UNIVERSITAT DE BARCELONA

Hygroscopic properties of single bacterial cells and endospores studied by Electrostatic Force Microscopy

Marc Van Der Hofstadt Serrano

UNIVERSITAT DE BARCELONA

Hygroscopic properties of single bacterial cells and endospores studied by Electrostatic Force Microscopy

Marc Van Der Hofstadt Serrano

Barcelona, December 2016

Doctoral Thesis

Universitat de Barcelona

Facultat de Física

Departament d'Enginyeries: Electrònica

Propietats higroscòpiques de cèl·lules i endòspores bacterianes individuals estudiats amb la microscopia de forces electrostàtiques

PhD program:

Nanoscience

Research field

Nanobiotechnology

Thesis Directors:

Gabriel Gomila Lluch

Author:

Marc Van Der Hofstadt Serrano

“A conclusion is the place where you got tired thinking”

Martin H. Fischer (1879-1962)

“Más sabe el diablo por viejo que por electrónico”

Contents

1 Introduction

Bacteria are attributed as the best adapted living organism in our planet. This statement is based under the conception that the simpler the organism, the faster it can evolve. Furthermore, bacteria are recognized as one of the first living organisms, so its evolution and adaptation has been going hand by hand with the development of the earth's environmental conditions. The vast adaptation of bacteria can be observed in their almost ubiquitous presence on earth; they can be found in the outer and inner organs of other living organism, or in soils and liquid environments where they can survive extreme conditions (such as temperature, radioactivity or salinity among others). Their adaptation and presence is such, that the overwhelming number of predicted bacterial cells on earth ($\sim 5 \times 10^{30}$) would have a biomass greater than the sum of plants and animals.

The large abundance of bacterial growth niches provide a rich diversity of bacterial characteristics. Within this diversity, some are advantageous and have a crucial role in human health and growth. In addition, many bacteria have a large use in the biotechnology sector, where applications range from fundamental biological studies (easiness to genetically modify bacteria), up to the exploitation in medical and industrial sector (such as in the production of antibiotics, medically-useful enzyme, food processing or biofuels generation). Antagonistically, there are pathogenic bacteria which are of great concern. Many virulent bacterial strains are responsible for severe illnesses, such as *Bacillus anthracis* (anthrax), *Corynebacterium diphteriae* (diphteria), *Vibrio cholera* (cholera), *Clostridium tetani* (tetanus) or *Streptococcus pneumoniae* (pneumonia) among others. Such is the problematic of virulent bacteria that by itself, *Mycobacterium tuberculosis* bacteria has been accounted for 2 million deaths annually. These two conflicting points of interest drives the need to fully unravel the properties of bacteria.

To establish an architecture within the bacterial domain, the ribosomal RNA (16S RNA marker gene) sequence analysis has been established as the major method for bacterial classification into species. Up to date, over 10^4 bacterial species have been described. Due to the large diversity encountered within the same bacterial species, there has been the need to sub-divide them into strains.

As an example, within the *Escherichia coli* species there are beneficial strains that help the host in the production of vitamin K2 while other strains cause serious food poisoning [1]. As a consequence, the classification by ribosomal RNA is still limited.

For the characterization and differentiation of bacterial strains, traditional microbiology research tools are still being used. This characterization can be divided into immunological and phenotypic, dependent upon the properties analysed. Under immunological characterization, the use of antibodies to detect antigens from specific bacterial cells helps to uncover composition properties. On the other hand, the phenotypic characterization is divided upon biochemical studies (which uncover functionality of the bacteria, such as detecting specific enzyme presence for metabolism classification) and morphological studies (which uncover structures such as cell shape, size, special structures and macroscopic morphologies such as aggregation and colony growth). With the discovery of the Polymerase Chain Reaction (PCR) in 1986, the actual studies performed by the presence of a given genetic sequence are termed as modern microbiology tools. Nevertheless, these genetic studies are still collaborated with traditional microbiology tools to link a genetic sequence to a specific bacterial trait.

The traditional microbiology characterization tools are limited, and can be restrictive to only the common bacterial species. This limitation pushed forward the need for new non-standard techniques to fulfil bacterial characterisation, where some traits could be specific to a unique bacterial species. These techniques address physical properties like mechanic pressure (such as turgid pressure), the electrical conductivity [2], bioluminescence properties [3], or orientation capabilities with the magnetic fields [4]. Furthermore, there are also other physicochemical properties which are of special interest in the medical sector, such as the adhesion capabilities [5], the hydrophobicity [6] or the hygroscopic properties [7]. With the exception of specific structural studies (where the electron microscope is used) most traditional microbiology and non-standard techniques are performed at the level of colonies (bulk analysis). Although a microbial colony arises from an individual bacterium, not all cells of the colony are genetically identical due to possible stochastic variability. As a consequence, the millions of cells present in a colony produce an average of the phenotype, hindering the heterogeneity of single cells.

The heterogeneity of bacterial colonies is important, since it could have practical consequences in the medical sector (antibiotic resistance or potential pathogens) and food industry (production and preservation) [8]. Furthermore, single individual traits can be masked by the study at the colony level, such as the actin polymerization or surface attachment proteins, which are only present at the cell poles of *Listeria monocytegenes* and *Bradyrhizobium japonicum*, respectively [9]. For this reason, the study at the single cell level is crucial to fulfil bacterial characterization.

Within single bacterial cell studies, many different techniques have been developed. The use of biological microelectromechanical systems (Bio-MEMS) based on dielectrophoresis, optical trapping or fluorescence (including flow-cytometry, confocal, super resolution, etc), have shown their ability to extract specific properties at the single cell level [8]. The main weakness of these techniques is the achievable resolution, the modification of the sample for its observation, and/or the possibility of only extracting one characteristic at a time. These restrictions limit the capability to study at the single bacterial cell level. To fulfil this gap, nanotechnology tools are recently being exploited (Nanomicrobiology [10]). Examples include the use of Nanoscale secondary ion mass spectrometry (nanoSIMS) or X-ray microscopy, which have helped to uncover structural and chemical composition of bacterial individual cells at the nanoscale [11,12].

The Atomic Force Microscope (AFM) is emerging as a promising nanotechnology tool for Nanomicrobiology. The AFM is capable of characterizing the structure of the bacterial cell and simultaneously obtain other physical properties of interest. In addition, it can also manipulate samples and function under physiological conditions, being this ability an important trait for microbiology research. The AFM has shown its ability to obtain high-resolution topographical images of bacterial samples under dry and liquid conditions, with the possibility of viewing living process such as extruding virus [13] or germination of bacterial spores [14], among other things. Physical properties obtained simultaneous to topographical imaging include mechanical characteristics (turgor pressure, elasticity, bursting forces, adhesion forces) [15], chemical attributes (chemical composition, antigen recognition, hydrophobicity) [16], functional responses (*in situ* antibiotics effects, growth medium modifications, effect of microwave radiation) [17–19], or electrical qualities (surface charge, dielectric value) [20,21].

This vast functionality of the AFM to characterize bacterial cells opens large possibilities to be used in the microbiology field; possibilities which cannot be contemplated by traditional microbiology tools. Hereafter, the AFM can help to deeper understand and solve open problems in microbiology. In particular, they can contribute to a better understanding of the properties of bacterial cells, one of the most outstanding forms of live.

One outstanding characteristic which present some bacterial species is the ability to produce spores to sustain harsh conditions. In particular, the endospores have attracted the attention of researchers, since it is a dormant form of the bacterial cell which has evolved to sustain harsh environmental conditions and at the same time being capable of germinating and reverting back to its bacterial vegetative state when adequate conditions are met. In the medical sector and the food industry this is of great concern since common sterilizing techniques (high temperature, UV radiation, common disinfectants or desiccation processes [22]) cannot be used due to the ability of the spores to remain unharmed at extreme conditions.

These extraordinary characteristics to sustain harsh conditions, which has not been observed to such an extent in other organisms, has been mainly attributed to the way endospores control its water content. A heterogeneous distribution of the water content plays a key role in bacterial resistance [23]. The ability of the bacterial endospores' inner core to remain dry (and hence less motile) has been shown to be significant for endospores resistance, since the core contains the crucial molecules for germination. The higher inactivation efficiency of a wet thermal treatment compare to a dry treatment shows the drastic effect the hydration properties has on the endospores' resistance [24].

Despite the large existing literature in hydration properties of single bacterial endospores [25], the hydration capabilities of single individual endospores still present some open questions. How do dry dormant endospores respond to different humid environmental conditions, how hygroscopic are they in comparison to dry bacterial cells, and specially, what is the hydration layout during hydration are some questions that at the single cell level remain unclear.

The objective of this thesis is to study the hydration properties of individual bacterial samples, undertaking special interest in dormant endospores and making special emphasis to cover the full range of environmental conditions. To

do so, measurements were performed from dry conditions up to fully hydrated conditions of bacterial samples, going through different relative humidity conditions. To achieve these results, we have made use of Electrostatic Force Microscopy (EFM), an adaptation of the AFM which the research group has considerable expertise. The use of this technique can report changes in the dielectric properties of bacterial samples, changes attributed to the presence or absence of water content due to hydration [21]. To accomplish such goal, various challenges of different difficulty have been addressed and solved.

Embarking with a basic understanding of the AFM, I focused on its use to image bacterial samples. With the special difficulty of imaging living bacterial cells in native conditions, I concentrated on the immobilization of bacterial samples and the use of complex and advanced AFM imaging techniques. This adjustment was used to observe bacterial division using the least aggressive attachment protocol. The large height presented by the spores and bacterial cells limited the use of the conventional methodology used by the research group based on Electrostatic Force Microscopy. A new methodology was implemented, with its respective understanding and adaptation of the AFM to perform such EFM measurements. This was firstly validated with an inorganic calibration sample and further tested on dry bacterial cells. I dedicated considerable amount of energy in the acquisition of electrical images of individual bacterial cells and endospores under different relative humidity. The abrupt changes in height of the endospores, and the humidity present in combination with electrical imaging, made obtaining results an arduous task. Nevertheless, the observed hydration properties of bacterial endospores differed from bacterial cells, where an explanation was presented attributed to their structural differences. Rounding up the work, final measurements were performed under liquid conditions, were the instability of measurements operated under liquid conditions intensified the complexity of obtaining results.

The structure of this work of thesis is structured into twelve chapters. After this *first* chapter of general introduction, in the *second* chapter we focus on the description of bacterial organisms to understand its characteristics. The *third* chapter presents the Atomic Force Microscope as a nanoscale characterization tool, and the ability of the Electrostatic Force Microscope to perform electrical characterization. In the *fourth* chapter a gentle AFM imaging technique is introduced to image individual bacterial cell in its native state. The *fifth* chapter presents a new methodology to enhance intrinsic electrical signal from the entire

sample under study. The *sixth* chapter shows the sub-surface capabilities of the EFM. The *seventh* chapter exposes the validation of the use of EFM under liquid conditions for topographically tall samples. The *eighth* chapter presents the study of the hygroscopic properties of bacterial vegetative cells and endospores and their hydration distribution. Finally, the *ninth* chapter deals with the first electrical images performed under liquid conditions of large biological structures. Rounding up, the *tenth* chapter will contain the main conclusions and future prospective of this thesis. It will be followed by the *eleventh* chapter with an appendix, and the *twelfth* chapter with references.

2 Bacteria as a *simple* living organism

With misconception, bacteria has been greatly classified as a simple organism. However its complexity is such that bacteria have been classified as an independent domain. In this chapter we will show just some small stripes of the complexity of the bacterial cells, making special focus on the bacterial species and endospore studied in this thesis.

2.1 Bacterial vegetative cells

The bacterial vegetative cell is the natural growth state of bacterial cells, expressing maximum metabolic activities (respiration, reproduction, absorption, fermentation...). If otherwise mentioned, the use of bacterial cells refers to vegetative state cells.

2.1.1 Bacterial morphology

Bacteria are prokaryotic cells, which contrary to eukaryotic cells (such as human cells), lack of membrane bound organelles (i.e. nucleus or mitochondria). Nevertheless, bacteria can still present a large variety of structures (Figure 2.1). All bacterial cells present a cell envelope which acts as a barrier of the cytoplasm (the internal composition of the bacteria) and the surrounding environment [26]. The bacterial cell envelope is composed by an inner cell membrane, consisting of a phospholipid bilayer with embedded proteins (also termed cytoplasmic or plasma membrane in eukaryotic cells). Its role is the selective permeability to ions and organic compounds, and attachment of extracellular structures. Surrounding the cell membrane, with the exception of the genus *Mycoplasma*, bacterial cells have a rigid cell wall made out of peptidoglycan. Its main role is to withstand internal turgor pressure. Some bacterial species may contain a thinner cell wall but surrounded by an outer membrane. This outer membrane is mainly composed of lipopolysaccharides, whose main function is pathogenicity

and adhesion. To increase bacterial resistance, some species my present a capsule composed of a polysaccharide layer to further increases protection.

Protruding from the cell envelope, there could be hair like appendages such as fimbriae/pili (for attachment/genetic transfer) and/or flagella (for movement/sensing). When regarding bacterial inner composition (the cytoplasm), a rich diversity is present, being dependent upon species. All bacterial cells present a nucleoid (with at least one circular chromosome) and ribosomes (for protein synthesis) which are homogenously distributed throughout the cytoplasm. Within the diversity of internal structures, it has been observed intracellular membranes, cytoskeleton and inclusions (for storage compartments such as for nutrients, gas for buoyancy, carboxysomes for CO_2 fixation, or magnetosomes for alignment with the magnetic fields.

In spite of all of these possibilities, a general approach for bacterial classification has been established following Gram staining. This method is capable of differentiating bacterial species into two large groups, exclusively upon their chemical and physical properties of the cell wall. Gram-positive bacteria express a thick layer of peptidoglycan, while on the other hand the Gram-negative bacteria express a thinner layer of peptidoglycan that is supplemented with an outer membrane. These differences are illustrated in Figure 2.1.

The morphology of bacteria can be as diverse as its structural composition. Their size belongs to the micrometre range, where the conventional size relies between 0.5 μm up to 5 μm. Nonetheless, there are exceptions with sizes that can be as small as 0.2 μm, or as large as 750 μm. For the common bacterial species, nanotechnology is an essential tool for the detailed characterization of bacterial cell at the single cell level. When characterizing bacterial shape, most bacterial cells have a rod-shape or a spherical shape. Nevertheless, there are other forms which can be found, such as curved rods, spiral-shaped, tightly coiled, club rod, helical or filamentous. Bacterial cells are usually present as single cells, but other patterns can be observed, such as pairs, chains or clusters.

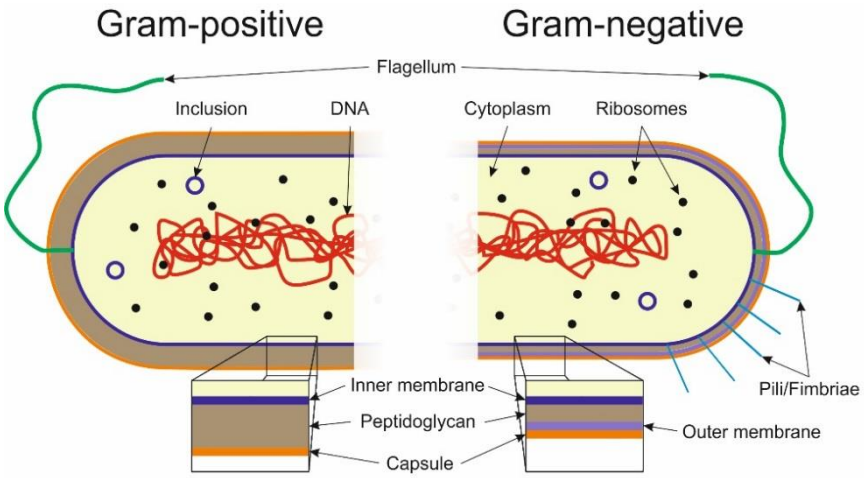

Figure 2.1 Schematic illustration of bacteria with the most common structures labelled. The differences between Gram-positive and Gram-negative are shown.

Bacteria can grow as individual cells, or they can form dense aggregations of bacteria (biofilms) to gain advantageous properties [27]. These biofilms can reach up to half a meter in thickness, with the likelihood of being a consensus of multiple species of bacteria. In the biofilm creation, an extracellular polymeric substance (EPS) is secreted to embed the bacterial cells. This collective growth favours protection (against dehydration, detergents and antibiotics), facilitates communication and gene exchange between bacterial cells. In many cases, the biofilms acts rather as a multicellular organism instead of a bunch of unicellular organism side by side, showing different physiologies compared to the planktonic state [28]. The secretion of the EPS allows bacteria to adhere stronger to surfaces, making it of special importance in medicine due to increased difficulty in removal. The pathogenic biofilms are usually present in infections when regarding to implanted medical devices or in chronic infections, predominately being more resistant to medical treatments.

2.1.2 Bacterial cell growth

The ordinary mechanism of bacterial growth is by binary fission (an asexual reproduction), but many other rare mechanism have been reported [29]. In binary

fission (Figure 2.2), the bacterial cell initially elongates and creates at least a copy of its chromosome. Each copy of the chromosome is attracted to different poles of the bacterium, and FtsZ proteins are recruited at the middle of the bacteria to form the FtsZ ring. This structure directs the formation of a septum that divides the cytoplasmic content. Further on, the cell pinches into two, giving rise to two identical daughter cells. The speed at which bacterial division occurs is principally dependent upon species and temperature conditions, for example at optimum conditions (37ºC) *Escherichia coli* can perform a bacterial division in ~19 minutes, while *Mycobacterium* may need up to days.

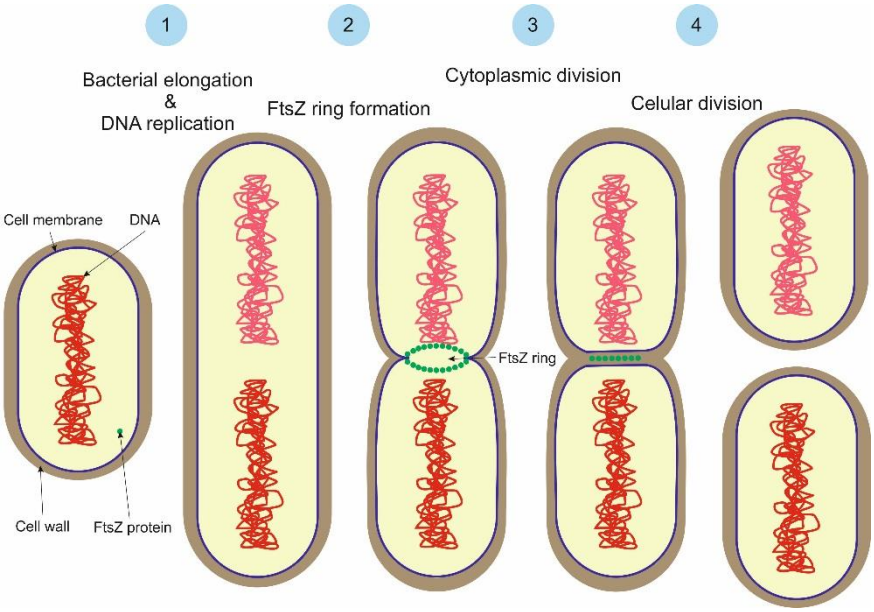

Figure 2.2 Schematic illustration of the bacterial binary fission process of a bacillus shape bacteria.

Genetic variability due to random mutations during bacterial growth is rare, and occur only sporadically. The evolution of bacteria is mainly caused by horizontal gene transfer (HGT), which is the transfer of genetic material between organisms (not from mother to daughter cells). This transfer can be by conjugation (direct cell-to-cell contact or by a bridge), transformation (direct uptake of exogenous DNA) or by transduction (DNA introduced by a virus). This genetic transfer

capabilities has introduced an extensive adaptive compatibility to hostile environments, especially with respect to antibiotics resistance [30].

2.1.3 Studied bacterial cells

2.1.3.1 *Escherichia coli*

Escherichia coli (*E. coli*) is the model bacterial organism for the Gram-negative bacteria. The ease and inexpensive cultivation conditions required for growth in the laboratory, makes *E. coli* to be the most used host organism for recombinant DNA, and hence for molecular genetics. They present a rod-shaped morphology, with some strains being motile due to the presence of flagella. The metabolism they exhibit is of facultative anaerobic, inhabiting principally the gastrointestinal tract of warm-blooded animals. The harmless strains help in vitamin K_2 production, food absorption and avoiding colonization of pathogenic bacteria. The virulent strains of *E. coli* can cause sever foodborne infections, urinary tract infections or meningitis. For these reasons, *E. coli* is used as a water contamination indicator.

One of the strains used in this work of thesis is the *E. coli* K-12 MG1655, which has been widely used in laboratory due to its minimal genetic manipulation. The other strain used is the Enteroaggregative *Escherichia coli* O44:H18 (EAEC 042), which has been associated to acute diarrhoea, being one of the main sources of several foodborne outbreaks [31]. Both strains in physiological media grow in an individual bacterial form to a length and diameter of 2 μm and 1 μm, respectively. When EAEC 042 is grown using eukaryotic cell medium, to mimic host conditions, they form a biofilm in a characteristic aggregative or "stacked-brick" pattern, giving rise to its pathogenicity [27].

2.1.3.2 *Bacillus cereus*

The *Bacillus* genus is one of the model organism for the Gram-positive bacteria. They are ubiquitously fond in nature, with special interest in industrial, ecological and clinical relevance, especially for its proximity to *Bacillus*

anthracis (anthrax infections) and *Bacillus thuringiensis* (insect pathogen used as pesticide). *B. cereus* presents a rod-shape morphology, a facultative anaerobic metabolism, motility and grows best at moderate temperatures (mesophilic). It is commonly found in the soil as a saprophytic organism, or in the microflora of invertebrates. When regarding to pathogenicity for humans, they cause 2-5% of the foodborne intoxications due to the production of emetic toxins and enterotoxins in the gastrointestinal tract (especially in contaminated rice). In addition, it is also an opportunistic pathogen, being capable of causing local and systemic infections. However, *B. cereus* is widely used as a biological control agent in the suppression of fungi and crop diseases.

Strains of *B. cereus* can form biofilms, but the majority develop as individual bacteria, with a length and a diameter of 3-4 μm and 1 μm, respectively. Being a Gram-positive bacteria, it presents a thick cell wall, around 60 nm thick as reported from TEM observations [32]. One of the most characteristic properties of *B. cereus* is its ability to produces spores to sustain harsh conditions (which is explained in section 2.2) [33].

2.2 Bacterial spores

The ability to withstand harsh environmental conditions by living organism can be approached by different mechanisms. One of the most effective mechanism is the production of bacterial spores (sporulation). The bacterial spore resistance is such, that they have been proposed as a possible source of extraterrestrial life [34]. In general, bacterial spores are characterized by the high tolerance to dessication, temperatures and toxic conditions compared to its vegetative cell. They are capable of achieving this resistance by a system of thick protective layers, the protection of the DNA by proteins, and remaining in a dormant state. The compact layers make the spore visible upon the use of optical phase contrast microscopy or by the use of Schaeffer-Fulton stain preparations. The spore are usually smaller in size than the vegetative cell forms, thus making necessary the use of nanotechnology tools in order to obtain a detailed characterization [35].

A type of spore with special interest are the endospores, such as those produced by *B. cereus*. These type of spores are produced in the interior of the bacterial

cells, with length and diameter dimensions of ~1.5 μm and ~1 μm respectively. The endospore is a non-true offspring remaining in a dormant form of the bacteria. To achieve this, the bacteria condenses itself, with thicker walls for a higher protection compared to other types of bacterial spores. Under activation, the endospores are capable of germinating back into the vegetative cell form of the bacteria within few minutes. If not activated, the *Bacillus* endospore can sustain high temperatures (~80ºC), UV radiation, common disinfectants, and desiccation processes [22]. These faculties make the endospores of special interest for research due to its implications on the medical and food industry.

2.2.1 Endospore formation and germination

As mention previously, the endospore formation is not contemplated as a reproduction mechanism by itself, it is rather established as a method for surviving harsh environmental conditions. The sporulation is triggered in bacteria by the scarce of nutrients, especially of carbon or nitrogen source. The process of spore formation takes place within a few hours (the whole process is depictured in Figure 2.3). The different steps occurring during sporulation are the following. The first step is the replication of the DNA and into of an axial filament which stretches across the long axis of the cell (Stage I). Contrary to bacterial division, in spore formation an asymmetric cell division occurs, giving rise to the formation of a prespore (Stage II). The prespore is separated with a thin cell septum ("*spore septum*"). The prespore is engulfed by the mother cell, where the spore septum is started to be degraded. This stage forms a free protoplast (forespore) which is separated from the mother cell with two membranes (Stage III). The cortex formation starts between the two cell membranes (Stage IV). At the same time (Stage V), large amounts of proteins are synthesized to protect the DNA of the forespore. Dipicolinic acid is synthesized by the mother cell and absorbed (together with divalent ions, principally Ca^{2+}) into the core of the forespore, causing partial dehydration and mineralization of the forespore's core. The coat and the exosporium are formed as extreme outer layers over the cortex. On the final stages, VI and VII, the spore matures by further dehydration and development of an extra chemical and heat resistance. At the end, the cell lysis to give a mature free endospore [36].

The germination of the spore gives rise to a vegetative cell once conditions are suitable for growth. This activation is commonly triggered by a response to the presence of amino acids. The spore is stimulated to hydrate, where the loss of the Ca^{2+} ions and the dipicolinic acid allow the activation of metabolism to break dormancy. The spore outer layers cracks and expands, allowing the vegetative cell to emerge from the broken endospore [14].

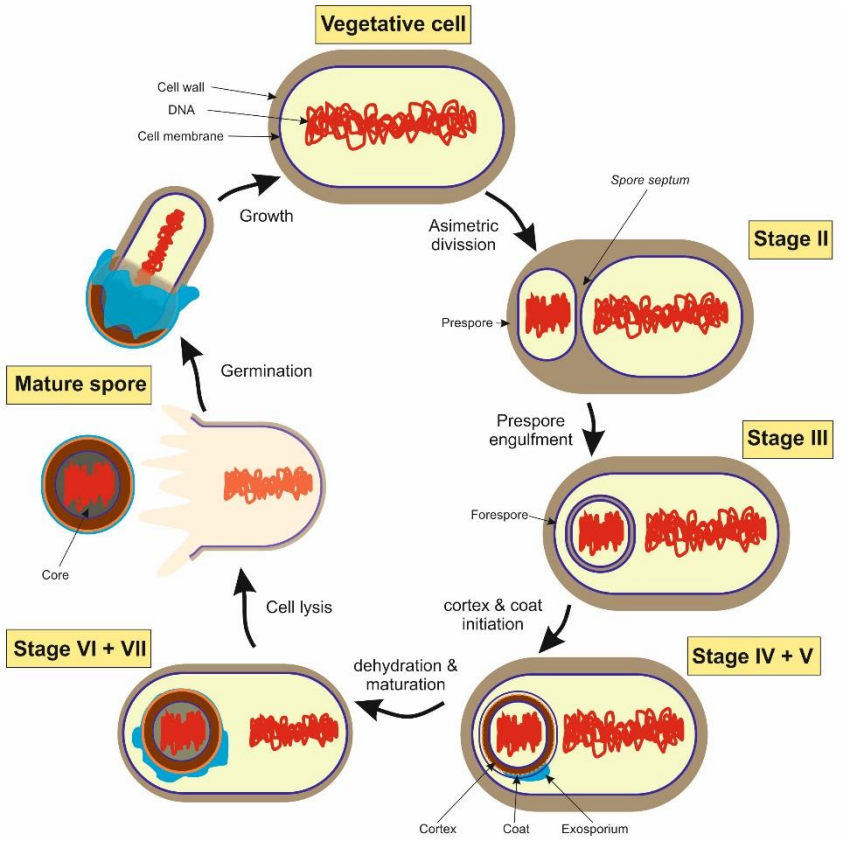

Figure 2.3 Schematic illustration indicating the stages which take place during the sporulation of the *Bacillus* genus.

2.2.2 Endospore structure

The structure of the *Bacillus* endospores is very important for their resistance to the harsh environmental conditions, reason why the endospore formation is a complex mechanism. Its construction is arranged in a series of concentric layers [22]. Starting from the most inner part, one finds the core. The core contains the spore chromosomal DNA, surrounded and protected by small acid-soluble proteins (SASPs). Theses SASPs proteins protect the DNA from ultraviolet radiation, chemicals and dry heat. Furthermore, the core also presents ribosomes and other important enzymes for activation, but all remain metabolically inactive. Up to 15% of the dry weight of the spore consists of calcium dipicolinic acid complex, which stabilize the DNA and prolongs the core dehydration. Surrounding the core, there is an inner membrane, a highly packed cell membrane which is the major permeability barrier for water and damaging chemicals. A thin layer of peptidoglycan (core wall) surrounding the inner membrane would become the cell wall of the bacterium. This structure up to the core wall will form the new vegetative cell after germination.

The cortex is the first layer of protection, being a thick layer of a less cross-linked peptidoglycan, showing a gradient of cross-linking as it extends outwards from the core. It is the most hydrated region of the spore, giving resistance to high temperatures. Covering the cortex there is the coat layer, a cross-linked protein layer which acts as a sieve, giving resistance against chemicals and enzymatic molecules. Some bacterial species of *Bacillus* can present a concluding layer of exosporium. It is a thin glycoprotein layer, where its basic function is to avoid the penetration of large potential harmful molecules and to interact with the environment and the host organism. The thickness of these layers of protection is dependent upon the species used, and it is related to the heat resistivity of the endospore, with a higher heat-resistant spore presenting a thicker protection [37]. For the strain used in this work of thesis, Transmission Electron Microscopy (TEM) revealed a thickness around 150 nm (Chapter 8).

3 A taster of the Atomic Force Microscope and the Electrostatic Force Microscope

Scanning Probe Microscopy (SPM) techniques are characterized by analysing the sample's surface by using a raster scan technique. They are composed of three main components: the scanner, the probe and the controller (Figure 3.1). The scanner is accountable for the precise movement and positioning of the sample with respect to the probe. This is usually made of a piezoelectric actuator which can execute movements with an accuracy down to the atomic level, being regulated by an electrical voltage. These movements are responsible for the lateral movement in the X and Y direction to perform the raster scan. Since it is a line by line imaging technique, one direction is performed fast while the other movement direction is slower. This scanning velocity can be controlled, together with the number of points acquired in each line, to enhance image quality and resolution. Furthermore, the scanner is also responsible for the vertical movement (z direction) to adjust the probe-sample distance.

The probe is dependent upon the scanning technique used, but all follow the structure of a needle-like form with a very sharp apex. The probe is placed in close proximity to the sample (on the nanometre level), allowing the characterization of a specific physical probe-sample interaction. This interaction is dependent upon a local material property, where the probe-sample interaction volume resolves the resolution achievable, which can be brought down to few picometres. The controller is responsible for the movement of the scanner, being of special importance in the vertical direction. With a feedback-control system, the controller operates the scanner to maintain the constant probe-sample interaction desired. The data obtained from the movement of the scanner creates a two-dimensional grid of data points, which can be electronically drawn as a topographical image of the sample surface (Figure 3.1).

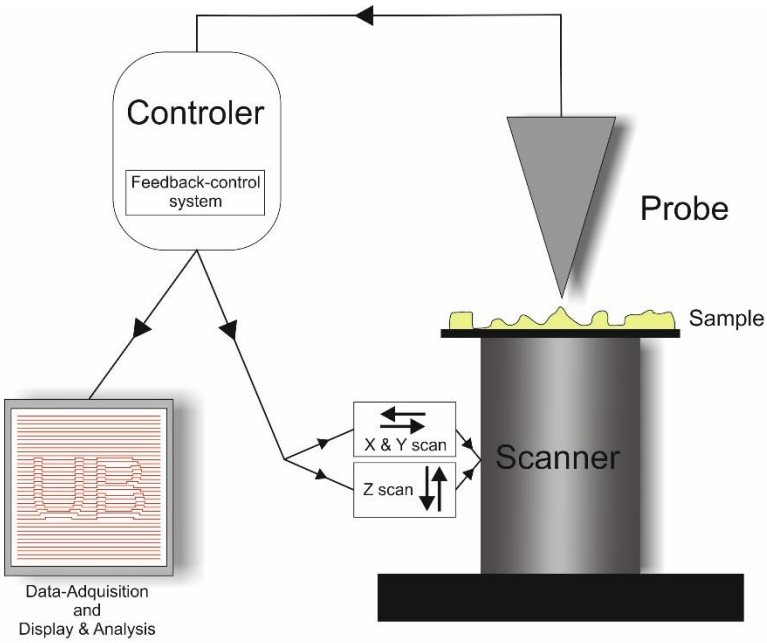

Figure 3.1 Schematic illustration of a simplified set-up for a scanning probe microscope. The controller operates the X & Y movement of the scanner. A shift in the probe-sample distance is detected by the probe response, which sends as a signal to the controller. The feedback-control system calculates the shift in probe-sample distance, where the controller moves the scanner in the Z direction to regain the probe-sample interaction desired. The obtained data is electronically drawn.

The pioneer SPM technique was the Scanning Tunnelling Microscope (STM). It was invented in 1981, and such was the impact of these new family of microscopes, that their inventors were awarded with the Nobel Prize in 1986. The STM relies on the dc tunnelling current when two conductive materials are in very close proximity (under 5 nm distance). The current sensed is exponentially proportional to the tip-sample distance, so a feedback loop upon the sensed current will maintain a certain probe-sample distance. Measurements are principally reserved to conductive samples, but very thin insulating samples can also be used.

With the limitation of the STM to principally measure conductive samples, the Atomic Force Microscope appeared in 1986 to fulfil the research at the nanoscale [38]. The AFM technique is based on a micrometre-long cantilever which

deflects depending upon the interaction force with the sample, which are usually very short ranged. At the free end of the cantilever, a sharp tip with an apex ranging in the nanometre size (1-200nm) is present to enhance the detection of local interactions. To detect this deflection, initially a STM was used, but it was later substituted with a laser and a multiquadrant photodiode for simplification (Figure 3.2).

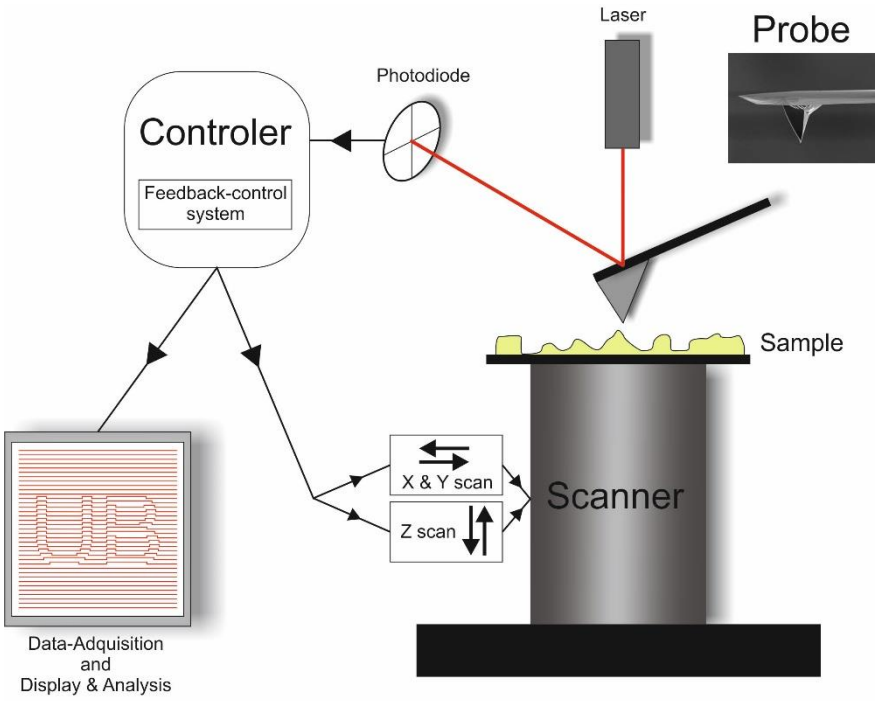

Figure 3.2 Schematic illustration of the Atomic Force Microscope. The probe-sample interaction causes the bending of the cantilever. The position sensitive photodiode detects the deflection due to the movement of the laser beam which is reflected on the backside of the cantilever. The inset shows the side view of the cone and a part of the cantilever of an AFM probe obtained with SEM (source: AFM-probe catalogue from www.nanoandmore.com).

The force detected by the AFM is limited by the thermal noise of the system, reaching measurements which can go down to the range of the pN with the photodiode system. The use of the forces can also be used to detect physical and physicochemical properties (such as by the functionalization of the probe with a

specific compound). Properties such as Young modulus, dielectric constant, chemical characterization or magnetic properties with nanoscale resolution are some examples [39,40]. Furthermore, the AFM has the ability to operate in a wide range of conditions, with special interest in ambient and liquid environments for life sciences research.

The SPM techniques have been mostly used as characterization techniques, where dependent upon the feedback used, different properties of the samples are obtained. In this thesis, the AFM is used as a topographical tool to image samples; and the Electrostatic Force Microscope (EFM), and adaptation of the AFM to detect electrostatic forces for the electrical characterization of the samples. These methods are further explained in the subsequent sections.

3.1 The Atomic Force Microscope as a topographical imaging tool

The principal use of the AFM has been the acquisition of topographical images of sample surfaces, which can reach down to sub-nanometre resolution [41]. The probe-sample (more precisely the probe apex-sample) interaction relies on short range forces of the Van der Walls and contact types (apex-sample < 10nm). As the probe approaches the surface, the first regime is characterized by attractive forces, which cause the deflection of the cantilever towards the sample until contact is made (Figure 3.3). As the probe approaches further the sample, the repulsive forces increase until the attraction forces are balanced by the repulsion forces, and hence the probe does not suffer any force from the sample (zero-deflection point). As the probe is further pushed towards the sample, the repulsive forces steeply increase and cause the cantilever to deflect away from the sample.

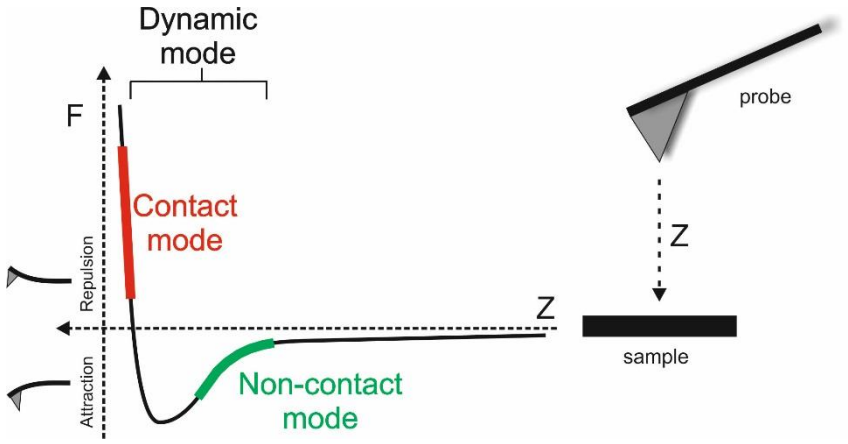

Figure 3.3 Probe-sample interaction regimes in Atomic Force Microscopy. At large separations, the forces are attractive and hence the system is in a non-contact regime. At touching distances, the forces are repulsive and hence the system is in a contact regime. Covering both ranges, the system is in a dynamic regime.

Dependent upon the region in which the probe-sample interaction is established, the imaging technique can be classified into different imaging modes. The three different imaging modes are:

i. Contact mode

In contact mode, the probe-sample interaction is in the repulsive regime (Figure 3.3). The probe-sample distance is maintained by performing feedback on the deflection of the cantilever, where the vertical displacement of the scanner maintains the desired deflection. Zero-deflection point is desired since it is the least aggressive point, but due to instability, images are obtained applying enough force to avoid instabilities. This force exerted onto the sample may cause modifications to the tip (wear out or contamination) or alterations to the sample. To reduce perturbation, soft cantilevers ($k < 1N/m$) are commonly used and images are obtained at slower scan velocities than for other imaging techniques.

ii. Dynamic mode

The dynamic mode, which can be otherwise named as AC or Tapping mode™, operates in an intermittent contact region (Figure 3.3). The

cantilever is mechanically oscillated close to its resonant frequency (to obtain maximum oscillation) with the use of a piezoelectric actuator attached at the probe holder. The amplitude of the oscillating cantilever is recorded by the photodiode and quantified with a lock-in amplifier (to filter out noise from frequencies which are not the exciting frequency). The reduction on the probe-sample distance causes a reduction on the oscillating amplitude. A given amplitude (smaller than its free vibration amplitude far from the sample) is defined as the set-point, where the feedback-control system would be used to cause the vertical displacement of the scanner to maintain the desired amplitude. At the same time, the lock-in amplifier is capable of acquiring at each point the phase shift between the excited oscillation and the measured oscillation. This information can complement the characterization of the imaged sample independently from topography, such as material composition or adhesion.

The general excitation mechanism is performed by acoustic mode, but other methods such as by magnetic forces (MAC-Mode^{TM}), laser heating or electrostatic forces can be used [42]. Under liquid conditions for imaging, these alternative methods have shown to present a better performance than acoustic mode. This is because they only oscillate the cantilever, in contraposition to acoustic modes which oscillate mechanically the liquid, which increase noise and instabilities. On a general basis, dynamic mode imaging is preferably used over contact mode since it is less aggressive, since the probe-sample interaction time is reduced. This reduces the possible modification of the sample and probe. Furthermore, the shear forces exerted by the tip on the sample while performing the raster scan are drastically reduced.

iii. Non-contact mode

In non-contact mode, the system works in the attractive regime (Figure 3.3). The cantilever is oscillated at its resonance frequency (with a small amplitude, <10nm) in very close proximity to the sample (~10nm). The attraction forces due to the reduction on the probe-sample distance, cause a decrease on the resonance frequency of the cantilever. A phase-locked loop is used to detect the shift in frequency or amplitude, and hence cause the vertical displacement of the scanner to maintain the desired resonance frequency. Since the probe hovers over the sample, nor the probe or the

sample suffer modifications. Maintaining a good feedback mechanism is hard, especially on tall topographical samples. This makes non-contact mode a demanding imaging technique non suitable for abrupt topographically tall samples.

3.1.1 AFM for biological imaging, microbiology on the lookout

Due to the complicated setup, little work had been done until the introduction of the optical laser and the photodiode in 1988. Since then, the number of life science publications with the AFM has increase drastically. Nowadays the system has become relatively simple to use by the life science community, making reasonably easy the image acquisition from large eukaryotic cells down to the important molecular units such as DNA. Furthermore, the system allows to perform images under liquid conditions. The general difficulty of performing images under liquid conditions is the immobilization of the sample onto the substrate. Contrary to eukaryotic cells which express focal adhesion points onto the substrate, bacterial cells lack of strong basic adhesion mechanism. This makes bacteria to be loosely bound to the substrate, which is a crucial requisite for AFM imaging.

A number of protocols have been developed in order to overcome the problem of very weak adhesion force of bacteria with the substrates [43]. These attachment techniques can be divided into 2 main groups.

- The physical entrapment techniques which restrain the bacteria into a compartment, avoiding the movement of the bacterial cell (Figure 3.5a). This mechanism prevents to a large extent the movement of bacterial cells, but cause a mechanical stress.
- The use of specific substrate coatings which are used to attach bacteria onto the surface. They could either be by covalent binding (Figure 3.5b) or by physisorption (Figure 3.5c). The covalent binding strongly attach bacteria onto the substrate, affecting bacterial integrity (since they irreversibly cause chemical modifications on the cell surface). On the other hand, physisorption (weak electrostatic forces) is the natural

mechanism of bacteria adhesion onto substrates, hence being the least aggressive mechanism. The problem relies on the difficulty of imaging living bacteria, since bacteria are easily displaced, reason why little work has been done (especially in bacterial growing mediums).

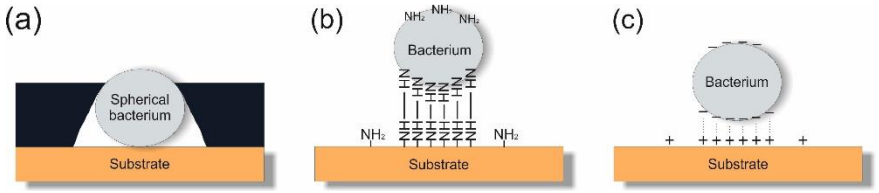

Figure 3.5 Schematic illustration of the 2 main groups of bacterial adhesions onto substrate for AFM imaging. (a) The physical entrapment relies on the jammed bacterial cell while (b and c) the substrate coatings rely on the attachment of the cell wall to the substrate. (b) Relies on the covalent attachment of bacterial cells, being a firm attachment, while (c) relies on the weak electrostatic forces, being a loose but less aggressive attachment.

3.2 Electrical modes of the AFM

One of the advantages previously describe of the AFM over the STM was its ability to measure insulating samples, but this does not restrict the capability of the AFM to measure electrical properties of samples. To do so, a conductive probe is used, where the sample can present insulating properties and be much thicker than the ones limited to the STM. With the adequate electronics, the local electrical properties of the sample can be measured and quantified, such as impedance, resistance, surface potential or dielectric polarization among others. Dependent upon the detected physical magnitude, the electrical characterization techniques can be divided into two groups:

i. Current detection techniques: the current flowing between the tip and the sample is measured to obtain the electrical property of interest. Some techniques are:
    a. **Conductive AFM (C-AFM):** A DC voltage is applied between the probe and the substrate, allowing the change in

DC current to be measured (with the use of a current amplifier). As an electrical contact must be present, images are obtained in contact mode and using non-wearable probes, allowing conductivity of the sample to be imaged simultaneously to the topography. Alternatively, current-voltage curves allows studying the resistivity and voltage dependence of regions of interest of the sample. Measurements are restrained to be performed in dried air conditions.

b. **Scanning Capacitance Microscopy (SCM):** A high frequency AC potential (GHz range) is applied between the probe and the substrate, forming a capacitor. The changes in the probe-sample capacitance (dC/dV) are detected by an electronic resonance circuit. The carrier density and the charge carriers can be extracted. This technique has been strictly restricted to the semiconductor industry, and as in C-AFM, images are obtained in contact mode.

c. **Nanoscale Impedance Microscopy (NIM):** An AC voltage is applied between the probe and the substrate, where an impedance analyser measures directly the impedance of the sample $Z(\omega)$. It is similar to C-AFM, where in this case the amplitude and phase of the AC current is measured to detect conductivity and local dielectric properties of the sample. Impedance images can be obtained during topography at a fixed frequency or can be obtained in non-contact mode. Furthermore, it can be run in spectroscopy mode, where at a given point of the sample, an impedance spectrum can be acquired. The need of a very sensitive low noise wide bandwidth amplifier makes NIM a complex technique, and hence not commercialized. As in C-AFM, this characterization technique is restricted to dried air conditions.

d. **Scanning Microwave Microscopy (SMM):** It is the extention technique of NIM, where the AC voltage is applied at higher frequencies, in the range from 0.1-100GHz. The microwave scattering parameters (S-parameters) are measured and related to the local impedance probe-sample interaction (since the apex of the probe acts as an antenna). This allows to obtain

conductivity and capacitance images at the nanoscale during topographical imaging. AFM based SMM systems are a young-commercialized technique, so little work has been done, where the quantification of images has been recently shown [44] and applied on biological material [45].

ii. Force detection techniques: the deflection or the oscillation amplitude of the cantilever due to the electrostatic forces interacting with the samples are measured to obtain the electrical property of interest. Techniques are:

   a. **Kelvin Probe Force Microscopy (KPFM):** An AC voltage is applied between the probe and the sample to cause an electrical oscillation of the cantilever. The electrical force would be dependent upon the probe-sample interaction. The amplitude of the first oscillation harmonic, $A(\omega)$, of the electrical force is proportional to the difference between the surface potential and a DC voltage applied by the probe. With the variation of the DC-potential of the probe, the first harmonic can be cancelled out (feedback), allowing the extraction of the surface potential (or work function) of the sample, which can be obtained during topographical imaging.
   b. **Scanning Polarization Force Microscopy (SPFM):** As in KPFM, an AC voltage is applied to excite electrically the cantilever, where in this case the feedback is performed on the amplitude of the second harmonic, $A(2\omega)$. The acquired image couples topography with the dielectric sample response, making quantification challenging. This technique has been mainly used for thin soft layers like water, since it is a non-contact imaging technique.
   c. **Electrostatic Force Microscopy (EFM):** It is a technique very similar to SPFM, but in this case no feedback is performed during electrical image acquisition. EFM is explained with a greater extent in the next section since it is the chosen technique for this work of thesis.

3.3 The Electrostatic Force Microscope as an electrical characterization tool

This work of thesis uses the Electrostatic Force Microscope to detect and quantify electrostatic interactions between a sharp conducting probe and the sample. In particular, the dielectric polarization properties of samples have been characterized, which is the property of a material to orient permanent or induced electric dipoles in response to an external electric field.

As in SPFM and KPFM, in EFM a voltage is applied onto a conductive probe to create an attractive electrical force between the probe and the sample. The most basic system, DC-EFM, relies on the application of a constant DC-voltage (V_{dc}), which would cause a static bending of the cantilever following the expression:

$$F_{dc}(z,\varepsilon) = -\frac{1}{2}\frac{\partial C_T(z,\varepsilon)}{\partial z}\left(V_{dc} - V_{sp}\right)^2 \tag{3.1}$$

where z is the apex-sample distance, C_T the total capacitance between the probe and the sample, V_{sp} the surface potential, and ε the sample effective dielectric constant. From expression 3.1, the dielectric properties of the sample can be extracted if the surface potential is known, although at high DC-voltages the error induced by V_{sp} is negligible. The sensitivity is limited by the thermal and electronic noise.

The capacitance gradient and the surface potential of the sample can be obtained separately by the use of a dynamic detection (AC-EFM). To do so, an AC-voltage (V_{ac}) is used,

$$V_{ac} = V_0 \sin(\omega t) \tag{3.2}$$

where ω is the frequency of the voltage applied between the probe and the sample. This creates a static electrostatic force (F_{dc}), a force oscillating at the excitation frequency (first harmonic, F_{ω}), and a force oscillating double the frequency (second harmonic, $F_{2\omega}$) according to:

$$F_{dc}(z,\varepsilon) = -\frac{1}{2}\frac{\partial C_T(z,\varepsilon)}{\partial z}\left[\frac{1}{2}V_{ac}^2 + \left(V_{dc} + V_{sp}\right)^2\right] \tag{3.3}$$

$$F_{\omega}(z,\varepsilon) = -\frac{\partial C_T(z,\varepsilon)}{\partial z}\left(V_{dc} + V_{sp}\right)V_{ac}\sin(\omega t) \tag{3.4}$$

$$F_{2\omega}(z,\varepsilon) = \frac{1}{4}\frac{\partial C_T(z,\varepsilon)}{\partial z}V_{ac}^2\cos(2\omega t) \tag{3.5}$$

While the static and the first harmonic contain information on the surface potential of the sample, the second harmonic contains only information on the capacitance gradient of the probe-sample setup, and hence direct information on the effective dielectric constant of the sample. Nevertheless, the C_T is dependent upon the probe-sample system, where the probe geometry plays a key role, following expressions:

$$\frac{\partial C_T}{\partial z}(z,\varepsilon) = \frac{\partial C_{apex}}{\partial z} + \frac{\partial C_{cone}}{\partial z} + \frac{\partial C_{cantilever}}{\partial z} \tag{3.6}$$

The variation of the cantilever contribution, as compared to the cone and the apex contributions, for the nanometric displacements of the probe have shown to be negligible [46]. Analytical expressions for the capacitance gradient including the probe and sample geometries, and its dielectric properties are scarcely available. Only in the case of a probe interacting with a metallic surface or with a very thin dielectric film, an accurate analytical expressions can be derived [47,48]:

$$\frac{\partial C_{apex}}{\partial z}(z,\varepsilon) = 2\pi\varepsilon_0\frac{R^2(1-\sin\theta)}{\left(z+\frac{h}{\varepsilon}\right)\left(z+\frac{h}{\varepsilon}+R(1-\sin\theta)\right)} \tag{3.7}$$

$$\frac{\partial C_{cone}}{\partial z}(z,\varepsilon) = \frac{2\pi\varepsilon_0}{\ln\left[\tan(\theta/2)\right]^2}\times\left[\ln\left(\frac{H}{z+\frac{h}{\varepsilon}+R(1-\sin\theta)}\right) - 1 + \frac{R\cos^2\theta/\sin\theta}{z+\frac{h}{\varepsilon}+R(1-\sin\theta)}\right] \tag{3.8}$$

where ε_0 is the permittivity of vacuum, R the apex radius, θ the cone angle, h the thickness of the sample, and H the cone height. The metallic case corresponds to

h=0 in the above expressions. In general, however, one has to restore to finite element numerical calculations [21,49].

The AC-EFM measurements can either be performed in Frequency Modulation EFM (FM-EFM) or in Amplitude Modulation EFM (AM-EFM) dependent upon the detection system used. FM-EFM detects the frequency shift in the resonance frequency of the cantilever, since electrostatic forces on the cantilever lead to slight modification of the spring constant. While FM-EFM has theoretically better electrical image resolution and localization, its advantage does not compensate for the complex and additional PLL-feedback loop system required [50]. On the other hand, AM-EFM detects the change in the electrical amplitude of the cantilever, being a much easier technique without losing much spatial resolution [49]. For this reason, AM-EFM is used in this work of thesis for electrical characterization.

The change in the electrical amplitude can be easily recorded with a lock-in amplifier (Figure 3.6). The lock-in amplifier is used to electrically oscillate the cantilever with an AC-voltage well below the resonance frequency of the cantilever, to avoid contributions from the mechanical response of the cantilever. The photodiode of the AFM system coupled to the lock-in detector is used to obtain the amplitude and the phase of the oscillation at the second harmonic ($A_{2\omega}$). Conversion to change into capacitance gradient from the electrostatic force can be done with the following expression:

$$\frac{\Delta\partial C}{\partial z} = \frac{2\sqrt{2}}{V_{ac}^2} k \frac{(A_{2\omega} - A_{2\omega,offset})}{mG} \tag{3.9}$$

where V_{ac} is in rms values, $A_{2\omega,offset}$ is the lock-in offset, k the equivalent spring constant, m the optical lever sensitivity, and G the lock-in gain. The use of the lock-in amplifier reduces drastically the noise (in comparison to DC-EFM) since it is very selective for the measuring frequency.

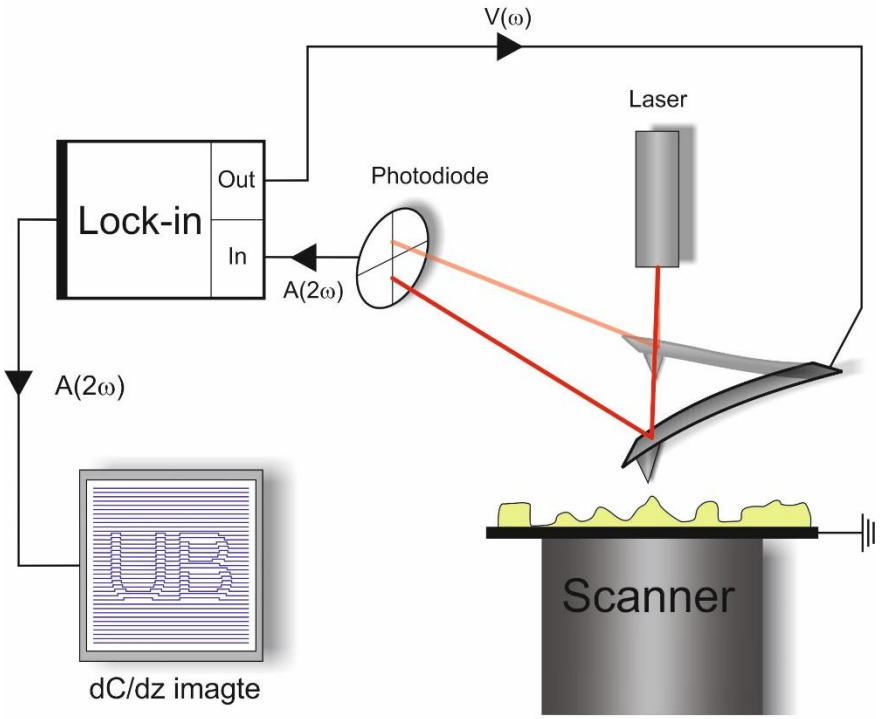

Figure 3.6 Schematic illustration of the AM-EFM. The electrostatic force between the probe and the sample cause a change in the electrical amplitude oscillation of the probe. This is recorded by the photodiode, which sends it to the lock-in to process it. The resulted amplitude is a reflection of the capacitance gradient image.

From EFM measurements, the electric permittivity of samples can be extracted, as expression 3.7 and 3.8 shows (for the case of a thin film). A simple method is by an approach (capacitance gradient-distance) curve, with the previous calibration of the probe geometries on a metal substrate. This reveals electrical information at a given point of the sample. To obtain electrical capacitance gradient images, a two pass imaging technique is used. In this type of imaging, during the first scan line the topographical image is obtained, while on the second pass, at a given lift distance, the electrical image is obtained while the AC-voltage is applied. The electrical images can be obtained by two modes:

i. **Constant height mode**: in this mode, the probe hovers parallel to the metallic substrate at a given height. In this method, the major contrast

is obtained at the highest point of the sample, hence being not suitable for high non-planar samples.

ii. **Lift-mode**: In this mode, the probe hovers parallel to the sample's topography at a given lift distance. This allows to obtain maximum contrast from the entire sample, but as it will be shown in chapter 5, the vertical displacement of the probe introduces an artefact to the electrical images, hindering intrinsic properties of the sample.

Furthermore, due to the penetration capabilities of the electric fields, characterization of the properties lying under the surface could be extracted. This subsurface characterization is explored under chapter 6.

3.4 Electrical characterization under liquid conditions

As explained at the beginning of this chapter, one of the advantages of the AFM is its ability to perform images under liquid conditions, without the loss of the nanoscale resolution. This opens the door to perform nanoscale characterization of biological material in their natural conditions and on living organisms *in situ*. One of such examples is the electrical characterization.

There are several issues in the electrical characterization which need to be taken into consideration when moving from an experiment in dry conditions to experiments under liquid conditions (especially with the use of polar protic solvents such as water). The presence of ions and electro-active species, which are dissociated and are free to move in the water solvent, create a conductive solution and the likelihood of electrochemical reactions. Furthermore, the dielectric constant of water ($\varepsilon_{r,\,water}$~80) is greatly higher than that of air ($\varepsilon_{r,air}$=1). One important characteristic change of ionic water solutions with respect to air is the presence of the electrical double layers (EDL). These layers occur when a metallic electrode surface or a static surface charge (insulating) is exposed to an electrolyte solution, where the excess charges from the metal or the static surface charge form a space charge region in the liquid. This charge region is

compensated by the adsorption of counter ions (from the solution) to reach a thermodynamic equilibrium (Figure 3.7).

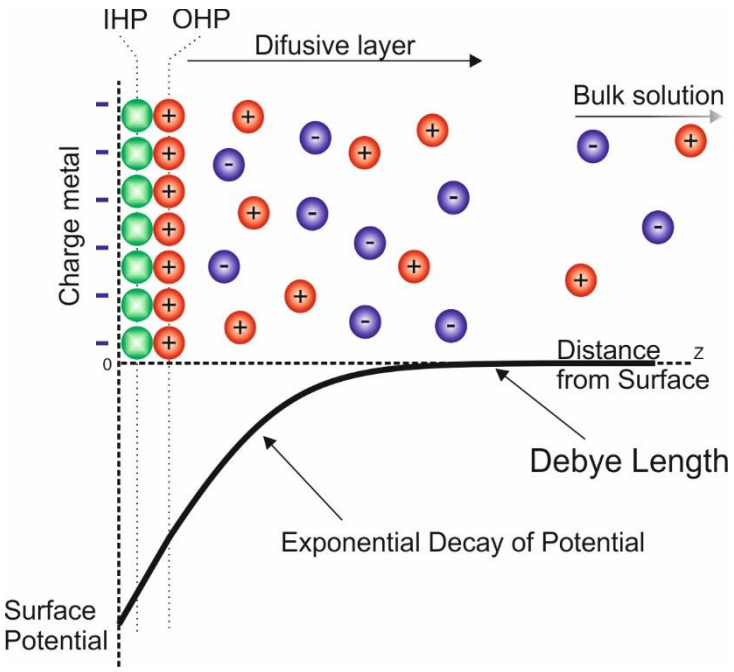

Figure 3.7 Cartoon of the electrical double layer developing on the charged metal interface, and the potential distribution throughout the liquid. Until the Outer Helmholtz layer (OHL) the potential drops linearly. In the diffuse layer, the potential drops exponentially until the Debye length. IHL: Inner Helmholtz Layer.

The electrical double layer is composed by a compact layer where ions adsorbed onto the object are due to chemical interactions, forming the Inner Helmholtz Layer (IHL). The solvated ions interact due to Coulomb force with the surface charge. The solvated ions closest to the electrode from the Outer Helmholtz layer (OHL) and beyond are the ions in the diffuse layer. The ions present in the diffuse layer electrically screen the surface charge of the metal, causing an exponential decay of the potential (created due to the surface potential of the metal). The distance at which the potential effect has decreased by $\frac{1}{e}$ from

the surface is the Debye length (κ^{-1}). This Debye length is on the order of few nanometres, decreasing with the increase of the electrolyte concentration as predicted by:

$$\kappa^{-1}(nm) = \frac{0.304}{\sqrt{c(M)}} \tag{3.10}$$

where c is the concentration of the monovalent ion in molarity (M). As an example, for a molarity of 1mM the expressed Debye length is ~9.6nm.

As in air, electrical measurements can be performed based on current sensing or force sensing techniques. The work performed in liquid is much more limited than in air due to the complexity it comprises. Two of the most current detection techniques used in liquid are:

1. **Scanning Ion-Conductance Microscopy (SICM):** This technique detects the change of current which is originated due to a change in the flow of ions entering a capillary probe. This flow of ions is dependent upon the distance between the probe's opening and the sample. This flow is dependent upon a basic physical exclusion; the closer the probe opening is to the sample, the smaller the region with liquid between the probe opening and the sample is, and hence fewer ions can flow inwards. This technique is restricted to insulating samples and electrolyte-containing solutions, and mostly used to obtain topographical images of large biological samples.
2. **Scanning Electrochemical microscopy (SECM):** In this technique the electrochemical behaviour of the sample is measured. This is measured from the faradaic currents caused from redox reactions occurring between the tip and the sample. Although it only senses redox reactions, with the adhesion of a turning fork to the ultramicroelectrode, topography can be obtained simultaneously with higher precision [51]. To increase resolution achievable and measure local electrochemical reactions, new electrodes have been developed, such as the use of modified AFM probes with smaller and closer sensing electrodes exposed to the surface (SECM-AFM) [52].

Under the force sensing measurements for electrical characterization in liquid conditions, we will focus directly on electrostatic force microscopy, since SPFM

is not adequate for topographically tall samples, and KFPM is no possible to be used under aqueous solutions [53].

3.4.1 Electrostatic Force Microscopy in liquid conditions

The electrostatic interaction under liquid environments is more complex than in air, being critically dependent upon the system and the conditions used to perform the measurements. The most basic system would be the use of an insulating probe, such as of silicon nitride. This insulating probe, as explained previously, will develop a static charge on its surface when introduced into a liquid. This charge would be dependent upon the chemical composition and pH of the environment, creating a double layer on the probe's surface. When the probe is approached toward the surface, the probe's double layer encounters the sample's double layer and an electrostatic force is created which can be sensed with common AFM systems. With this system, the surface charge of biological supported lipid bilayer membranes, single DNA molecules or bacteria have been studied [54–56].

In the same line, conducting probes can be used to detect surface charges. In this case, a static potential is applied between the probe and the base electrode to create a surface potential on the probe and the component space charge region. In this case, again, when the EDL regions overlap, a weak electrostatic force appears [57].

Dynamic electrical measurements (using AC voltages) have also been assessed under liquid conditions. *Hirata et al.* [58] used AC-EFM to detect local electrostatic forces of the sample at low ionic concentrations. The use of theoretical background used for air systems resulted in that the outcome of these forces detected are due to a combination of surface stress and the electrostatic forces [59,60] (Figure 3.8).

It was discussed later on that the use of higher frequencies cause the reduction of the electrical double layer's impedance (Z_c) according to:

$$Z_c = \frac{1}{\omega C} \tag{3.11}$$

where C is the capacitance of the electrical double layer. Since the capacitance of the electrical double layers are larger than that of the bulk and sample capacitance, the increase of the frequency will hinder the electrical double layers' capacitance but not of the bulk and sample capacitance. This will result on the EFM to principally detect the capacitance from the bulk and sample. This statement is restrained to the case where the probe-sample distance is greater than the Debye length. Frequencies (such as double the resonance frequency [53,61]) have been assessed, but measuring the dielectric properties of the sample to a local level still remained challenging. This has been attributed to the parasitic oscillations on the cantilever (induced by electrostatic forces and the surface stress) which hinder the local dielectric properties measured by the electrostatic force acting on the apex of the probe, and hence only extracting bulk capacitance (Figure 3.8). The use of ultra-short cantilevers or spherical probes increase the locality of the electrostatic forces, but brings by disadvantages such as low signal to noise ratio or large radius (losing spatial resolution), respectively [53].

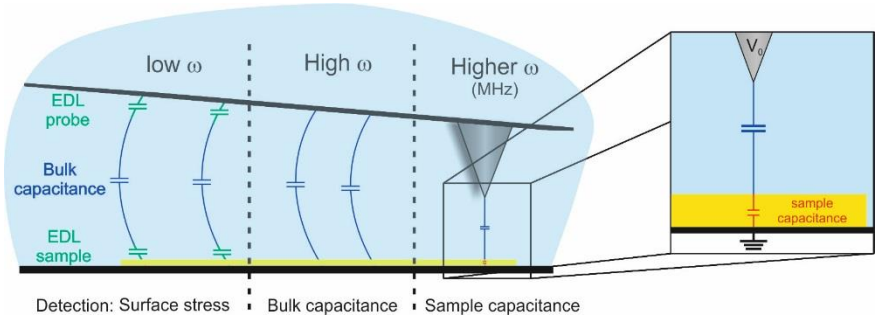

Figure 3.8 Schematic illustration of the sensed force by electrostatic force microscopy under liquid conditions dependent upon the frequency used. At low frequencies, the surface stress predominates in the interaction due to the presence of the EDL. At high frequencies (<MHz), the EDL effect is hindered and the bulk capacitance between the cantilever and the substrate is sensed. At higher frequencies (>MHz), the impedance of the bulk capacitance reduces drastically, allowing the detection of the sample's capacitance and hence local electrostatic measurements.

Members of the research group pushed forward the frequency used and increased up to the MHz range frequencies [62]. With the approximation of using a parallel plate model, and neglecting the EDL contributions as previously mentioned, the electric force acting on the probe are probe-sample distance dependent. This effect can be observed for frequencies greater than the actuation frequency (f_{act}) given by:

$$f_{act} = \frac{c\Lambda}{2\pi\varepsilon_0\varepsilon_{sol}}\left(\frac{\varepsilon z}{\varepsilon_{sol} h}+1\right)^{-1} \tag{3.12}$$

where c is the solution electrolyte concentration (mM), Λ is the molar conductivity, and ε_{sol} is the dielectric constant of the solvent. In the case of aqueous solutions:

$$f_{act} = 3MHz \cdot c(mM)\left(\frac{\varepsilon z(\text{nm})}{78h(\text{nm})}+1\right)^{-1} \tag{3.13}$$

showing that the actuation frequency for the probe apex is in the MHz range. At lower frequencies than f_{act} the applied voltage falls on the sample, where its impedance at these frequencies is much higher than the solution impedance. This creates no voltage drop on the solution under the apex, and hence no local electric force acting on the probe apex. Using frequencies higher than f_{act}, the bulk impedance from the cantilever is reduced and the electric force acting on a conductive probe in close proximity to a sample becomes local and sensitive to the local capacitance of the sample (Figure 3.8), where dielectric polarization properties can be extracted.

The high frequency voltage (*f*), which will be beyond the cantilever mechanical resonance frequency since it is in the MHz (not taking into consideration ultra-short cantilevers), causes a static bending of the cantilever due to the DC mode of the electric force. This force depends non-linearly on the applied voltage. A low frequency signal (f_{mod}), lower than the mechanical resonance of the cantilever, is applied between the conductive probe and the bottom of the sample to modulate the cantilever bending, giving rise to an increase in the signal to noise detection of the electrostatic forces. The electrostatic force detected at the first harmonic by this modulation frequency falls under:

$$\left|F_{elec}(z,f)\right|_{f_{mod}} \approx \frac{1}{4}\frac{\varepsilon_0\varepsilon_{sol} f^2\left(\frac{2\pi\varepsilon_0\varepsilon}{\Lambda ch}\right)^2}{1+f^2\left(\frac{2\pi\varepsilon_0\varepsilon z}{\Lambda ch}+\frac{2\pi\varepsilon_0\varepsilon_{sol}}{\Lambda ch}\right)^2}v_0^2 \qquad (3.14)$$

where v_0^2 is the amplitude of the applied voltage. The system is illustrated in Figure 3.9. Using this approach, members of the research group have been able to measure and quantify thin oxide films [63] and lipid bilayers [64] in electrolyte solution with nanoscale resolution.

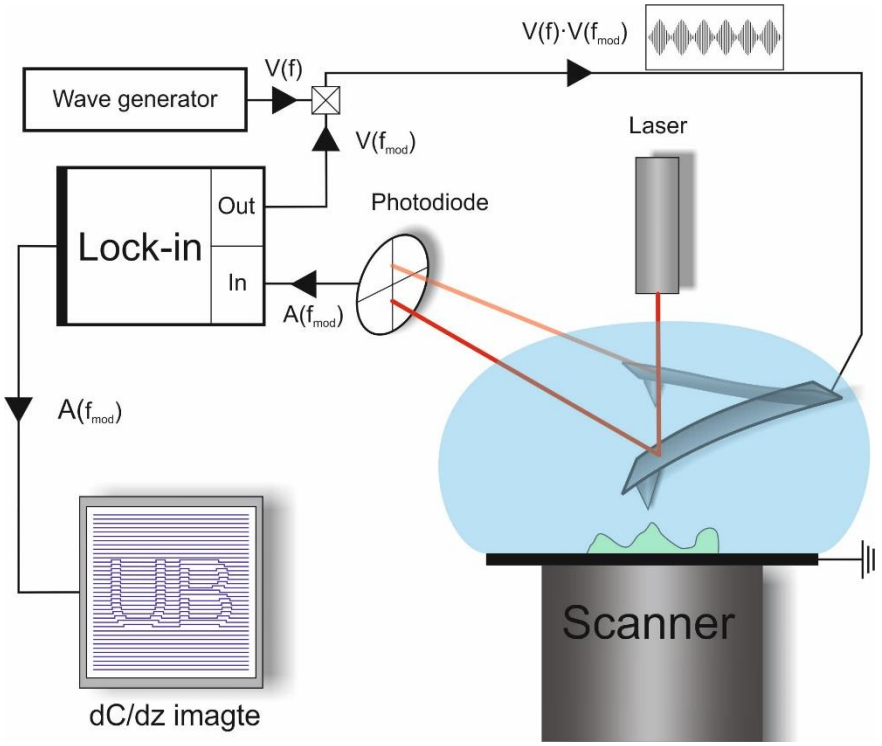

Figure 3.9 Schematic illustration of the AC-EFM in liquid for higher frequencies (MHz). A high frequency produced by a wave generator is modulated by a low frequency (produced by the lock-in), and applied onto the cantilever. The photodiode records the oscillation amplitude of the probe. The lock-in amplifier processes the oscillation amplitude of the modulating frequency to create the capacitance gradient image.

4 Nanoscale imaging of the growth and division of bacterial cells on planar substrates with the atomic force microscope

In chapter 1 we have shown that the use of the Atomic Force Microscope is emerging as a promising characterization technique for Nanomicrobiology. Due to the complexity of imaging living bacterial processes in their natural growing environments, improvements have come to a standstill. Here we show the in situ nanoscale imaging of the growth and division of single bacterial cells on planar substrates with the AFM. To achieve this, we minimized the lateral shear forces responsible for the detachment of weakly adsorbed bacteria on planar substrates with the use of the so called dynamic jumping mode with very soft cantilever probes. With this approach, gentle imaging conditions can be maintained for long periods of time, enabling the continuous imaging of the bacterial cell growth and division, even on planar substrates. Present results offer the possibility to observe living processes of untrapped bacteria weakly attached to planar substrates. This result is one of the goals of this work of thesis to further allow the electrical characterization of bacterial samples under liquid conditions.

This chapter reproduces almost literally the article: *Nanoscale imaging of the growth and division of bacterial cells on planar substrates with the atomic force*, ultramicroscopy **154**, 29-36 (2015) by M Van Der Hofstadt, M Hüttener, A Juárez and G Gomila. My contribution to this article was to produce all experimental results (from sample preparation to image acquisition), data analysis and manuscript writing and development in collaboration with my supervisor and rest of the authors.

4.1 Introduction

As we have mentioned in chapter 1, since the first images of dried bacterial cells were obtained with the atomic force microscope [41], this technique has significantly contributed to the understanding of the nanoscale structural and

physical properties of single bacterial cells [10,15,65–67]. Examples include the high resolution imaging of the dynamics of bacterial membrane proteins [68,69], the molecular recognition of cellular membrane proteins [39,70], the visualization of the effects of antibiotics on the cell surface [71,72], and imaging of the extrusion of bacteriophages [13]. In this way, the AFM has decisively contributed to the emerging field of Nanomicrobiology [10].

Imaging living bacterial cells with the Atomic Force Microscope still poses a major challenge. In chapter 3 we mentioned that this limitation arises from the relatively reduced adsorption forces of most living bacteria to the standard substrates used for AFM (such as glass or mica). In contraposition, the non-living bacterial cells (i.e. dried bacteria) show stronger adhesion forces, making imaging easier and extensively used [73,74].

Two different approaches have been reported to overcome the difficulty of imaging living bacteria. The first approach relies on increasing the strength of the forces that immobilize the bacteria to the substrates. The second approach is focused to reduce the shear forces exerted by the AFM tip on the bacteria and which are responsible for cell detachment during imaging. Among the first approach, we can find the physical entrapment of bacterial cells into polycarbonate filters [69,75] or microwells [42], or the use of specific substrate coatings (such as APTES [71], PEI [76], poly-L-Lysine [18,77], polyphenolic proteins [43] or gelatine [43,78,79]) or surface chemical binding groups (e.g. cross-linking of NH_2 groups via glutaraldehyde [80]). Concerning AFM imaging modes, conventional modes such as contact mode or dynamic mode can only be used when bacteria are relatively strongly attached to the substrates [81]. For weakly attached bacteria (for most coated planar substrates) the use of the intermittent contact mode with magnetically excited probes seems to offer the best performance [42,77,78]. This has been attributed to the fine tuning of the dynamic oscillation in liquid conditions.

Despite these developments, relatively little progress has been made in the nanoscale imaging of living bacterial processes, such as bacterial growth and division [42,75], especially for bacterial cells on planar substrates [77,82]. The use of planar substrates provides a more natural condition to study these bacterial processes. They offer a less constrained space (compared to physical entrapment methods) for bacterial growth and division, together with weak electrostatic adsorption forces. In this way, it mimics the bacterial natural way of adhesion

onto several types of substrates, including those present in biofilm formation on natural and synthetic surfaces [83,84]. In this article, we present the use of an alternative AFM imaging mode to study living bacterial cells, the so-called dynamic jumping mode. With this method, we have been able to image living bacterial cells weakly absorbed onto planar substrates, following its growth and division. When using dynamic jumping mode, the probe is oscillated at its resonance frequency and approached to the sample until a prefixed oscillation amplitude set point is reached. At this point, the probe is retracted a given distance and laterally displaced out of contact from the sample until the next point. This out of contact lateral displacement, together with the use of the intermittent contact mode and of soft probes, drastically reduces the shear forces exerted onto the weakly absorbed bacterial cells. It should be noted that dynamic jumping mode offers a better performance than its static version [85], which has already been widely used in the imaging of viruses on planar substrates in physiological conditions [86,87].

With the use of the dynamic jumping mode we have been able to image living single bacterial cells belonging to two different *Escherichia coli* strains, the MG1655 and the enteroaggregative (EAEC) 042, both being weakly adsorbed onto planar gelatine coated substrates. In addition, we have been able to monitor the growth and division of *E. coli* 042 in its native state over long periods of time.

4.2 Materials and methods

4.2.1 Cell types and cultures

Escherichia coli strain MG1655 is well known to be the common non-pathogenic laboratory *E. coli* strain for biological research [88], while strain 042 is the archetype of the EAEC pathotype [27,89,90]. EAEC strains display a characteristic aggregative or ‘‘stacked-brick’’ pattern of adherence to intestinal epithelial cells [1]. When grown at initial stages of biofilm, bacteria secrete less extracellular polymeric substance (EPS) [91].

Stock samples of the common laboratory strain *E. coli* MG1655 and the EAEC *E. coli* 042, were kept on Luria broth (LB) (Laboratiorios Conda, S.A.) agar plates at 4ºC.

4.2.2 Preparation of substrates for AFM imaging

Three types of substrates, namely, glass, gold and mica were used, in all cases coated with gelatine. Three different substrates have been used to show the generality of the approach presented and to evaluate any eventual effect of substrate roughness. Glass coverslips (No. 26024 Ted Pella, INC.) and gold substrates (Arrandee) were rinsed following a sequential sonication washing with acetone, iso-propanol and milli-Q water. Drying was performed with a nitrogen flow. The mica substrate (No. 52-6 Ted Pella, INC.) was freshly cleaved. The coating of the three substrates with gelatine was done with an adaptation of the protocol described in Ref. [78]. Briefly, the gelatine solution was prepared by dissolving 0.5g of gelatine (Sigma-Aldrich, G6144) and 10 mg of Chromium (III) potassium sulphate (Sigma-Aldrich, 243361) in 100mL milli-Q water. The resulting solution was heated up to 90ºC and left to cool down to 60ºC. The substrates were vertically dipped into the solution and allowed to air dry overnight inside a cabinet.

4.2.3 Sample preparation

For topographic imaging of bacterial cells, samples were prepared by using two different protocols. Protocol 1 used early stationary phase bacterial cells, obtained after an overnight cell culture. This is a standard microbiology protocol that ensures that bacterial cells have only small differences in growing times, collecting bacteria at the same growth phase. In this approach, the sterile loop was used to scrap a small quantity of bacteria grown on an agar plate into 10ml of LB, which was left at 37ºC at 250 rpm for 15 hours (overnight culture). 600 µl were then transferred into a micro-centrifuge tube and centrifuged at 3000 rpm for 3 min. The pellet was re-suspended in 600 µl milli-Q water. To attach cells onto the gelatine substrate, from the aliquot prepared, 40µl of the milli-Q

bacterial suspension were pipetted onto the gelatine substrate and spread using the help of the pipette tip. For dried samples, the sample was left until its complete dryness. For semi-dried samples, the sample was left to dry until the drop of water was not appreciable (but bacteria were not completely dry). For fully hydrated samples, the bacteria were allowed to deposit from the droplet of the solution for 30 min in a humid environment. The samples were rinsed in a soft stream of either 10mM HEPES buffer solution at pH 8 (imaging in liquid conditions) or with milli-Q water (imaging in dry conditions). Samples for liquid imaging were left in the buffer solution, while samples for dry imaging were left in dry conditions and imaged under nitrogen ambient flow (~0% Relative Humidity).

Protocol 2 used the *E. coli* 042 strain in early biofilm forming stage. Cells were directly grown on the imaging substrate. To achieve this, *E. coli* 042 strain was grown overnight in LB broth at 37ºC and 16µl were pipetted into a 12 well cell culture plate with a gelatine coated mica substrate at the bottom. The well contained 2ml of Dulbecco's Modified Eagle's Medium (DMEM, Invitrogen 11966025) supplemented with 0.45% of glucose. The culture plate was left to stand at 37ºC for 4 hours. Substrates holding the bacterial growth were softly rinsed with fresh growth medium (DMEM plus glucose) and either covered in it, or rinsed with milli-Q water and left to dry (in the case of the dried samples).

4.2.4 AFM imaging of bacterial cells

AFM topographic images in air were recorded in dynamic mode using Tap150Al-G probe (BudgetSensors) with a spring constant of 2.7N/m under nitrogen ambient flow (~0% Relative Humidity). The Cervantes microscope (Nanotec Electronica S.L.) was used at a scan speed of 0.7 Hz and 256 pixels per line.

Bacterial imaging in liquid media was performed using dynamic jumping mode plus (Nanotec Electronica S.L.) using Biolevers (BL-RC150VB-C1, Olympus) with a nominal spring constant of 0.03N/m. This innovative mode follows the jumping mode in liquid [92] with the modifications described in [85], and with the advantage of the acoustic oscillation [93]. Briefly, the probe performs a force vs. distance curve at each point of the sample surface in dynamic mode until the

prefixed oscillation amplitude set point is achieved. Due to the less invasive properties of the dynamic mode and the use of soft cantilevers, forces of <0.2 nN can be applied as set point, what turned out to be crucial when imaging weakly adhered living bacteria. Once reached the set point, the tip retracts a given distance to perform the raster scan of the tip at maximum tip-sample separation, avoiding shear forces when imaging, but maintain high control of the forces applied when imaging [94]. Scan speed was of 0.5Hz at 256 or 128 pixels per line scan, being independent of the scan size. Images were obtained at room temperature. A simple flatten was done to all images using WSxM 5.0 Develop 6.5 [95]

4.2.5 Viability assays

To assess the viability of bacterial cells, the commercial viability test Live/Dead BacLight from Invitrogen was used. This kit allows the labelling of nucleic acids, which is dependent on the membrane's permeability. A disrupted membrane means a dead bacterium, being this shown by a red fluorescent stain. An intact membrane is a living bacterium, which is shown by a green fluorescent stain. Viability tests were performed on the sample prepared in exactly the same way as for AFM imaging, with the only difference that after preparation, the freshly prepared viability test solution was added to cover the sample and left incubating for 15 min in the dark. Fluorescence images were done using a Leica inverted microscope DMIRBE. SYTO® 9 presents an excitation wavelength 480nm and emission 530nm, while propidium iodide an excitation of 485nm and emission of 630nm. We calculated the survival % by using image J. The plugin "analyze particles" was used to count the number of present dead and alive bacteria, independently, and then the % of living cells was calculated.

4.3 Results

4.3.1 Imaging bacterial cells on planar substrates in buffer solution

For further reference, we started the analysis by analysing the *E. coli* 042 strain grown according to protocol 1 in both dry and re-hydrated conditions. Figure 4.1A shows an image obtained under nitrogen ambient flow (~0% Relative Humidity) of a dried (and hence dead) bacterial cell on a gelatinized gold substrate. Dried cells presented a rod-shaped structure ~2 μm long and ~1 μm wide and with a maximum height ~261±6 nm (N=13), as obtained from cross-sectional profiles taken along the main bacterial axis (Figure 4.1B blue line).

When adding HEPES buffer solution at pH 8 to the dried dead bacteria, bacteria re-hydrated (Figure 4.1C). These bacteria still preserved the rod shape under buffer solution, presenting similar length and width, but a sensibly larger height (920±21 nm, N=13) (Figure 4.1B green line). The viability test done on these dried re-hydrated bacteria indicated that all bacteria were dead (Figure 4.1D).

The semi-dried bacteria sample imaged in buffer solution (Figure 4.1E), show a similar appearance to the dried re-hydrated sample. The topographic cross-section (Figure 4.1B purple line) shows that the bacteria height (920±26 nm, N=13) was similar to the one of dried re-hydrated bacteria. The viability test of the semi-dried bacteria (Figure 4.1F) illustrated a slight increase in the viability of this sample preparation, up to 30% of living bacterial cells are present as indicated by the green staining. Further on, we note that in both cases flagella can be observed as shown by the insets (Figure 4.1C and 4.1E for re-hydrated and semi-dried bacteria respectively), where the z-scale has been reduced to favour visualisation. Similar results have been obtained on gelatinized mica substrates and with the other strain considered in this study (data not shown).

In contrast to the samples described above, where some sort of drying process was involved, the observations of fully hydrated (living) bacterial cells could not be achieved with conventional imaging modes. Such images could only be reproducibly obtained with the use of the dynamic jumping mode with very soft cantilevers, since this method showed to exert very weak shear forces on the bacterial samples. In Figure 1G a topographic image of fully hydrated individual *E. coli* 042 bacteria on a gelatine coated gold substrate in HEPES buffer solution at pH 8 is shown. The rod shape of bacteria has been naturally preserved, with a height of 1084±32 nm (N=13) (Figure 4.1B red line). The height is slightly greater than the re-hydrated or the semi-dried bacteria. The viability test (Figure

4.1H) shows that more than 95% of the cells are viable. It should be noted that even if the bacteria are observed in HEPES buffer medium, which is depleted from nutrients, bacteria still remain alive for long periods of time. This is due to bacterial ability to survive under starvation conditions in its stationary phase.

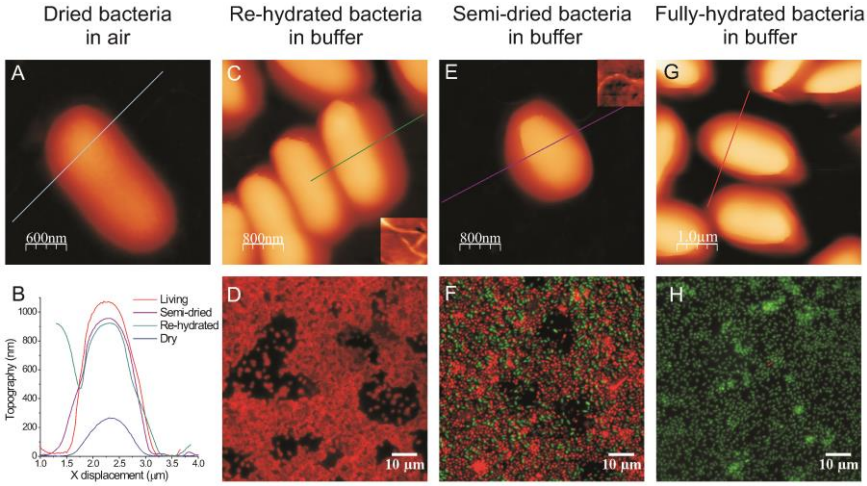

Figure 4.1 AFM images of individual *E. coli* 042 bacterial cells dried and imaged in dry conditions (A) and of re-hydrated cells (C), semi-dried bacteria (D), and fully hydrated bacteria (E) in HEPES buffer solution at pH 8. Insets show the presence of flagella. Figure 1B shows a comparison of the cross-sections taken along the lines indicated in the images: dried bacteria (blue line), re-hydrated bacteria (green line), semi-dried bacteria (purple line), and fully hydrated bacteria (red line). Fluorescence images from the viability kit stain for dried bacteria (D), semi-dried bacteria (F) and living bacteria (H), where green illustrates living bacteria and red dead bacteria. All bacterial cells are on a gelatinized gold substrate. Image in A was acquired in conventional dynamic mode and has a Z scale bar of 0.5µm. Images in figures C, E and G were acquired in dynamic jumping mode and have a Z scale bar of 1.5µm. In the insets the z scale bar is of 100nm.

AFM images of weakly absorbed *E. coli* 042 bacterial cells were also observed over other gelatinized substrates. Substrates used were common laboratory materials, for instance glass and mica (Figures 4.2A and B, respectively). When compared to those obtained on the gelatinized gold substrate shown in Fig. 4.1, images did not show any apparent structural differences. Images of the common laboratory strain *E. coli* MG1655 were also achievable on gelatinized gold

substrates (Figure 4.2C). No apparent structural differences between the living MG1655 and *E. coli* 042 bacterial cells were observed.

These results demonstrate the capability of dynamic jumping mode to image living bacterial cells weakly attached onto planar substrates.

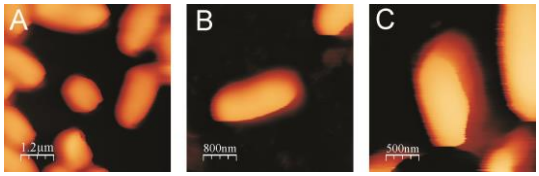

Figure 4.2 AFM images obtained using dynamic jumping mode of living individual EAEC 042 cells resuspended in HEPES buffer solution and deposited on gelatinized coatings of glass (A), and mica (B); and living individual MG1655 cells deposited on a gelatinized coating of gold. Z scale bar of 1.5µm.

4.3.2 Imaging living bacterial cells in growth medium on planar substrates.

The addition of nutrients to the HEPES buffer solution caused the irreversible detachment of both MG1655 and *E. coli* 042 cells. Bacteria grown following sample preparation protocol 1 could not be imaged with the presence of nutrients in the solution, being a handicap for the *in situ* observation of growth and division processes. To overcome this, the property of the *E. coli* 042 strain to form biofilm was then exploited. Biofilm grown samples seem to show a slightly stronger attachment to the substrates since they could be imaged even in the presence of a liquid solution rich in nutrients (sample preparation protocol 2).

As before, and for further comparison, these biofilm samples were firstly observed in dried conditions (~0% Relative Humidity) (Figure 4.3A). It was observed that they presented similar properties to the previously shown individual 042 cells, but forming aggregates of several bacteria. The viability test (Figure 4.3B) showed that, as in the previous experiments with sample preparation protocol 1, bacteria died during the drying process. The observation of the fully hydrated aggregate in HEPES buffer solution at pH 8 was not much

of an impediment (Figure 4.3C), where as in the corresponding cases shown before, bacteria remain alive due to its stationary transition capability (Figure 4.3D). A stronger adhesion between bacteria was observed on the biofilm growing on the gelatine-coated mica substrate since bacteria appeared close together and were less easily displaced. This increased the adhesion to the substrate and enabled higher resolution images to be taken, which clearly revealed the presence of a flagellum net interconnecting bacteria (Figure 4.3D). Finally, images of viable *E. coli* 042 bacterial cells in nutrient medium (DMEM + 0.45% glucose) could also be obtained (Figure 4.3E). A slightly smaller quality was obtained due to the smaller adhesion of the bacteria to the substrates in this medium, and eventually, due to an increased bacterial cell motility (which was confirmed from optical microscope videos, data not shown).

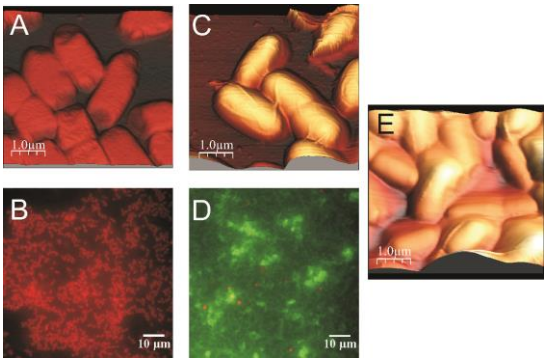

Figure 4.3 3D representation images of AFM images of dried *E. coli* 042 aggregation in dry conditions (A), of living EAEC 042 aggregation in HEPES buffer solution (C) and in growing medium (E) on gelatinized coatings of mica. Fluorescence images from the viability kit stain for the biofilm growth of a dried sample (B), and maintained under HEPES buffer solution (D), where green illustrates living bacteria while red dead bacteria. Imaging mode of A was done with conventional tapping mode while figure C and E were done in dynamic jumping mode, with all having a Z scale bar of 1.5µm.

4.3.3 Imaging bacterial growth and division on planar substrates

Images capturing the growth and division of *E. coli* 042 bacterial cells were obtained by continuously imaging the sample for long periods of time (up to 3 hours) in the nutrient medium (DMEM supplemented with 0.45% glucose). During this period of time, single bacterial cells' growth and division could be clearly observed and identified. In Figure 4 we present a sequence of error images showing the growth of two independent bacterial cells. It can be observed how the bacterium on the left of the images grows from an initial length of 1.8µm up to 2.7µm in ~84 min. The septum formation can be observed in the last two sequence images, as indicated by the black arrow. This bacterium seems to extend its growth towards the bottom of the image, as it can be seen from the reference given by the green dashed line, delimiting bacterial initial position and size (Figure 4.4). On the other hand, the bacterium on the right of the images starts with a larger initial longitudinal size of 2.1µm, and grows up to 3.6µm after ~79 min, where the septum has slightly formed. On the last image of this sequence, the new formed upper cell created after the septum formation was blurred. This is due to the moving capability of living bacteria, which makes difficult the imaging of bacteria which are not adhered to the substrate. On the ~94 min image, the cell on the top had disappeared and the lower right bacteria was still present (image not shown).

A detailed septum formation for another pair of bacterial cells is shown in Figure 4.5. It was observed that from the ~5 min image to the ~20 min image, the septum had formed; giving a time of ~15 min for septum formation under these conditions (room temperature around 24ºC). On the following images of this sequence, it can be observed how the septum was still present. The movement of living bacteria can also be appreciated in Figure 4.5, where the cell located at the right of the sequence of images had moved from a vertical position to a diagonal position, attracting itself to the other bacterium.

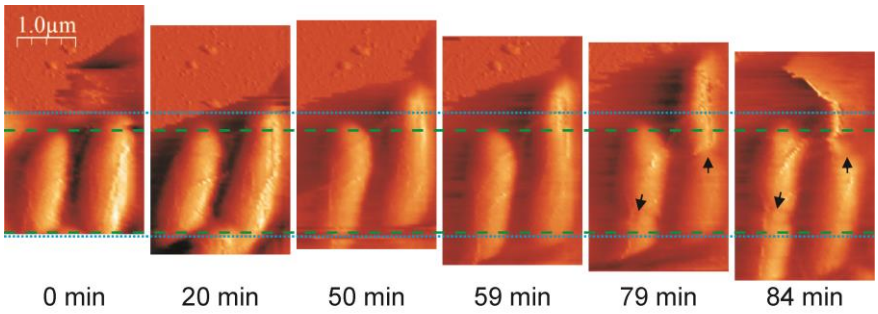

Figure 4.4 Time sequence AFM error images of growing *E. coli* 042 cells in nutrient medium (DMEM + 0.45% glucose) on gelatinized coatings of mica. The growth and the formation of the septum of two bacterial cells can be observed. The green dashed line delimitates the original size of the left bacterium, while the blue dotted line delimitates the original size of the right bacterium. Images have been moved vertically to correct drift error suffered during imaging in liquid. Arrows show septum formation.

4.4 Discussion

We have shown that the dynamic jumping mode implemented with soft cantilevers enables the nanoscale AFM imaging of viable and metabolically active bacteria on planar substrates. The use of weak forces (lower than 0.2 nN), together with the lateral displacement of the probe far away from the sample (which drastically reduces lateral shear forces) are at the basis of this capability. Based on the results obtained, this mode can be considered as an alternative to other existing AFM imaging modes for living bacterial studies (e.g. magnetically excited dynamic modes). The main advantage of the mode used here with respect to magnetically excited dynamic modes is that its implementation does not require of any hardware modification nor of any special AFM probe (as long as its spring constant is soft enough, typically below 0.05 N/m). This makes this technique be potentially implemented in almost any AFM system. Moreover, since imaging has been possible with both the *E. coli* 042 strain, and the common laboratory bacterial strain *E. coli* MG1655, we predict that it is quite likely that imaging can be achieved with many other bacterial types.

With the capability to image intact viable bacteria we have verified, once more, that aggressive preparation methods, such as drying processes, substantially alters the structure and viability of bacterial cells [96]. For instance, the dimensions of viable bacterial cells are almost identical to those expected for *E. coli* cells [97,98], while those of re-hydrated or semi-dried bacteria are smaller in height. Moreover, cell viability was strongly compromised when drying was involved (below 30% in the best-case scenario). We note that even when bacterial morphology remains almost intact, this is not a guarantee for viable cell imaging. Therefore, viability tests as complement to AFM imaging are required to confirm viable cell conditions, as also has been recently pointed out by others [77].

It is relevant to point out here that imaging of bacterial cells attached to a gelatine coated substrate under growing medium (i.e. actively growing bacteria) is much more difficult than under buffer solution (i.e. non-proliferating bacteria), as also reported elsewhere [43,77]. We hypothesize that the main reason for this difficulty has to be traced back to the motility properties of cells, whereas the reduced bacterial adhesion onto gelatine coated substrates by salts would play a smaller effect. In buffer media, the absence of nutrients drastically reduces both bacterial motility and growth, rendering stationary phase cells. Therefore, under these conditions, once attached to the substrate the bacteria remain immobile on it, facilitating its AFM imaging. Instead, in nutrient rich media the motility and growth resume, introducing additional "forces". These "forces", in addition to the force made by the AFM tip, can favour the detachment of the cells. This hypothesis has been supported from our optical microscopy observations of the samples in both media, where, when compared to buffer solutions, higher motility of the attached bacteria was observed in nutrient growth media (data not shown).

Both the gentle forces exerted by the dynamic jumping mode, and the ability of the *E. coli* 042 strain to generate confluent growth has helped to overcome the challenges of imaging bacteria in liquid solutions containing nutrients. In dry and buffer imaging conditions, we clearly observed the confluent growth and initial biofilm formation of 042 cells, with bacteria being in close contact (Figure 4.3C). Under these conditions, flagella were imaged, indicating that flagella are static. The absence of flagella movement could indicate that motility of bacteria can be considerably reduced when cells tend to aggregate. We note that bacterial motility is not fully suppressed under these conditions, as we have noted in Figure 4.5. This must be the bacterial natural behaviour since we are using a medium which mimics its natural ambient medium (human intestinal gut), and using a charged surface for its adherence (as reported previously [27]).

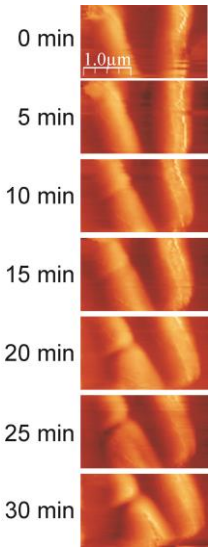

Figure 4.5 Time sequence AFM error images of growing EAEC 042 bacteria in its natural growing medium (DMEM + 0.45% glucose) for its aggregation growth on gelatinized coatings of mica. The formation of the septum in ~15min can be observed on the left bacteria, while the right bacteria shows the movement bacteria can express (from a vertical position to a diagonal one).

The ability of strain 042 cells to adhere to the flat surface made it possible to observe bacterial division (Figures 4.4 and 4.5) following a natural adhesion process onto a substrate, contrary to other methods observed up to now [75,77]. It was possible to obtain a sequence of several images showing a bacterial division, without drastically compromising image resolution (~40 nm). Increasing the resolution would have implied ~18 min per image, thus preventing a real continuous monitoring of the cell growth and division. In the present conditions a spatial resolution below ~20 nm could be achieved, which compares favourably with the theoretical prediction of ~10 nm achievable with amplitude modulated imaging modes in liquid and in soft samples under ideal conditions [99]. The sequence of error images of two independent adjacent bacteria growing and forming a septum for future division has been achieved as shown in Figure 4.4. It has been well established that the growing rate of bacteria is dependent on various factors, where for each bacterial cell the dividing rate could be different. This makes the extraction of the dividing rate difficult to normalize when predicted from AFM images on individual bacteria.

Since bacterial biofilms grow three-dimensionally [27,100], the newly formed bacteria are not exclusively restricted to a two-dimensional growth on the substrate. This phenomenon can be observed with the top bacteria formed in the division of the cell located to the right side in Figure 4.4. In this case, the newly formed top cell was not as firmly attached to the substrate as the cells located in the lower part of the image. The smudgy image observed had arisen from the metabolically activity of the bacterium, which makes it motile. The detachment of this newly generated cell on the top, clearly indicated that the division process had finished (image not shown).

The septum formation in Figure 5 corresponds to a duration of ~15 minutes, which corresponds to an average T period (the time difference between the time required for the initiation of envelope constriction and the generation time) as reported by other authors using other methodologies [101]. This reconfirms that the weak applied forces of the dynamic jumping mode allows the observation of the division process in its almost native state, enabling single cell analysis of bacterial growth and division.

Previous reported AFM studies on bacterial cell division required either the use of trapping pores [42,69,75]) or of the poly-L-lysine [18,77] with magnetically excited probes. Both attachments may compromise membrane integrity, and hence influence cellular physiology and division rate. We have tested static AFM imaging modes with a similar principle of making the raster scan out of contact, such as the static version of the jumping mode, without succeeding in obtaining good images in the case of living bacteria in a nutrient rich environment. Therefore, we conclude that the use of a dynamic mode is the key in obtaining the results reported. The methodology presented here enables observation of division in cells that are actively growing and not subjected to relevant torsion or attachment forces. As shown in Figures 4.4 and 4.5, a continuous sequence of cell elongation and septum formation can be obtained for individual cells. This methodology can therefore be used in the immediate future for single cell physiological studies about bacterial cell division.

4.5 Conclusions

We have shown that dynamic jumping mode AFM constitutes a powerful technique for the observation of physiological processes of viable bacteria that are weakly attached to biocompatible gelatinous coated planar substrates. Images of intact and viable bacterial cells have been obtained for cells suspended in buffer solution for two different *E. coli* bacterial strains on different substrates, thus predicting a wide applicability of this imaging method. We have observed that when imaging in nutrient media with bacterial cells on planar substrates is additionally challenging due to the inherent bacterial motility associated to the bacterial growth. These forces tend to detach bacteria from the substrates. We have circumvented these difficulties with the dynamic jumping AFM mode in the case of the *E. coli* 042 strain at the initial phase of biofilm formation. This method has made it possible to observe the bacterial growth and division, an event which has not been shown up to date with biocompatible gelatine coated substrates. These results open new possibilities in the in-situ observation of living bacterial processes at the single cell and nanoscale levels.

5 Nanoscale dielectric microscopy of non-planar samples by lift-mode electrostatic force microscopy

In chapter 3 we briefly explained the two imaging modes used to obtain Electrostatic Force Microscopy images. Among this two modes, lift-mode Electrostatic Force Microscopy is the most convenient imaging mode to study the local dielectric properties of non-planar samples. Here we present the quantitative analysis of this imaging mode. We introduce a method to quantify and subtract the topographic crosstalk from the lift-mode EFM images, and a 3D numerical approach that allows extracting the local dielectric constant with nanoscale spatial resolution free from topographic artefacts. We demonstrate this procedure by measuring the dielectric properties of micropatterned SiO_2 pillars and of single bacterial cells, thus illustrating the wide applicability of our approach from materials science to biology. This characterization is one of the goals of this work of thesis since it would allow to further use lift-mode EFM for topographically tall samples in a quantitative manner.

This chapter reproduces almost literally the article*: Nanoscale dielectric microscopy of non-planar samples by lift-mode electrostatic force microscopy*, Nanotechnology **27**, 405706 (2016) by M Van Der Hofstadt, R Fabregas, M C Biagi, L Fumagalli and G Gomila. My contribution to this paper was to produce all experimental results (from sample preparation to image acquisition) and manuscript development in collaboration with my supervisor and rest of the authors. Deconvolution and data analysis was performed by M C Biagi, and 3D modelling by R Fabregas.

5.1 Introduction

As we mentioned in chapter 3, in recent years a number of scanned probe microscopy techniques sensitive to the local dielectric permittivity properties of dielectric materials have been developed. Among them, we can cite nanoscale capacitance microscopy [102–104], electrostatic force microscopy (EFM) [46,48,105–109], nanoscale impedance microscopy [110,111], scanning

polarization force microscopy [112–115], scanning microwave microscopy (SMM) [116,117] and nanoscale non-linear dielectric microscopy [118]. These techniques have allowed measuring the electric permittivity with nanoscale spatial resolution on planar samples, such as thin oxides, polymer films and supported biomembranes [46,48,103–105], and on non-planar ones, such as, single carbon nanotubes, nanowires, nanoparticles, viruses and bacterial cells [21,45,49,119–126].

Despite these successful applications, using these techniques to study highly non-planar samples remains difficult in some cases. In particular, it is still a challenge to obtain the local dielectric permittivity properties of samples with large topographic variations in the range of hundreds of nanometres. The reason being that for these samples, measurements are taken with the probe following the sample surface topography (in contact, intermittent contact or by two pass modes, such as, 'lift' mode). As a consequence, the probe-substrate distance varies during the image acquisition, thus inducing spurious capacitance variations that are not related to the dielectric properties of the sample. That is, dielectric images of non-planar samples can be severely affected by topographic crosstalk [127–130].

Very recently, members of the research group have proposed a simple method to address this problem in the framework of scanning microwave microscopy [45]. It consists in reconstructing a dielectric topographic crosstalk image from the measured sample topography and a measured dielectric approach curve taken on the bare part of the substrate. By removing the crosstalk image from the measured dielectric image, one obtains an intrinsic dielectric image, which is closely related to the local dielectric permittivity properties of the sample, and which is directly amenable to a quantitative analysis with the help of finite-element numerical calculations.

Here, we generalize this approach to the case of lift mode Electrostatic Force Microscopy (EFM). We present the procedure to construct EFM topographic crosstalk images, to further generate intrinsic EFM images, which can then be directly interpreted in terms of the local polarization properties of the sample. Quantification of the resulting intrinsic EFM images is carried out by means of full 3D image numerical calculations. The procedure is demonstrated here on micropatterned SiO_2 pillars and to a single bacterial cell, in order to show the wide range of possible applications.

5.2 Topographic crosstalk in lift-mode EFM

Let us consider the typical case of lift-mode EFM images acquired in amplitude detection mode (a similar procedures can be applied to other EFM detection modes, such as frequency shift detection). In this two pass technique, in the first pass the topography of the sample is recorded in any AFM imaging mode, and in the second pass the EFM signal is recorded by lifting the probe at a fixed distance (lift), z_{lift}, from the sample surface. The EFM signal is obtained by applying an ac voltage of amplitude v_ω and frequency ω (far from the mechanical resonance frequency of the cantilever) on the conductive probe and recording the cantilever oscillation amplitude at frequency 2ω, $A_{2\omega}$. The oscillation amplitude is then related to the probe-sample capacitance gradient, dC/dz, through the well-known relationship:

$$\frac{dC}{dz} = \frac{4}{v_\omega^2} kA_{2\omega} \tag{5.1}$$

where k is the equivalent spring constant of the cantilever. From the capacitance gradient, quantitative information on the local dielectric permittivity properties of the sample can be obtained with the help of the appropriate theoretical model. A schematic representation of lift-mode EFM, with the definition of the more relevant parameters, is shown in Figure 5.1. Note that the lift path $z(\vec{x}) = h(\vec{x}) + z_{lift}$ follows the measured topography, $h(\vec{x})$, where $\vec{x} = (x, y)$ represents a position on the plane of the sample. In general, however, the measured topography is affected by tip-sample convolution effects (where tip is referred as the cone and the apex of the probe from here onwards) and may differ from the actual sample surface topography, $h'(\vec{x})$. For highly non-planar samples, tip convolution effects can be significant and they have to be taken into account.

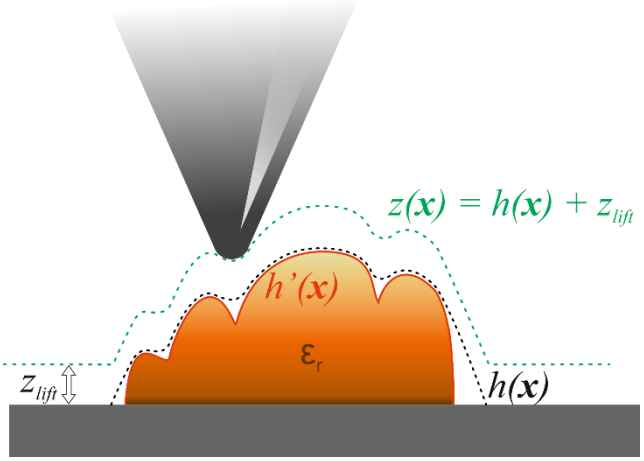

Figure 5.1 Schematic representation of the lift mode imaging with the definition of the main parameters.

Since electrostatic interactions are long ranged, the probe interacts, in general, with both the substrate and the sample. As a result, variations in probe-substrate distance occurring during lift mode imaging induce some capacitance gradient variations that also contribute to the capacitance gradient image. These capacitance gradient contributions, which we refer to as topographic crosstalk contribution, are independent from the dielectric permittivity properties of the sample and, hence, would be present even if the sample showed no electric polarizability (or the sample was not present). If $C'\left(\vec{x}, z; \varepsilon_r\right)$ is the measured capacitance gradient for a sample with dielectric constant, ε_r, when the probe is located at a distance z from the substrate at position $\vec{x} = (x, y)$, then the capacitance gradient topographic crosstalk at lift distance z_{lift} is given by

$$C'_{cross}\left(\vec{x}, z_{lift}\right) = C'\left(\vec{x}, h(\vec{x}) + z_{lift}; \varepsilon_r = 1\right) \tag{5.2}$$

By definition, the crosstalk contribution is a function of the lift distance z_{lift} and the measured topography, $h\left(\vec{x}\right)$, as well as, of the probe dimensions.

Given the topographic crosstalk contribution, we can subtract it from the measured capacitance gradient image to obtain, what we call, the intrinsic capacitance gradient image, $C'_{\text{int}}\left(\vec{x}, z_{lift}; \varepsilon_r\right)$, given by,

$$C'_{\text{int}}\left(\vec{x}, z_{lift}; \varepsilon_r\right) \equiv C'\left(\vec{x}, h(\vec{x}) + z_{lift}; \varepsilon_r\right) - C'_{cross}\left(\vec{x}, z_{lift}\right)$$
$$= C'\left(\vec{x}, h(\vec{x}) + z_{lift}; \varepsilon_r\right) - C'\left(\vec{x}, h(\vec{x}) + z_{lift}; \varepsilon_r = 1\right) \quad (5.3)$$

The intrinsic capacitance gradient image shows two useful properties, namely, it is different from zero on those parts of the image where the sample is present, and it is free from stray capacitance contributions (e.g. non-local cantilever contributions), since these contributions are subtracted. It should be noted, that the intrinsic capacitance gradient is still dependent on the sample geometry and dimensions since they determine the overall electric polarization of the sample, and hence, the force acting on the tip [127–130].

Experimentally the topographic crosstalk capacitance gradient image can be constructed following the procedure that we applied for the case of capacitance measurements in Ref. [45]. Briefly, one measures a capacitance gradient approach curve on a bare part of the substrate, $C'_{subs}(z)$, and then substitutes in it the probe-substrate distance, *z*, by the probe substrate distance during the lift imaging, $z_{lift} + h(\vec{x})$, thus giving the topographic crosstalk capacitance gradient image, i.e. $C'_{cross}\left(\vec{x}, z_{lift}\right) = C'_{subs}\left(z_{lift} + h(\vec{x})\right)$.

We illustrate these concepts in Figure 5.2 for measurements obtained on a silicon dioxide pillar ~236 nm height and ~5 μm wide microfabricated on a highly doped silicon substrate (AMO Gmbh). The images have been obtained with a commercial AFM system (Nanotec Electronica, S.L.) coupled to an external lock-in amplifier (Anfatec Instruments AG), in lift-mode by applying a voltage of amplitude 3V (rms) and frequency 2 kHz, and acquiring the cantilever oscillation amplitude at 4 kHz. CDT-CONTR doped diamond probes (Nanosensors) of spring constant 0.79 N/m and nominal tip radius ~100 nm have been used. Figure 5.2a shows the topographic image of the SiO_2 pillar, while Figure 5.2b shows a horizontal cross-section profile across the centre of the topographic image. A series of five lift-mode EFM capacitance gradient images obtained at lift distances 32 nm, 48 nm, 59 nm, 90 nm and 142 nm are shown in Figure 5.2c. Absolute values of the capacitance gradient are represented in the images. The precise value of the lift distance for each image, z_{lift}, has been

obtained by comparing the value of the capacitance gradient on a bare part of the substrate with the value obtained from an independently measured capacitance gradient approach curve on the substrate (square symbols and red line, respectively, in Figure 5.2g). The EFM images are converted to capacitance gradient images by using Eq. (5.1).

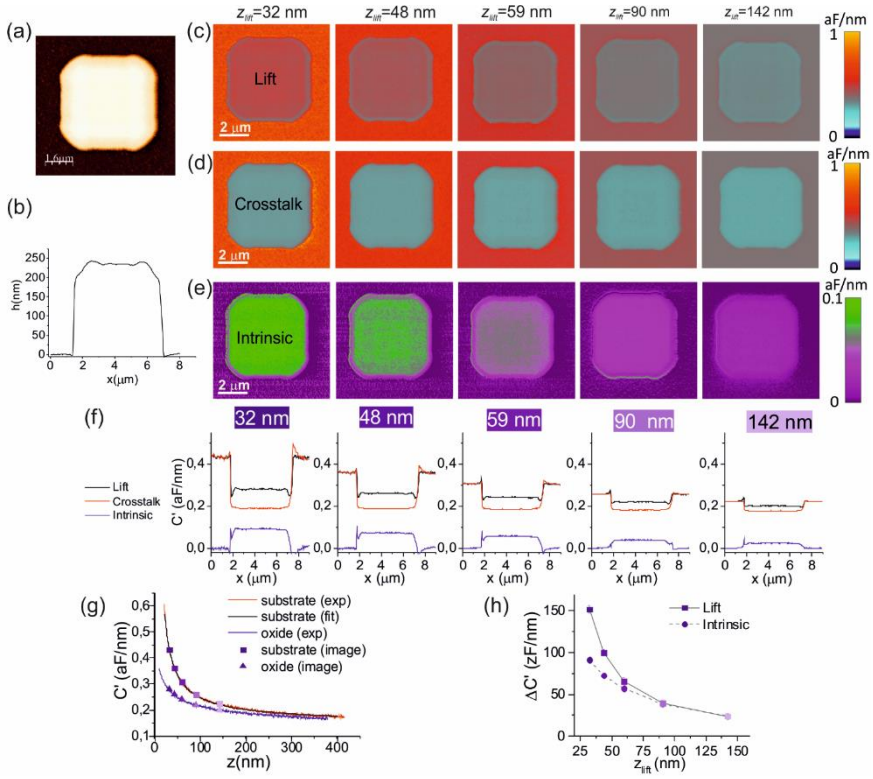

Figure 5.2 (a) Topographic image of a micropatterned SiO_2 pillar of height ~236 nm on a highly doped silicon substrate. (b) Topographic cross-section profile along the centre in (a). (c) Series of five 2ω-capacitance gradient images obtained in lift mode at lift distances of 32 nm, 48 nm, 59 nm, 90 nm and 142 nm, respectively. Note that absolute capacitance gradient values are shown. (d) Series of five topographic crosstalk capacitance gradient images reconstructed with the capacitance gradient approach curve measured on the substrate and shown in (g), red line, and the topographic image in (a), for each lift distance. Absolute values are shown. (e) Series of five intrinsic capacitance gradient images obtained from the subtraction of the capacitance gradient topographic crosstalk images in (d) from the measured

capacitance gradient images in (c). (f) Series of five sets of cross-section profiles along the centre of the images in (c) (black lines), (d) (red lines) and (e) (blue lines). (g) (Symbols) Absolute capacitance gradient values obtained from the images on the substrate (squares) and on the centre of the oxide (triangles) as a function of the lift distance. (Continuous lines) Measured capacitance gradient approach curves measured on the substrate (red line) and on the centre of the oxide (blue line). The black line is a least square fitting of the theoretical model to the approach curve on the substrate to calibrate the probe geometry giving a apex radius R=166±2 nm and a half cone angle θ=15.0±0.5º (see section 3). The theoretical curves are shifted by a fitted constant capacitance gradient offset of k_{stray}=0.128±0.002 aF/nm to account for stray effects associated to the cantilever and not included in the model. (h) Capacitance gradient contrast in the lift (square symbols) and intrinsic (circle symbols) images shown in (c) and (e), respectively, as a function of the lift distance (the lines are guides to the eyes).

For a given lift distance, the absolute values of the capacitance gradient (and hence of the electrostatic force acting on the tip) decrease when the probe moves from the substrate to the top of the pillar (see cross-section profiles in Figure 5.2f, black lines). We will show below that this decrease is strongly influenced by the fact that the probe-substrate distance increases when the probe moves away from the substrate to the top of the pillar (i.e. topographic crosstalk).

Moreover, when the lift distance increases, the absolute capacitance gradient values on both the substrate and the oxide decrease, as expected (see also cross-section profiles, black lines, in Figure 5.2f). This fact is explicitly shown in Figure 5.2g where we plot the capacitance gradient values on the substrate (square symbols) and on the oxide (triangle symbols) as a function of the lift distance (the error in the values is around ~0.002 aF/nm, smaller than the symbol). The values on the substrate (squares) overlap with the approach curve measured on it, since it is the condition to set the lift distances. The values obtained from the images on the oxide (triangles), once the lift distance has been adjusted with the substrate as mentioned, nicely overlap with an approach curve taken on the oxide (blue line in Figure 5.2g) without no adjustment, thus

confirming the stability of the measuring EFM set-up and the equivalence of both types of measurements. It can be observed that the capacitance gradient values on the substrate (squares) decrease more rapidly than those on the oxide (triangles) when moving away from the substrate. This fact implies that the contrast in the images also decreases when increasing the lift distance, as it is explicitly shown in Figure 5.2h where we plot the lift contrast values (square symbols) as a function of lift distance. In particular, the contrast greatly decreases at lift distances larger than ~100 nm in the present case.

With the help of the topographic image (Figure 5.2a) and the approach curve measured on the substrate (red line in Figure 5.2g), we have constructed the capacitance gradient topographic crosstalk images as explained above (equation 5.2). The results are shown in Figure 5.2d, together with the cross-section profiles in Figure 5.2f (red lines). These images show values and contrasts relatively similar to those of the lift images, thus confirming that topographic crosstalk contributes significantly to lift EFM images on highly non-planar samples. By subtracting the crosstalk images from the lift images (equation 5.3) we obtain the intrinsic capacitance gradient images (Figure 5.2e, note the change of range in the colour scale). As advanced before, the intrinsic capacitance gradient images show non null values on those parts of the image where there is the oxide, showing a positive contrast (see cross-section profiles in Figure 5.2f, blue lines). The contrast in the intrinsic capacitance gradient images decreases when the lift distance increases, as for the lift images, as shown in Figure 5.2h (circles). Note that, in absolute terms, the contrast in the intrinsic images is significantly smaller than that on the lift images, especially at short distances, (compare circles and squares in Figure 5.2h), as a consequence of the subtraction of the topographic crosstalk contribution.

We note that the intrinsic capacitance gradient images also show non-null contrast values on positions corresponding to the substrate close to the oxide pillar. This non-null contrast is due to long range electrostatic lateral effects that are detected by the tip when still on the substrate but close to the oxide pillar. These lateral long range effects are identified in the lift mode image as an increase in the capacitance gradient signal with respect to the signal on the substrate when the probe approaches the oxide pillar at short lateral distances (below ~200 nm in the present case).

5.3 Reconstruction and analysis of capacitance gradient images

Intrinsic capacitance gradient images provides a direct route to quantify the local electric permittivity of highly non-planar samples. First, it enables to directly visualize the homogeneity (or non-homogeneity) of the sample's dielectric properties not masked by topographic crosstalk artefacts. This allows one setting up theoretical models that already incorporate this information. For instance, in the case of the measurements performed on the oxide pillars a direct inspection of the intrinsic capacitance gradient images shown in Figure 5.2e confirms the uniformity of the dielectric properties of the pillars, which can then be assumed in the theoretical model. Furthermore, the use of intrinsic capacitance gradient images also enables one to use simplified probe models. In particular, in the present case, in which the substrate can be assumed to be metallic from the modelling point of view (it can be approximated by a constant electric potential surface given the high doping density of silicon), the cantilever does not need to be included in the numerical calculations of the intrinsic capacitance gradient images. The reason being that for metallic substrates the cantilever contribution is included in both the lift EFM image and the reconstructed crosstalk image, and hence it is automatically subtracted and does not contribute to the intrinsic capacitance gradient image. Note, however, that in the case of thick insulator substrates, the microscopic parts of the probe, such as the cantilever, induce some indirect effects in addition to the direct stray effect mentioned above, and some contribution from them need to be included in the model [126,131].

Based on this analysis, we calculate the intrinsic capacitance gradient images through the model system schematically depicted in Figure 5.3a. The tip is represented as a truncated cone of half-angle θ, and cone height H, terminating in a tangent hemisphere of radius R [131]. In addition, a disc of thickness W, overseeing the cone base by an amount L is located onto the cone base to model eventual local cantilever effects. As explained above, given that the substrate is metallic-like we do not need to include these effects in the present work, so we take $L = 0$ μm. The explicit tip geometry used in the calculations is determined by means of the tip calibration procedure described elsewhere [46,49]. Briefly, theoretical approach curves calculated for the tip on the bare substrate are least

square fitted to an experimentally recorded approach curve on the metal, with the apex radius, R, and cone angle, θ, as fitting parameters (other probe geometric parameters are fixed to nominal values: H=12.5 μm, W=3 μm, L=0 μm). A constant offset, k_{stray}, is also included in the calculated data (associated to non-local cantilever effects), and fitted together with the apex radius and cone angle. An example of a fitted curve is shown in Figure 5.2g, where the black continuous line represents the theoretically calculated curve that best fits the experimentally measured curve (red line). In this case, we obtain an apex radius R=166±2 nm and half cone angle θ=15.0±0.5º, with a constant offset k_{stray}=0.128±0.002 aF/nm.

The pillar oxide is assumed to have a physical shape and dimensions consistent with the measured topographic images, after proper subtraction of tip dilation effects. The tip dilation effects have been calculated for the tip geometrical dimensions (determined by the tip calibration process described above). Based on this analysis, the pillar has a thickness h=236 nm and a width w=5.2 μm, with round edges at the top and lateral sides (brown pillar in Figure 5.3b). The assumed pillar geometry provides an excellent agreement with the measured topographic image: see Figure 5.3c where we compare the calculated tip dilated profile of the assumed geometry (blue dashed line) with the measured topographic profile (symbols). For comparison, we also show the physical geometry of the pillar (red line) and the tip path when in lift imaging (green line). Finally, a uniform relative dielectric constant, ε_r, is assumed for the oxide based on the analysis of the intrinsic capacitance gradient images.

The capacitance gradient between the probe and sample is calculated by solving Poisson's equation with the finite element numerical software Comsol Multiphysics 5.2 (AC/DC electrostatic module). Poisson's equation solution results in the distribution of the static electric potential around the probe and in the sample, from which we derive the Maxwell stress tensor on the probe surface, and, by integration of it on the surface of the probe, we obtain the electrostatic force (see further details elsewhere [131]). The mesh was set to at least 200000 elements. An accurate process of optimization, validation and numerical noise reduction of the 3D simulations has been undertaken, in order to meet the experimental requirements and to enable the handling of 3D structures whose physical dimensions vary in more than three orders of magnitude.

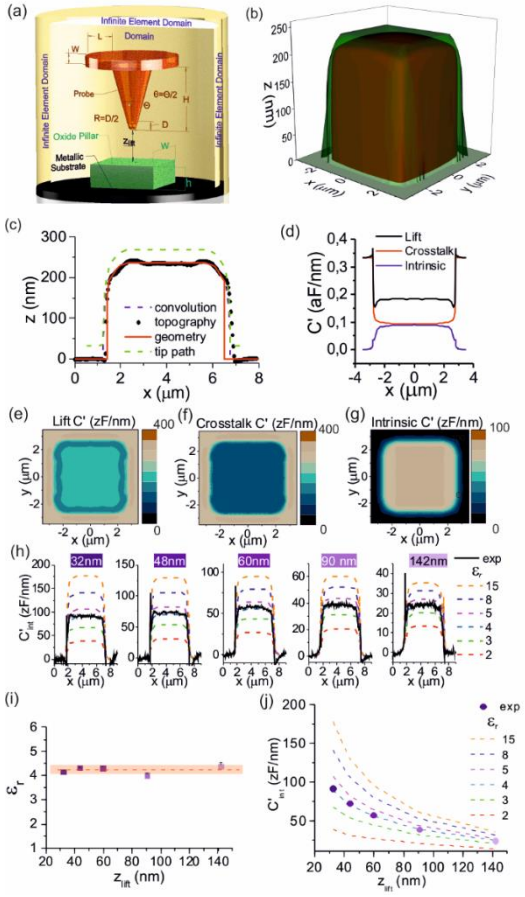

Figure 5.3 (a) Schematic representation (not to scale) of the system geometry modelled. Dimensions of the oxide pillar w=5.2 μm and h=236 nm. Probe geometry with calibrated radius R=167 nm and half cone angle θ=15º, and nominal values H=12.5 μm, W=3 μm, L=0 μm. (b) Green surface: ensemble of simulated lines representing the 3D probe movement over the oxide pillar (convoluted topography). The brown surface represents the actual oxide pillar geometry simulated. (c) Comparison of a measured topographic profile (symbols) with a tip convoluted profile (dashed purple) obtained for the pillar and tip geometries simulated (red line). Also shown the probe path followed during the simulations (green line) for a lift distance z_{lift}=32nm. (d) Transversal cross-section profiles along the centre of the numerically calculated images in (e)-(g), in absolute values. (e) Numerically calculated lift capacitance gradient image, (f) topographic crosstalk

capacitance gradient image (obtained by setting ε_r=1 in the simulations), and (g) intrinsic capacitance gradient image obtained from the subtraction of (f) from (e). (h) Series of numerically calculated intrinsic capacitance gradient profiles for different dielectric constants of the pillar (dashed lines) and different lift distances (from left to right 32 nm, 48 nm, 60 nm, 90 nm and 142 nm). Also shown the experimental intrinsic capacitance gradient profiles measured at each lift distance (continuous thick lines). For all distances the experimental profiles agree with ε_r ~4. The experimental profiles in the image are the average of 10 consecutive lines for better signal to noise ratio. (i) Extracted electric permittivity values resulting from contrast values obtained from the intrinsic capacitance gradient images in Figure 5.2e, as a function of lift distance. The average value obtained is ε_r ~4.2±0.2 (j) (Dashed lines) numerically calculated intrinsic capacitance gradient contrast curves on the centre of the pillar as a function of lift distance. (Symbols) Experimental contrast values obtained from the intrinsic capacitance gradient images. A least square fitting of the data gives ε_r = 4.1±0.2.

Lift mode capacitance gradient images $C'(\vec{x}, z_{lift})$ have been computed with the model geometry described above. To this end, software routines written in Matlab (Mathworks Inc.) have been used to move the probe in the simulations with respect to the pillar following the (convoluted) topographic profile at the set lift distance, i.e, $z(\vec{x}) = h(\vec{x}) + z_{lift}$ (green surface in figure 5.3b). Images of 45x51 points have been calculated. Images for the five experimental lift distances z_{lift} = 32 nm, 48 nm, 59 nm, 90 nm and 142 nm have been calculated. For each lift distance a range of dielectric constant values has been considered (ε_r=1−15). An example of a calculated capacitance gradient lift image for z_{lift}=32 nm and ε_r = 4 is shown in figure 5.3e, together with its cross-section profile in figure 5.3d (black line). Absolute values are shown. As it can be seen, the image shows the same trends as the experimental image, although the absolute values do not match the experimental ones, since the model does not include the non-local cantilever stray effects. By simply setting ε_r=1 in the simulations we can calculate the topographic crosstalk images. An example for z_{lift}=32 nm is shown in Figure 5.3f, together with a cross-sectional profile in Figure 5.3d (red line). Again, the qualitative trend is similar to the images derived from the experiments (see Figure 5.2), but a quantitative match is not obtained because of the reason mentioned above. Finally, by subtracting the topographic crosstalk capacitance

gradient images from the lift images we obtain the numerically calculated intrinsic capacitance gradient images. An example of a calculated intrinsic capacitance gradient image for z_{lift}=32 nm and ε_r=4, is shown in Figure 5.3g, together with a cross-sectional profile in Figure 5.3d (blue line). The image also shows a similar behaviour to the experimental intrinsic capacitance gradient images (Figure 5.2). In this case, the agreement with the experimental results is quantitative, since the intrinsic capacitance gradient image is not affected by non-local stray effects related to the cantilever (which as we have mentioned are not included in the theoretical model). Comparison of the experimental profiles obtained from the intrinsic images (black solid lines, same profiles as blue lines in Figure 5.2f) at the five lift distances considered with the theoretical ones (dashed lines) for different dielectric constants of the oxide are shown in figure 5.3h. For all lift distances the profiles approach the curves corresponding to ε_r~4, independently of the lift distance. The values obtained for the dielectric constants for the different distances is shown in Figure 5.3i. These values were derived by calculating the intrinsic capacitance contrast between the centre of the pillar (average of 300 pixels) and the substrate (average of 800 pixels) from the images in Figure 5.2e, and fitting these values with the corresponding theoretical contrast as a function of the dielectric constant, at each z_{lift}. The overall average value is ε_r=4.2±0.2. A similar value is obtained if one performs a least square fitting of the intrinsic capacitance gradient contrast in the centre of the pillar as a function of the lift distance, with the correspondingly theoretically calculated curves for different dielectric constants (see Figure 5.3j). In this case a value ε_r=4.1±0.2 is obtained. These values of the electric permittivity are in full agreement with the value usually reported for silicon dioxide, thus confirming the quantitative accuracy of the proposed procedure and, hence, validating it. We have further validated the method with the case of polystyrene nanoparticles of diameter ~300 nm, similar to the height of the silicon dioxide pillars. Also in this case, we obtain an excellent agreement between the extracted dielectric permittivity and the nominal value usually quoted for polystyrene (details are provided in the Appendix 5.7.3).

5.4 Application to a single bacterial cell

We show the usefulness of the proposed approach for the case of a sample showing a relatively complex non-planar surface geometry, namely, a single bacterial cell under dry conditions. In particular, we consider the case of bacterial cells of the *Bacillus Cereus CECT495* type, endospore forming bacteria, in an early sporulation state [132]. The bacterial cells have been grown following the procedure detailed in Ref. [33]. Briefly, an individual colony of *B. cereus* CECT495 was grown for 24h at 30ºC at 250 rpm in Trypticase soy broth. For early stage sporulation, 0.1 ml of the culture was added into 25 ml of G Medium [133] and incubated at 30ºC and 250 rpm for 8h. Sample was rinsed in milli-Q water at a low centrifugation (4 min, 4ºC and 4000rpm) and deposited on a gold substrate (Arrandee), previously cleaned following sequential sonication washing with acetone, isopropanol and water. Samples were allowed to dry in a cabin flow and imaged under nitrogen ambient flow (~0% Relative Humidity).

Figure 5.4a shows a 3D representation of the topographic image of the bacterial cell, together with longitudinal and transversal cross-section profiles. As it can be seen the bacterial cell surface topography is highly non-planar and, then, suitable for the analysis proposed here.

Besides the evident surface rough variations, the bacterial geometry approximately adapts to an ellipsoidal cap geometry. This fact is illustrated in the profiles shown in Figure 5.4a where we compare the tip convoluted profiles (purple lines, practically indistinguishable from the red lines) obtained from the convolution of the tip (with its calibrated geometry) and a cap ellipsoid of width w = 1499 nm, length l = 4496 nm and height h = 250 nm (red lines in the profile panels in figure 5.4a, see Appendix 5.7.1 for more details). We note that this geometry is very close to the hemiellipsoid geometry used in Ref. [21], but adapts slightly better to the geometry of the bacterial cell investigated here. The tip dimensions have been obtained from the calibration curve measured on the substrate shown in Figure 5.4b, giving R=115±1 nm, θ=30.0±0.3º and k_{stray}=0.108±0.002 aF/nm.

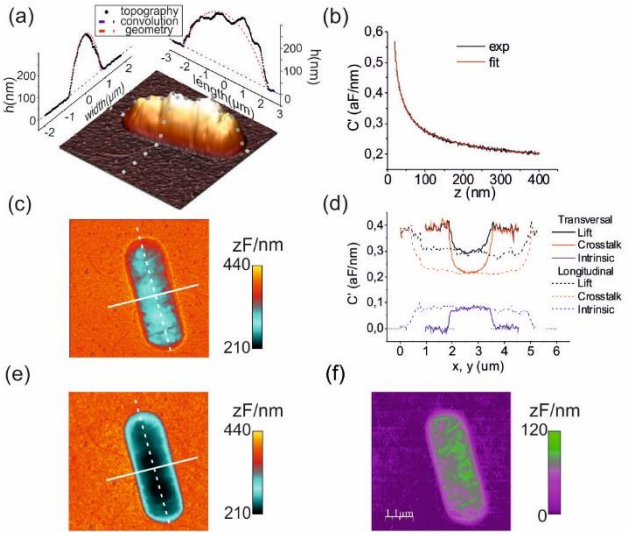

Figure 5.4 (a) 3D reconstruction of a topographic image of a *Bacillus Cereus* bacterial cell, together with transversal and longitudinal cross-section profiles. Also shown in the profiles panels the convoluted profiles (dashed lines) obtained from the convolution of the tip with an ellipsoidal cap of width 1448 nm, length 4456 nm and height 250 nm. (b) Capacitance gradient approach curve on the metallic substrate (symbols) and corresponding theoretical least square fitting curve (black line). The fits gives R=115±1 nm, θ=30.0±0.3º and k_{stray}=0.108+0.002 aF/nm. (c) Lift-mode capacitance gradient EFM image obtained at a lift distance of 38 nm. (d) Cross-sectional profiles along the lines in (b) (black lines), in (e) (red lines) and in (f) (blue lines). (e) Topographic crosstalk capacitance gradient image reconstructed from the topographic image in (a) and the approach curve in (b). (f) Intrinsic capacitance gradient image obtained from the subtraction of (e) from (c). Note the change in scale range with respect to (c) and (e).

Capacitance gradient lift-mode EFM images have been measured at five different lift distances, z_{lift}=38 nm, 49 nm, 60 nm, 79 nm and 127 nm. Figure 5.4c shows one example of a capacitance gradient lift-mode EFM image (in absolute values) acquired at a lift distance z_{lift}=38 nm. Similarly to the case of the oxide pillar, the absolute capacitance gradient decreases when moving from the substrate to the top of the bacterial cell (see the transversal and longitudinal cross sectional profiles in Figure 5.4d, continuous and dotted black lines, respectively).

In the present case we remark the presence of features in the electrical image on the bacterial surface. Whether such features correspond to bacterial inhomogeneities or to topographic crosstalk effects can be investigated by analysing the intrinsic capacitance gradient image. To obtain it, we first constructed the topographic crosstalk capacitance gradient image with the help of the topographic image shown in figure 5.4a and the capacitance gradient approach curve measured on the bare substrate (shown in Figure 5.4b, black line). The result is shown in Figure 5.4e, together with transversal and longitudinal cross-section profiles shown in Figure 5.4d (continuous and dotted red lines, respectively). As it can be seen, the topographic crosstalk image presents also electrical features on the bacterial cell surface, showing that most of the features observed in the lift capacitance gradient image come from topographic crosstalk effects. By subtracting the topographic crosstalk from the lift image, we obtain the intrinsic capacitance gradient image, shown in Figure 5.4f. The intrinsic capacitance gradient image shows a fairly uniform (compared to the previous images) and positive contrast indicating the lack of relevant electrical inhomogeneities. In fact, the intrinsic capacitance gradient transversal and longitudinal cross sectional profiles are fairly flat (Figure 5.4d, continuous and dotted blue lines, respectively), indicating the lack of contributions of both large and small topographic variations, as compared to the topographic profiles (Figure 5.4a) or lift capacitance gradient profiles (Figure 5.4d, black lines).

We quantified the intrinsic capacitance gradient images by means of 3D finite element numerical simulations by using a system geometry similar to the one used for the oxide pillars, but substituting the oxide pillar by a bacteria with an ellipsoidal cap shape (see Figure 5.5a). The dimensions of the bacterial cell are those obtained from the tip deconvolution analysis described above (w=1499 nm, l=4496 and h=250), and those of the tip, from the tip calibration procedure, also described before, (R=115±1 nm and θ=30.0±0.3º). Lift capacitance gradient images of 91x35 points following the bacterial cell lifted convoluted topography (green lines in Figure 5.5b) have been calculated for the five experimental lift distances z_{lift}=38 nm, 49 nm, 60 nm, 79 nm and 127 nm and different dielectric constants in the range ε_r=2–15. An example for the lift distance z_{lift}=38 nm and ε_r = 6 is shown in figure 5.5c. By setting ε_r=1 in the calculations we obtained the corresponding topographic crosstalk capacitance gradient images (see the one corresponding to z_{lift}=38 nm in Figure 5.5d). Subtracting the crosstalk from the lift capacitance gradient images, we obtain the intrinsic capacitance gradient

images (see the one for z_{lift}=38 nm and ε_r=6 in Figure 5.5e). The respective transversal cross-section profiles are shown in Figure 5.5f. Note the fairly flat profile of the intrinsic capacitance gradient image. The intrinsic capacitance gradient images can be compared directly with the experimental ones. In Figure 5.5g we show the calculated intrinsic capacitance gradient transversal profiles (dashed lines) at the different lift distances, for different dielectric constants of the bacterial cell, and compare them with the corresponding experimental intrinsic capacitance gradient profiles (black solid lines). From this comparison, we obtain ε_r~5–6. A more precise estimation for each lift distance is obtained by matching the average value obtained on the centre of the bacterium (60 pixels) with the corresponding theoretical values as a function of the dielectric constant of the bacterial cells. We obtain in all cases values in the range ε_r~5.5–6.5 (see Figure 5.5h) with an average value ε_r=6.0 ±0.3. A similar value (ε_r=5.8±0.3) is obtained from a least square fitting of the intrinsic contrast values as a function of lift distances with theoretically calculated intrinsic contrast curves on the centre of the bacterial cell for different dielectric constants (Figure 5.4i).

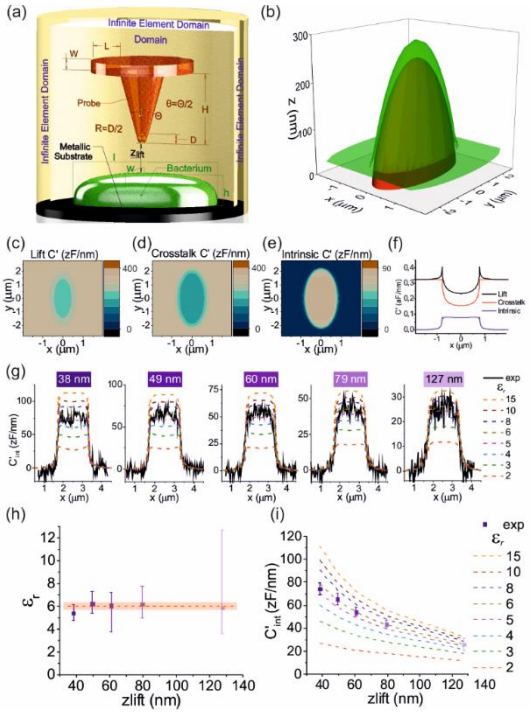

Figure 5.5 (a) Schematic representation (not to scale) of the system geometry modelled for the bacterium. Dimensions of the bacterium w=1.499 μm, l=4.496 μm and h=250 nm. Tip geometry with calibrated radius R=115 nm and half cone angle θ=30º, and nominal values H=12.5 μm, W=3 μm, L=0 μm. (b) Green surface: ensemble of simulated lines representing the 3D tip movement over the bacterium (convoluted topography). The red surface represents the actual bacterial cell geometry simulated. (c) Numerically calculated lift capacitance gradient image for z_{lift}=38 nm and ε_r=6, and corresponding topographic crosstalk capacitance gradient image (d), obtained by setting ε_r=1 in the simulations, and intrinsic capacitance gradient image (e), obtained from the subtraction of (d) from (c). Images are of 91x35 pixels. (f) Transversal cross-section profiles along the centre of the images in (c), (d) and (e). Absolute values are shown. (g) Comparison of the measured intrinsic capacitance gradient profiles at five different lift distances (continuous lines) with numerically calculated profiles for different dielectric constant values (dashed lines). (h) Extracted dielectric constant at each lift distance after matching the theoretical values to the experimental ones obtained on the centre of the bacterial cell. The average value is ε_r=6.0±0.3. (i) Intrinsic capacitance gradient contrast in the centre of the bacterial cells as a function of lift distance (symbols), compared with numerically calculated curves for different dielectric constants of the bacterial cell (dashed lines). The best agreement is found for ε_r=5.8±0.4.

5.5 Discussion

We have presented a method to quantify capacitance gradient EFM images obtained in lift mode on highly non-planar samples and to obtain the local dielectric constant of this type of samples. To this end, we have introduced the concept of intrinsic capacitance gradient image, which is obtained from the subtraction of the topographic crosstalk capacitance gradient image from the lift capacitance gradient image. The use of the intrinsic capacitance gradient images offers several advantages from the point of view of obtaining information on the local dielectric permittivity properties of non-planar samples and to extract quantitative values for their electric permittivity. First, it enables to directly

visualize the homogeneity (or heterogeneity) of the sample's dielectric properties not masked by topographic artefacts with the highest signal to noise ratio (i.e. with the tip as close as possible to the sample in all points of the image). This property is important as it allows inferring local dielectric permittivity properties of the sample not perturbed with topographic properties. Second, it enables to set up theoretical sample models that are well adapted to the actual dielectric permittivity properties of the sample (for instance, in the cases analysed here, both samples showed a relatively uniform dielectric response in the intrinsic images, what justified the use of uniform dielectric theoretical models). And third, it allows one to use simplified geometrical probe models, since the contribution of microscopic parts not related to the dielectric permittivity properties of the sample (e.g. cantilever) are subtracted from this type of images and they do not need to be included into the calculations.

The proposed approach offers clear advantages when applied to highly non-planar samples with respect to other approaches reported in the literature. For instance, we and other authors [49,104,127] have suggested the use of constant height imaging mode, in which the tip substrate distance is kept constant during image acquisition. This imaging mode produces electric images free from topographic crosstalk contributions and, hence, are also directly amenable to a quantitative interpretation in terms of the local polarizability of the sample [49,104]. However, for samples showing large topographic variations (in the hundreds nanometre or micrometric ranges) the constant height imaging mode only provides accurate electric information on the highest parts of the sample, since the remaining parts lie at a too large distance from the tip during the image acquisition. This fact prevents accessing the local dielectric properties in all parts of the sample with high accuracy. The use of lift mode imaging ensures the maximum sensitivity in all positions of the sample, and our analysis ensures the results are free from topographic crosstalk artefacts. We would like to highlight, however, that for planar samples or low dimensional non-planar samples (like nanoparticles, nanotubes, etc,) the use of constant height imaging mode can be preferred since the accuracy required (very often in the sub 1zF/nm) [49,125,126] cannot be offered by the reconstruction procedure presented here.

The proposed method has been validated with measurements on SiO_2 pillars, providing a value in excellent agreement with values quoted for high quality SiO_2 oxides ($\varepsilon_r \sim 4$). For the case of the *B. Cereus* bacterial cell, the value obtained

(ε_r~6) is slightly larger than the values reported earlier for other types of bacteria cells (*S. Thyphimurium, E. Coli, L. Sakey* and *L. innocua*) in the same dry conditions (ε_r~3–5) [21]. A possible explanation for the higher effective polarization of *B. Cereus* could be related to the initial sporulation state of the bacterial cell, in which the cell wall tends to thin and the DNA content (which shows a relatively large polarizability (ε_r ~8) [125]) tends to increase. Indeed, in this type of bacterial cell, after the triggering of spore formation due to harsh conditions, the first step is DNA replication [132]. After this step has ended, the replicated DNA goes to one end of the bacterial cell and it is encapsulated by spore layers until it becomes a mature endospore. At the early stage of spore formation we use (8h) it has been reported that the spore is not present yet, since it only appears at around 12h in sporulation medium [33]. Instead, a process of reduction/loss of the thick cell wall characteristic of gram positive bacterial cells is occurring, which manifest in a significant reduction in bacteria height from the usual ~500 nm in dry conditions to the ~265 nm observed by us.

Finally, we remark that for the geometry and dimensions of the bacterial cells studied here, the use of 3D numerical simulations is unavoidable in order to obtain accurate values of the dielectric constant (beyond their need to simulate full images and profiles). In our previous work, we used equivalent 2D axisymmetric models preserving the bacterial cell volume and height [21] (i.e. representing hemiellipsoids by equivalent hemispheroids). We will show below that this approximation is valid only when the aspect ratio of the bacterial cell is small (e.g. length:width<2:1), like those of the bacterial cells analysed in Ref. [21]. In the case of the *B. cereus* cells analysed here the length is nearly double (close to 4 μm) while the height and width are similar to the other bacterial types, thus giving an aspect ratio length:width>2:1. For these geometries, the 2D axisymmetric approximation are not accurate enough to enable extracting reliable dielectric constant values.

We show it explicitly in Figure 5.6, where we compare calculated capacitance gradient values on the centre of the bacterial cell at a lift distance z_{lift}=40 nm as a function of the dielectric constant of the bacterial cell, for different 3D hemiellipsoidal geometries (solid symbols) and their corresponding equivalent 2D hemispheroid geometries (empty symbols). The 3D bacterial cells have the same height h=250 nm and width w=1 μm, and different length (l=1, 2, 3, 4 and 5 μm). For the 2D geometries the radius of the equivalent hemispheroids are

R_{eq}=500 nm, 707 nm, 866 nm, 1000 nm and 1118 nm, respectively. The equivalent 2D model tends to slightly overestimate the capacitance gradient values as compared to the 3D model, providing values between 1% and 5% larger (see inset Figure 5.6a where we plot the relative error between both models as a function of the dielectric constant for the different bacterial lengths, and for different lift distances z_{lift}=20 nm, 40 nm and 80 nm).

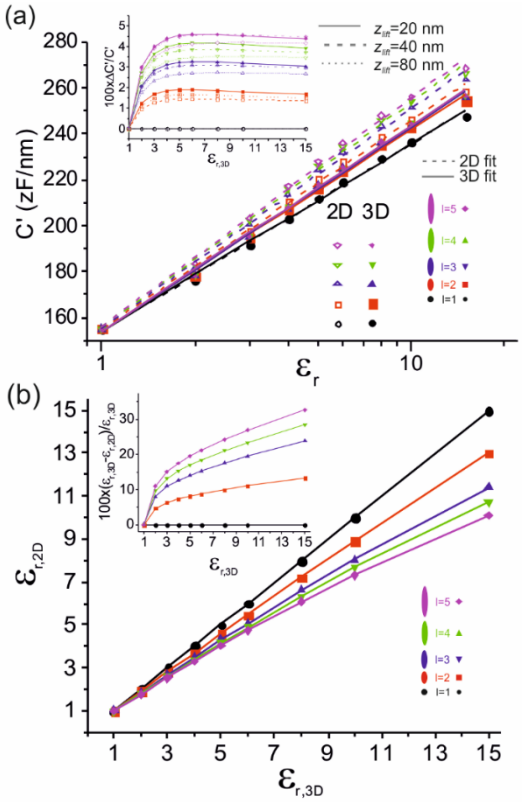

Figure 5.6 (a) Linear-log representation of calculated absolute capacitance gradient values on the centre of the bacterial cell as a function of the dielectric constant of the cell for different hemiellipsoidal geometries 3D (filled symbols) and their equivalent hemispheroid geometries with same volume and height 2D (empty symbols). The continuous and dashed lines represent linear-log fits of the calculated data. Inset: Relative error between the capacitance gradients calculated with the 3D and the 2D models as a function of the dielectric constant, for different bacterial lengths and three different lift distances, z_{lift} = 20nm, 40 nm and 80nm. (b) Dielectric constant extracted by using the 2D model

using as input data the values calculated with the 3D model as a function of the dielectric constant, for the five bacterial cells considered. Inset: Relative error on the extracted dielectric constant of the 2D model as a function of the dielectric constant for the five bacterial lengths considered. Tip geometry: R=150 nm, θ=15º, H=12.5, W=3 μm, L=0 μm. Bacterial cell geometry: width w=1 μm, height h=250 nm and lengths l=1 μm, 2 μm, 3 μm, 4 μm and 5 μm.

Even if the relative error in the calculated capacitance gradients is relatively small, the extracted dielectric constants show much larger errors between the two models. We show it in Figure 5.6b, where we plot the dielectric constant that would be obtained by using the 2D model to quantify the simulation data obtained with the 3D model (see also the inset where the relative error is calculated). We observe that only for small aspect ratios <2:1 for which the calculated capacitance gradients errors between the 2D and 3D models are below ~2%, the relative error in the extracted 2D dielectric constant is below ~10% (for ε_r<10), which is an acceptable uncertainty. However, for aspect ratios larger than 2:1 the relative error in the calculated capacitance gradients is above a ~2% and the relative error in the extracted dielectric constant can grow up to ~28% for the more eccentric geometries (l=5 μm). Such large errors can be avoided by using 3D models to quantify the measurements for these type of bacterial cells, as we did here. The reason why the extracted dielectric constants are so sensitive to the actual intrinsic capacitance gradient values is that they depend logarithmically on the dielectric constant (dashed and continuous lines in Figure 5.6a). This fact makes that the relative error in the extracted dielectric constant depends exponentially on the relative error in the calculated intrinsic capacitance gradients (see Appendix 5.7.2),

$$\frac{\Delta\varepsilon_r}{\varepsilon_r} \approx 1 - \exp\left[-\frac{\Delta C'_{\text{int}}}{C'_{\text{int}}} \ln\left(\varepsilon_r\right) \right] \tag{5.4}$$

5.6 Conclusions

We have presented a quantitative analysis of lift mode electrostatic force microscopy images for nanoscale dielectric characterization. We have shown that

for highly non-planar samples a significant contribution to the images comes from the topographic crosstalk associated to the variation of the tip-substrate distance while the probe tracks the sample topography. A method to subtract this contribution from the images has been presented. The resulting image has been shown to reflect more precisely the local dielectric properties of the sample. Application of this procedure to experimental results obtained on silicon dioxide pillars and on single bacterial cells fully confirm the need of the proposed method for quantitative analysis of the dielectric properties of highly non-planar samples. Present results are expected to be especially useful in samples showing large topographic variations, such as dielectric samples with high steps or single cells, where the topographic crosstalk contribution can mask the intrinsic dielectric response of the sample.

5.7 Appendix

5.7.1 Tip dilation analysis for a cap ellipsoid

For a cap ellipsoid corresponding to an ellipsoid of semiaxes *a*, *b* and *c*, buried under the surface a depth *d* (the hemiellipsoid correspond to *d* = 0), the coordinates of a transversal cross-section profile *z(x)* representing the convolution between the tip apex of radius *R* and the bacterial cell are given by:

$$z(x) = c \cdot \sin\alpha(x) - \frac{a}{2}\tan\alpha(x) \cdot \sqrt{\frac{R^2}{1+\left(\frac{a}{c}\tan\alpha(x)\right)^2}} - R - d \quad (5.5)$$

where only $z(x) > 0$ are considered and where the angle $\alpha(x)$ is found for any $x \in \left[-(a+R), a+R\right]$ from the roots of the equation of the centre *x* of the apex tangent to the cap ellipse in the point of abscissa $a\cos\alpha(x)$, i.e.,

$$x = a\cos\alpha(x) - \sqrt{\frac{R^2}{1+\left(\frac{a}{c}\tan\alpha(x)\right)^2}} \tag{5.6}$$

(Similarly for the *z(y)* profile, substituting *a* by *b*).

The deconvoluted dimensions of the cap ellipsoid are obtained by adjusting equation (5.5) to the measured topographic profile, by varying the parameters *b*, *c* and *d* (for the transversal profile) and *a*, *c* and *d* for the longitudinal profile, leaving the difference *c*–*d* fixed to the measured height. In particular, for the bacterial cell shown in figure 4.4a we obtained an ellipsoid of semiaxes *a*=1000 nm, *b*=3000 nm and *c*=740 nm, "buried" a distance *d*=490 nm.

The method holds true only if the contact point between tip and cap ellipsoid belongs always to the surface of the tip apex, and not to the cone surface. For a cone angle θ, this condition is mathematically verified if,

$$R\cdot(1-\sin\theta) \geq \frac{1}{\sqrt{\frac{a^2}{c^4}\cot^2\theta+\frac{1}{c^2}}} - d \tag{5.7}$$

5.7.2 Relative error in the extracted dielectric constants between 2D and 3D models

According to the calculations shown in Figure 5.6a, the intrinsic capacitance gradient in the centre of the bacterial cell for both the 3D and the 2D models follows an approximate logarithmic dependence on the dielectric constant for ε_r<10 (dashed and continuous lines in Figure 5.6a) i.e.,

$$\begin{aligned} C'_{\text{int},3D}(z,\varepsilon_r) &= C'_{3D}(z,\varepsilon_r) - C'_{3D}(z,\varepsilon_r=1) \approx b_{3D}\ln(\varepsilon_r) \\ C'_{\text{int},2D}(z,\varepsilon_r) &= C'_{2D}(z,\varepsilon_r) - C'_{2D}(z,\varepsilon_r=1) \approx b_{2D}\ln(\varepsilon_r) \end{aligned} \tag{5.8}$$

Here, b_{2D} and b_{3D} are parameters dependent on the geometry and probe sample distance but independent from the dielectric constant. The relative error in the calculated intrinsic capacitance gradients between the 3D and 2D models is then given by

$$\frac{\Delta C'_{\text{int}}}{C'_{\text{int},2D}} = \frac{C'_{\text{int},2D}(z,\varepsilon_r) - C'_{\text{int},3D}(z,\varepsilon_r)}{C'_{\text{int},2D}(z,\varepsilon_r)} \approx \frac{b_{2D} - b_{3D}}{b_{2D}} \tag{5.9}$$

which is approximately independent from the dielectric constant for ε_r<10 where the log-linear fit is correct (see Figure 5.6a). For a given intrinsic capacitance gradient value, $C'_{int,exp}$ the extracted dielectric constants from the two models would be

$$\varepsilon_{r,2D} = e^{\frac{C'_{\text{int,exp}}}{b_{2D}}} \quad ; \quad \varepsilon_{r,3D} = e^{\frac{C'_{\text{int,exp}}}{b_{3D}}} \tag{5.10}$$

The relative error of the 2D model with respect to the 3D one is then equal to

$$\frac{\Delta\varepsilon_r}{\varepsilon_{r,3D}} = \frac{\varepsilon_{r,3D} - \varepsilon_{r,2D}}{\varepsilon_{r,3D}} = 1 - e^{-\frac{\Delta C'_{\text{int}}}{C'_{\text{int},2D}}\ln(\varepsilon_{r,3D})} \tag{5.11}$$

where use has been made of equations (5.8)-(5.10). This result is precisely equation (5.4) of the main text.

5.7.3 Experimental data for the validation of the method on polystyrene nanoparticles

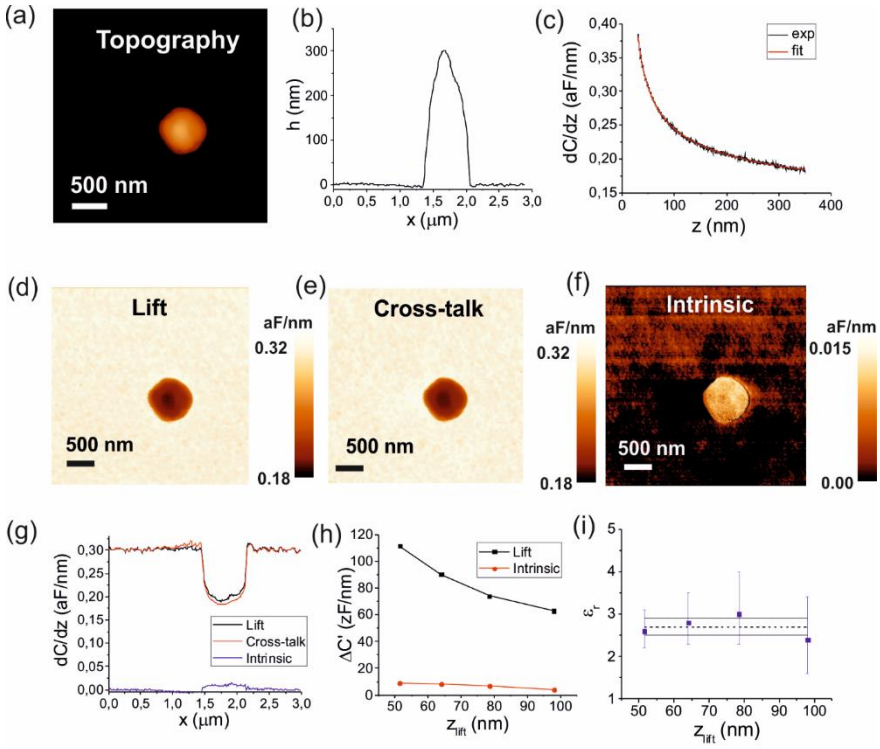

Figure 5.7 (a) Topographic image of a single polystyrene nanoparticle on a gold substrate and (b) corresponding cross-sectional profile along the centre of the nanoparticle. From the topographic image we obtain a height h~301 nm and a width (after tip deconvolution) w~390 nm. (c) Capacitance gradient approach curve on a bare part of the metallic substrate (black lines). The red line represents a least square fitting of the theoretical model to the experimental data, providing a tip radius R=99±1 nm, a cone half angle θ=27.4±0.3° and a stray capacitance gradient k_{stray}=0.098±0.002 aF/nm. (d) Capacitance gradient lift image of the nanoparticle shown in (a) obtained at a lift distance z_{lift}~51 nm. (e) Capacitance gradient cross-talk image obtained from the topographic image in (a) and the approach curve in (c). (f) Intrinsic capacitance gradient image obtained from the subtraction of (e) and (d). (g) Cross-sectional profiles along the centre of the nanoparticle in images (d) (black line), (e) (red line) and (f) (blue line). (h) Contrast of the capacitance gradient lift (black squares) and intrinsic (red circles)

images obtained at four different lift distances z_{lift}~51 nm, 64 nm, 78 nm and 98 nm. (i) Extracted dielectric constants from the measured intrinsic capacitance gradient contrast and the numerical simulation model, by using the measured tip and nanoparticle geometries, and the lift distances. The average value is ε_r=2.7±0.2 in good agreement with the nominal value for polystyrene ~2.5. Additional data: Spring constant of the probe *k*=0.55 N/m.

6 Subsurface capabilities of the Electrostatic force microscopy

In chapter 5 we showed that the electrical images obtained from EFM has information upon the intrinsic characteristic of the sample under study. In this chapter, we demonstrate the ability of the EFM to detect subsurface properties of samples. The technique has been tested on a calibration sample consisting of gold pellets buried under a SiO_2 matrix. Results show that for small lift distances, the EFM is capable of detecting buried structures separated by 200nm, and hence being capable of detecting, if any, the inner properties of the bacterial samples analysed in this work of thesis. This capability is of outmost importance to unravel the inner hydration properties, which is one of the main goals of this thesis.

6.1 Introduction

In Chapter 2 we demonstrated that although bacteria are considered a simple living organism, they present a complex structure. If we separate the bacterial structure into two major regions, the vegetative cell would be divided into the cytoplasm and the cell wall. On the other hand, the endospore cell would be divided into the core and the wall of protection (composed by the cortex and the coat principally). In both cases, the hygroscopic properties occur at the most exterior layer (the one in contact with the ambient), but the water distribution is not only dependent upon the outer layer; water molecules could be driven into the most inner parts of the cell. In order to observe if the bacterial endospores hydrate and where does this water content allocate, the chosen characterization technique must discriminate between properties observed from the inner parts with respect to the outer parts. To achieve such capability, a subsurface characterization technique with high resolution is needed.

One of the most used methodology to obtain high resolution images of subsurface structures is by performing slices of the sample and analysing the newly created surface [134]. The disadvantage of this approach is the damage

caused to the sample under study, and hence its inability to obtain information from living organism. An alternative approach to uncover subsurface properties of a sample is to use characterization tools which have penetration capabilities. Tools such as electron tomography, confocal microscopy, magnetic resonance imaging or X-ray tomography are the most common techniques. Due to their restriction to fixed organism, or the limited resolution they present, these techniques are inadequate candidates for subsurface characterization of single bacterial endospore samples.

When regarding subsurface characterization techniques with the AFM, various techniques have arisen to be promising, with the ability to conserve the nanoscale resolution. The use of ultrasounds [135], nanomechanical properties [136], infrared [137] or microwave [138] have shown promising results. Another penetrating technique, which is of special interest for us, is the EFM al low frequencies, where it has the capability to measure subsurface properties in a non-invasive manner [46,139,140]. The vast majority of the work regarding subsurface imaging with electric fields at low frequencies has been done with carbon nanotubes embedded in a known polymer resin [141–144], functionalized thiolate layer covered with a polystyrene film [145], or the use of viruses [49]. The ability to separate the surface properties from the subsurface properties when using the EFM makes it an appropriate technique to observe subsurface properties such as the hydration distribution of bacterial endospores.

The bacterial samples are composed of three basic organic compounds; lipids, proteins and DNA, which have low relative dielectric constant values, being ~2, ~4 and ~8 respectively [125]. With the presence of a homogenous distribution throughout the bacterial sample, the effective dielectric value quantified by the AFM probe at a given point of the sample would be a low value. If on the other hand there is a heterogeneous distribution, such as the presence of inclusions, the effective dielectric value quantified would change throughout the bacterial sample. This would be dependent upon the subsurface distribution and quantity of the organic compounds within the bacterial cell.

The relative dielectric constant value of water is ~80, an order of magnitude greater than the highest dielectric value of the organic compounds present in bacterial samples. The incorporation of water molecules would cause an increase on the effective dielectric value detected by the probe, and hence being able to appreciate hydration capabilities. The increase of the effective dielectric value

would be dependent upon the water absorbed and its localization, if retained by the surface layers or by the subsurface core.

In order to demonstrate the subsurface capabilities of the Electrostatic Force Microscopy, we used an inorganic sample consisting on pellets embedded on a silicon oxide matrix (ε_r ~4). The pellets are of gold, being in contact with a highly doped silicon substrate. The pellets are 50nm tall and covered by 50nm of the SiO_2 matrix (as specified by manufacturer) as represented in Figure 6.1a. The buried pellets consisted of different shapes and sizes as observed under scanning electron microscopy and optical images, Figure 6.1b and Figure 6.1c respectively. This layout mimics the situation of a bacterial vegetative cell, where in this case only the core has hydrated, being represented by the gold pellet, while the cell wall remains dry, represented by the SiO_2 matrix on top of the gold pellet. The samples have been developed within the V-SMMART EU project (participated by the research group) and are not currently commercially available from the company MC2 (France).

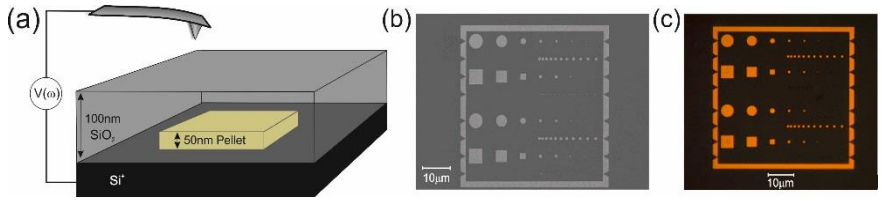

Figure 6.1 (a) Schematic illustration of the calibration sample used for sub-surface characterization capabilities of the EFM. (b) Scanning electron microscopy and (c) optical microscopy image of the inorganic sample.

6.2 Observing subsurface electric properties

The methodology we use to perform the electrical images with EFM is as described in chapter 5. Briefly, using a commercial AFM system (Nanotec Electronica, S.L.) topographical and capacitance gradient images were obtained using a CDT-CONTR doped diamond probe (Nanosensors) with a probe apex of ~140nm. On the first scan line, the topography of the sample is obtained with conventional AFM imaging tapping mode. During the second scan line, the

mechanical oscillation is substituted by an electrical oscillation at 2 kHz (with the addition of an external switch), and the probe follows the topography of the first scan line at a given lift distance. The electrical amplitude is collected by an external lock-in amplifier (Anfatec Instruments AG) to obtain the electrical capacitance gradient image. To extract the lift distance of the electrical image, capacitance gradient approach curves have also been measured on given points of the sample as explained in chapter 5. From the absolute values of the electrical image and the curves, the lift distance at which the EFM images are acquired can be calculated.

The first sample is composed of square gold pellets with a length of 4μm (as specified by manufacturer). The topographical image reveals the presence of a slight depression of the SiO_2 matrix, where this has been attributed to the subsurface presence of the buried gold pellet (Figure 6.2a). An average depression of only ~2.5 nm, with a length of 4.22 μm ± 0.03 μm, is extracted from cross-section analysis (Figure 6.2b). The surface roughness presented by the SiO_2 matrix is fairly flat, presenting a RMS roughness smaller than 1.3 nm. These small irregularities have small contribution on the capacitance gradient images.

The obtained lift-mode capacitance gradient image at a lift distance of ~34 nm for the corresponding topographical image is shown in Figure 6.2c. Absolute values show that a greater capacitance gradient is obtained where presumable the gold pellet is buried. This increase is attributed to the presence of the gold pellet, which causes an increase on the effective dielectric constant detected by the probe. The cross-section profile (Figure 5.2d) shows an increase of the capacitance gradient by ~40zF/nm, where the noise irregularities are due to topographical effect (Figure 6.2b), but being less significant than the effect caused by the buried gold pellet.

The greater the probe-sample distance is, the less localized the signal is to a given point of the sample. This can be clearly observed on the EFM capacitance gradient image obtained at a lift distance of ~98 nm (figure 6.2e). At this distance, the buried gold pellet is merely observed, with only a slight contrast of ~6zF/nm (Figure 6.2f). It is interesting to point out, that at this distance, the probe's apex is separated from the buried gold pellet by ~148 nm. This separation distance is in the range of the spore's outer wall protection thickness, showing the capability of the EFM to detect the hydration of bacterial endospore's inner core.

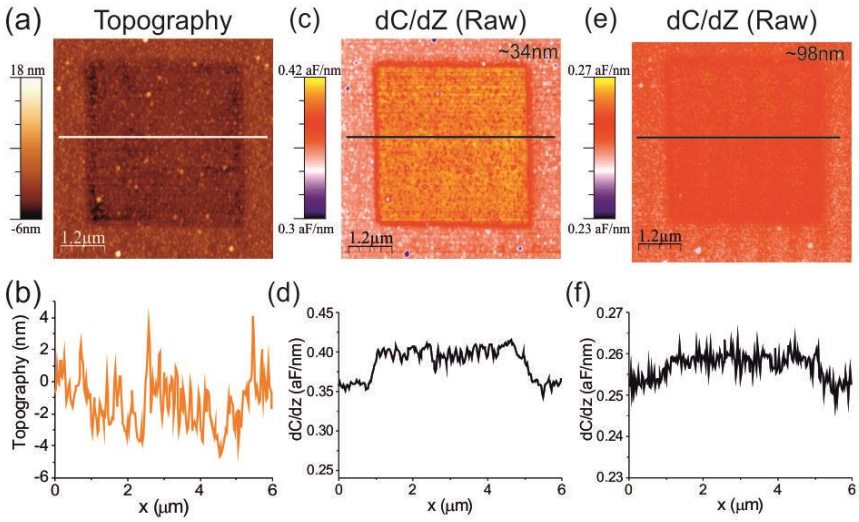

Figure 6.2 (a) Topographic image of the region where the 4 µm length gold pellet is presumably buried. (b) Cross-section profile along the white line in (a). (c) Capacitance gradient image for the matching topographical image at a lift distance of ~34 nm from the surface. (d) Cross-section profile along the black line in (c). (e) Capacitance gradient image at a higher lift distance, ~98 nm. (f) Cross-section profile along the black line in (e).

6.3 The lateral resolution of the EFM at the subsurface level

One of the main issues in the subsurface characterization is the lateral resolution achievable. This is of interest especially in cases where there could be a heterogeneous distribution within a sample. To detect the lateral resolution, we firstly used a sample composed of two buried gold disc pellets of 1 µm in diameter, which are separated 200 nm between them (as specified by manufacturer). In this sample, as in the previous case, there are topographical effects on the surface which help to locate the buried gold pellets (Figure 6.3a). The depression observed in this case is of only ~3.5nm, a value still small to present significant electrical contribution. From surface topography, the

extracted diameter of the buried gold pellet is of ~1.15 μm, while the separation distance is of ~156 nm (Figure 6.3b).

The obtained lift-mode capacitance gradient image at a lift distance of ~35 nm for the corresponding topographical image is shown in Figure 6.3c. The yellow circle on the image has a diameter of ~1.01 μm, and hence corresponds to the region of the buried gold pellet. The red halo surrounding the yellow circle is the capacitance gradient caused mainly by the depression of the sample. This is observed in the topography cross-section (Figure 6.3b) at the 2 μm position where there is no change in the depression while there is a change in the capacitance gradient signal due to the absence of the buried gold pellet (Figure 6.3d). From this change, the predicted subsurface separation between the buried gold pellets by EFM images is calculated to be ~220 nm, which is in closer agreement to manufacturer's values than the predicted from surface topography (~156 nm). For higher lift distances ~99 nm (Figure 6.3e) the buried gold pellets are still observed, but the separation between them is just slightly detected (Figure 6.3f).

The lift distance used for this measurement are virtually identical to the lift distance used for the 4 μm squared pellet. As in the previous case, a contrast observed between the buried gold pellet and the SiO_2 matrix is of ~40zF/nm for the closer lift distance, while ~6zF/nm for the furthest lift distance. This shows the capability of the EFM to measure subsurface properties with good reproducibility.

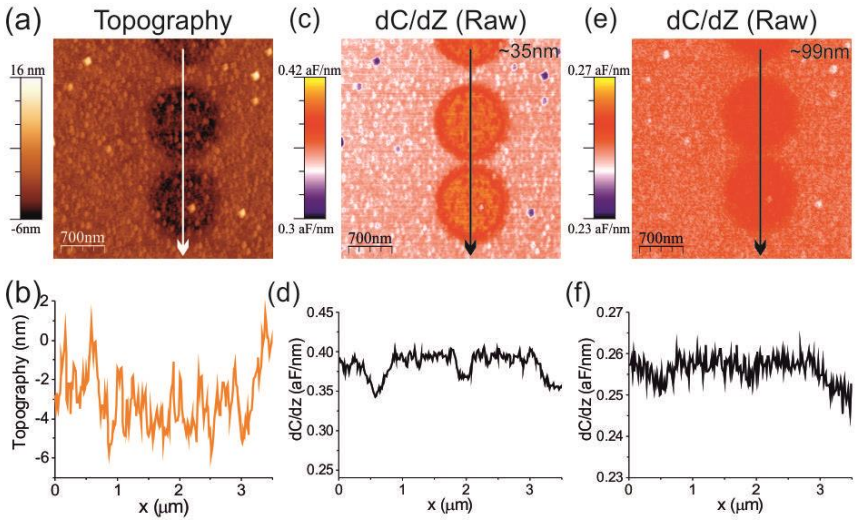

Figure 6.3 (a) Topographic image of the region where the 1 μm length gold pellets are buried and separated by 200 nm. (b) Cross-section profile along the white line in (a). (c) Capacitance gradient image for the matching topographical image at a lift distance of ~35 nm from the surface. (d) Cross-section profile along the black line in (c). (e) Capacitance gradient image at a higher lift distance, ~99 nm. (f) Cross-section profile along the black line in (e).

Bacterial samples, such as the endospores or the vegetative cells, are just in the range of the micrometre, so the presence of a micrometre structure in its interior is unlikely. The existence of structures in the order of few tens to hundreds of nanometre is more likely, such as the inclusion in bacterial vegetative cells. For this reason, we use a smaller size buried gold pellets to resemble the hypothetical case of an internal inclusion hydrating more than the cytoplasm. This sample is composed of 200 nm diameter gold discs which are buried under the SiO_2 matrix, and separated by 200 nm in distance. The AFM topographic image of the surface reveals a depression of ~5 nm with a very unfavourable topography (Figure 6.4a). The predicted separation distance of the buried gold pellets from surface topography is of ~195 nm, but the extraction of the disc diameter is too irregular to extract an objective result (Figure 6.4b).

Capacitance gradient image at a lift distance of ~34 nm reveals that buried objects as small as 200 nm in diameter can still be observed (Figure 6.4c). In this case, a slightly greater contrast of ~51zF/nm is detected between the presence

and the absence of the buried object (Figure 6.4d). As the lift distance is the same as for the previous results, and the capacitance gradient at the SiO_2 matrix is almost identical, we attribute this higher value to the increase in the depression of the surface topography. Nevertheless, the contribution due to the presence of the buried gold pellet is still greater than due to the presence of the depression on the surface.

The diameter of the buried gold pellets extracted from capacitance gradient image at ~34 nm is of ~154 nm, while the separation distance of ~248 nm. This underestimation and overestimation, for diameter and disc separation respectively, comes from the lateral effects of EFM, since the observed buried gold pellets are in the range of the probes apex radius and lateral effect must be taken into consideration [48]. At larger lift distances, such as ~112 nm (Figure 6.4e), the 200 nm buried gold pellets are just visible, with a contrast as low as ~5zF/nm (Figure 6.4f). At such high lift distances, the effect due to small depressions on the sample are less visible, being usually hidden within the error of the measurement. Furthermore, the separation of the disc on the capacitance gradient image is just slightly intuited, where the ability to discern between the two discs at this lift distance must be judge with precaution.

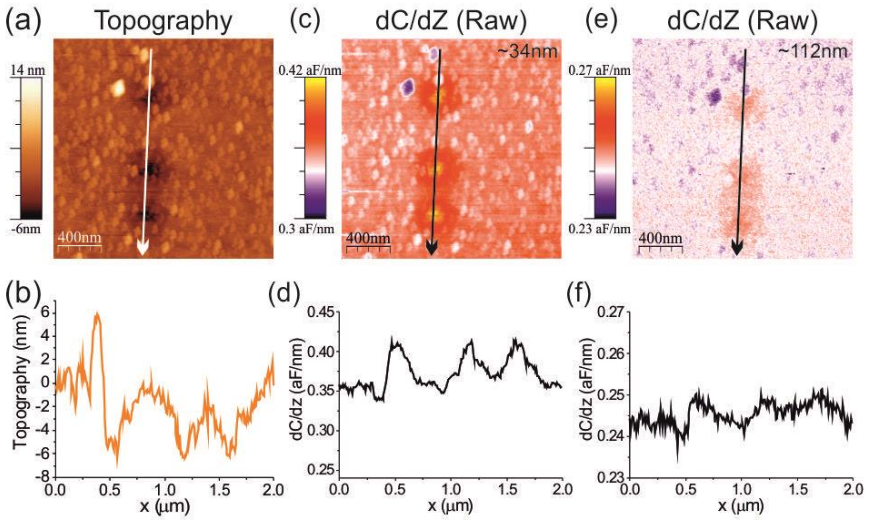

Figure 5.4 (a) Topographic image of the region where the 0.2 μm length gold pellets are presumably buried and separated by 200 nm. (b) Cross-section profile along the white line in (a). (c) Capacitance gradient image for the matching topographical image at a lift distance of ~34

nm from the surface. (d) Cross-section profile along the black line in (c). (e) Capacitance gradient image at a higher lift distance, ~112 nm. (f) Cross-section profile along the black line in (e).

6.4 Conclusions

We presented in this chapter the ability of the EFM to resolve subsurface properties down to the nanoscale level with the use of an inorganic sample. The sample is of great interest for this work of thesis due to its close approximation to a system where only the core has hydrated. We have observed that samples down to 200nm in size and buried 50nm under the surface can be detected independently from surface morphologies. This is of similar nature as bacterial vegetative cell wall, where the thickness is in the range of the covering matrix, and the gold pellet's size are in the range of possible heterogeneous hydration patterns due to the presence of inclusion in the bacteria. For large lift distances, the system resembles closer to the bacterial endospore cell outer protective wall, where the thickness is in the range of the probe-gold pellet distance. At this distances, subsurface properties can still be detected, and hence detecting hydration of the endospore core is achievable. The resolution of the 200nm separation between the two small buried gold pellets at high lift distances is in the border of resolution. Nevertheless, as chapter 2 shows, the spore presents a homogeneous circular distribution, so the expected hydration would also be homogeneous.

This method has shown its stability by obtaining repetitive contrast at nearly identical lift distances, showing the large potential of the EFM to observe internal hydration properties of bacterial vegetative and endospore cells.

7 Validation of EFM under liquid conditions for topographically tall samples

In chapter 3 we described that local electrical images under liquid conditions have been restricted only to small sized thin samples (<25nm). Nevertheless, in chapter 4 we showed that bacterial samples are much greater in size, being up to 1.5 orders of magnitude greater. In this chapter we address the capability of EFM to obtain local electrical images under liquid conditions of topographically tall samples. With the use of a conductive sample and a biocompatible dielectric sample we show that for topographically tall samples the EFM signal still remains local, being capable of detecting electrical response from the sample under study. A strong positive capacitance gradient contrast shows the presence of a conductive sample, while a weak negative contrast shows the hydration of the biocompatible gelatine under liquid conditions. These results show the potential of EFM under liquid to perform images of topographically tall samples without losing EFM locality, being a main goal of this work of thesis to further on apply it to bacterial samples under liquid conditions.

7.1 Introduction

As described in chapter 3, the electrical characterization under liquid conditions is limited due to its complexity. The transaction from air electrical measurements to liquid electrical measurements is not trivial and should be taken with precaution. On a general approximation, an inverse behaviour is expected when comparing air to liquid electrical measurements. In the case of electrical measurements performed in air, since the relative dielectric constant value of air is ~1, the sample which displaces the air will have a higher dielectric constant. This change will cause an increase on the electrical response between the probe and the conductive sample. On the other hand, the relative dielectric constant value of water is ~80. The vast majority of dielectric objects have a lower dielectric value, and hence the displacement of the water by a dielectric sample

would cause a decrease on the electrical response. In the case of an object with a higher dielectric value than water, then an increase in the electrical response should be encountered, being greatest for the case of metal samples. It is worth mentioning that in the case of a metal sample, the increase in the capacitance is not due to the increase on the dielectric value with respect to the base electrode (since both are metallic), but rather a decrease in the separation between the probe and metal surface.

With the use of the Electrostatic Force Microscope, members of the research group have obtained local electrical images of inorganic and biological samples [62]. The previous work accomplished by the research group was reserved to small thin samples (<25nm), in particular an inorganic structure and a supported lipid bilayer [63,64]. In order to demonstrate the local capabilities of the EFM under liquid conditions of topographically tall samples, we use two distinctive samples. As a first sample, a conductive protrusion on a conductive sample, consisting of gold on top of a gold substrate, is used. The second sample is composed of an irregular biocompatible gelatine layer which is deposited on top of a conductive sample. The gelatine layer acts as a dielectric material with similar dielectric attributes to those as biological organism, in contraposition to the use of an inorganic dielectric substrate.

7.2 Materials and Methods

Gold and gelatine sample preparation. For the conductive sample, a gold substrate (Arrandee) was used. The substrate was cleaned following a sequence of sonication in acetone, isopropanol and milli-Q water. A conductive protrusion on the gold substrate was attributed to a scratch performed on the gold substrate, which caused some gold to peel off from the substrate and deposit onto the adjacent gold substrate. The gelatine sample consisted on a layer of biocompatible gelatine (Sigma-Aldrich G6144) deposited on top of the gold substrate (Arrandee) as explained in chapter 4. For this case scenario, the sample was not left to stand straight to allow the gelatine to form irregular patterns on the gold substrate instead of a thin layer.

Atomic and Electrostatic Force Microscopy imaging. Topographic and capacitance gradient images have been obtained with a commercial AFM system (Nanotec Electronica, S.L.) following the electrostatic force microscopy two pass mode for liquid conditions detailed in chapter 3 and Ref. [62]. Briefly, during the first pass, the topographic line is obtained in conventional intermittent contact mode, followed by a second pass in which the probe moves at a constant height from the substrate. Before starting the second pass, the mechanical oscillation is interrupted and an electrical potential is applied (with the help of a switch), where an amplitude 2V rms and 44MHz frequency is modulated by an electrical potential of amplitude 0.8V rms and 2 kHz frequency. During the second pass, the electrically induced oscillation amplitude at the first excitation frequency ($A\omega$) is measured by an external lock-in amplifier (Anfatec instruments AG).

In chapter 5 we describe that lift-mode EFM allows to obtain maximum electrical contrast from the entire sample. Nevertheless, from the raw EFM images, the dielectric response cannot be inferred directly since some post-processing of the data is necessary. Since in liquid the veracity of the cross-talk removal has not been demonstrated, and is out of the scope of this thesis, images have been performed in constant height mode. In this mode, a change of capacitance gradient can be directly attributed to the sample, as previously shown [21,49]. The main drawback is that only information on the tallest part of the sample is obtained (see also chapter 5). To analyse and compare such images, the comparison between images is attained on the signal to noise levels.

Capacitance gradient approach curves have also been measured on given points of the sample. These curves are used to determine the constant height at which the EFM images are acquired by comparing the absolute value of the capacitance gradient in a bare part of the substrate of the EFM image with the values of the approach curve measured on this part of the sample, as previously used in chapter 5 and 6.

Solid platinum probes from Rocky Mountain Nanotechnology LLC, of spring constant ~0.3N/m and resonance frequency in solution of ~6kHz have been used all through this chapter. Imaging has been performed under milli-Q water at room temperature.

7.3 Results and Discussion

Figure 7.1a sows AFM topography images of the region on the gold substrate which has suffered from a scratch and its content has been deposited onto an adjacent region. The protruding gold presents an irregular pattern, with lateral dimensions (length and width) ~500nm and 420nm, respectively. In comparison to previous electrical results under liquid conditions, the protruding gold is half in size the existing electrical results obtained using this technique. Concerning the height, topographic cross-section profile reveals a 170nm protrusion from the gold substrate (Figure 7.1b), being almost one order of magnitude greater than that of the inorganic sample analysed previously by the members of the research group [62].

The EFM constant height image undertaken for the gold defect at a lift distance from the substrate of ~226 nm is shown in Figure 7.1c. This lift distance leaves a probe-gold defect separation of ~56 nm, which is greater than the sum of the Debye lengths and can be assumed that a change in capacitance gradient is not due to the overlapping of the EDL layers. Due to the almost spherical shape of the gold defect (Figure 7.1b), the major contrast obtained is at its highest point, showing a sharp positive contrast (Figure 7.1D). This positive contrast shows that the sample under study has a greater dielectric than water, and the EFM remains local for topographically tall samples, at least for conducting samples. This electrical results showed an improvement on the electrical lateral resolution achieved, obtaining electrical images of samples half in size to those previously obtained by the research group.

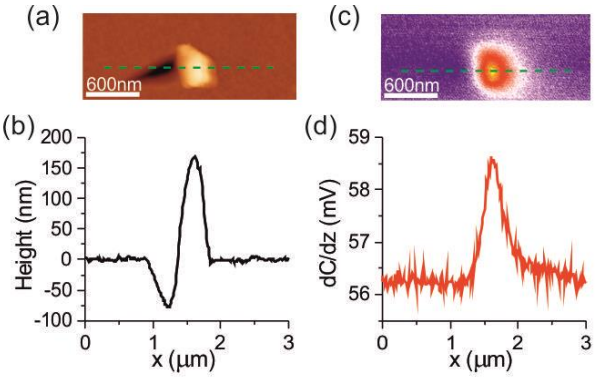

Figure 7.1 (a) Topographical image of the gold defect on top of the gold substrate. (b) The corresponding cross-section profile along the green line in (a). (c) EFM capacitance gradient image for the matching topographical image at a constant height of ~226 nm with respect to the metallic substrate. (d) Corresponding cross-section profile along the green line in (c).

The second sample considered consisted on a dielectric topographical tall sample. For this case, a layer of gelatine was deposited on top of the gold substrate. Gelatine was used instead of an inorganic sample because, since it is used for the attachment of the living bacterial samples, it was assessed to see if the gelatine coating could have a drastic effect on the EFM measurements of living bacterial cells. The gelatine coating of the gold was prepared similarly to chapter 4, with a slight modification to obtain irregular patterns (see Materials and Methods). The topographical AFM image (Figure 7.2a) reveals an irregular pattern, with a hill of gelatine deposited to the right of the image. Concerning the height, topographic cross-section profile reveals a ~105nm hill from the lowest point of the image (Figure 7.2b), being over one order of magnitude greater than the organic lipid bilayer sample analysed previously by the members of the research group [64].

EFM constant height image revealed a change in electrical response at a constant height of ~180nm, 75nm from the tallest point of the sample (Figure 7.2c). The irregular pattern of the gelatine makes the probe-gelatine distance modify, reason why the EFM image doesn't reflect a nice pattern as in Figure 7.1c. For the gelatine, the contrast is negative (Figure 7.2d), which is in correlation with the statement previously mentioned. The low signal to noise level can arise from the large probe-gelatine separation (~74nm) during imaging.

Figure 7.2e shows capacitance gradient approach curves measured on the metal and on the gelatine. In this case the gelatine has been shifted on the *Z* axis by the height of the gelatine. This type of graph allows to predict the resulting contrast of an EFM image at a given lift distance. For the height used (~180nm), the values obtained in the EFM image are well in agreement with the predicted from the curves (inset Figure 7.2e). This shows that at lower lift distances, a greater contrast would be obtained.

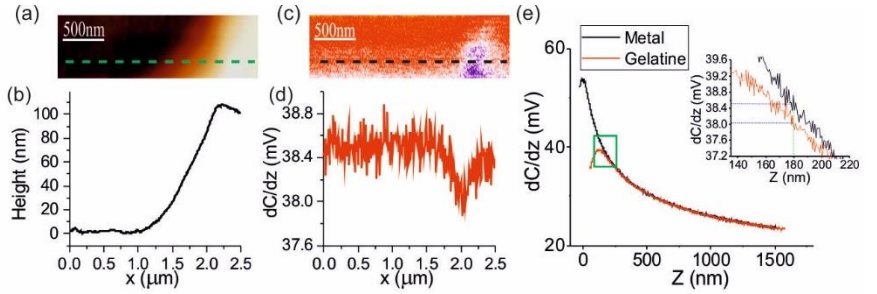

Figure 7.2 (a) Topographical image of an irregular gelatine coating on top of the gold substrate, presenting a hill of gelatine on the right side of the image. (b) Corresponding topographical cross-section profile along the green line in (a). (c) EFM capacitance gradient image for the matching topographical image at a constant height of ~180 nm with respect to the lowest region of the image. (d) Corresponding capacitance gradient cross-section profile along the black line in (c). (e) Superposition capacitance gradient approach curve performed on the metal substrate (black) and the gelatine (red), with the second shifted in the *Z* axis by the gelatine height. The inset shows a zoom of the most significant values, where at the given height, the expected value from the contrast matches the one obtained in the image. Lines are used as guidelines to help reader appreciate the difference.

Comparing the electrical response presented by the biocompatible gelatine to the previous results obtained by the research group (the inorganic sample and the lipid bilayer [63,64]), a much lower contrast is observed. While previous results have shown a contrast (signal to noise level) of ~4 for the 5nm lipid bilayer, and of ~10 for the 20nm inorganic structure, the gelatine was down to ~2.5. The possibility that what has been assumed to be gold substrate (left side of Figure 7.2a) could have a thin layer of gelatine would reduce the electrical signal. Nevertheless, the gelatine coating would reduce the absolute value of the

electrical signal, but a large contrast should still be present due to the substitution of ~105nm of water by the gelatine imaged.

From another point of view, the gelatine is a porous dielectric material which is capable of absorbing water content into its interior. This wettability of the gelatine would cause to increase the effective dielectric value of the gelatine, decreasing the difference in dielectric value between the liquid environment and the sample under study. This reduction is probably the cause of the low contrast obtained of the gelatine hill in Figure 7.2c. Nevertheless, the low contrast and the high signal to noise level observed by the gelatine (Figure 7.2e) rules out the possibility that the gelatine coating on a conducting substrate could hinder the electrical contrast of a sample deposited on top of the gelatine layer, such as the case of living bacteria cells.

7.4 Conclusions

In this chapter we have extended the capabilities of the Electrostatic Force Microscope to perform electrical images under liquid conditions. In particular we have shown that EFM under liquid conditions is capable of achieving images of samples half in lateral size, and over an order of magnitude in height. These results suggested that EFM is capable of detecting electrical response for topographical tall samples, since electrical locality at the probe apex is not lost. The low contrast exhibited by the gelatine sample indicates that the gelatine is hydrating, and as a consequence, would not hinder the electrical response present by a sample placed on top of a thin layer of gelatine. Present results show the potential of EFM to analyse topographically tall samples under liquid conditions, being of special interest for living bacterial cells under natural environments.

8 Internal hydration properties of single bacterial endospores probed by environmental electrostatic force microscopy

As described in chapter 1 and 2, the bacterial endospores have a complex structure, where its resistance to harsh conditions is attributed to the control of its water content. In chapter 5 and 6 we observe the capabilities of EFM to detect intrinsic signals which is also dependent upon the sub-surface properties of the sample. With this in mind, we show that the internal hydration properties of single *Bacillus cereus* endospores can be determined through the measurement of its electric permittivity in air under different relative humidity (RH) conditions by means of quantitative environmental electrostatic force microscopy (EFM). We show that an increase in the RH from 0% to 80% induces a large increase in the equivalent homogeneous relative electric permittivity of the bacterial endospores, from ~4 up to ~17, accompanied only by a small increase in the endospore height, of just a few nanometres. These results correlate the increase of the moisture content of the endospore with the corresponding increase of environmental RH. 3D finite element numerical calculations, which include the internal structure of the endospores, indicate that the moisture is mainly accumulated in the external layers of the endospore, hence preserving the core of the endospore at low hydration levels. This mechanism is different from what we observe for bacterial cells of the same species, in which the cell wall at high humid atmospheric conditions is not able to preserve the cytoplasmic region at low hydration levels. These results show the potential of quantitative environmental EFM to study the internal hydration properties of small scale biological (and non-biological) entities under variable air humidity conditions, opening novel avenues for nano-hygroscopic studies, which can be of relevance to understand essential biological processes and to design novel bio-nanotechnological applications. The capability to characterize the hygroscopic properties by EFM accomplish the main goal of this work of thesis, which can be further be used for the characterization of other biological samples.

This chapter reproduces almost literally the manuscript submitted: *Internal hydration properties of single bacterial endospores probed by environmental electrostatic force*

microscopy by M Van Der Hofstadt, R Fabregas, R Millan-Solsona, A Juarez, L Fumagalli and G Gomila. My contribution to this paper was to obtain all experimental results (from sample preparation to image acquisition), data analysis with R Millan-Solsona and supervisor, and manuscript writing and development in collaboration with my supervisor and rest of the authors. 3D modelling was performed by R Fabregas.

8.1 Introduction

As we have explained in chapter 1 and 2, the depletion of nutrients or the presence of harsh environmental conditions activates effective survival strategies on living organisms. One of the best known examples is the production of endospores by prokaryotes, such as the genus *Bacillus* or *Clostridium* [25]. Endospores consist of micrometric capsules produced by bacterial cells where replicated DNA is compacted into a core region and surrounded by protein and lipid membrane layers, of which the more relevant are (from inside to outside) the inner membrane, the cortex and the coat. Endospores can remain in a metabolically dormant state in dry conditions for decades and are capable of germinating back into a vegetative bacterial cell within minutes when appropriate environmental conditions are established (e.g. presence of water, nutrients, appropriate temperature, etc.). In addition to resist desiccation conditions, endospores are capable to resist other severe conditions, such as high temperatures (even combined with high hydrostatic pressures), radiations or toxic chemicals [22,34,146], making them a great threat in clinical medicine, food industry or terrorism.

The outstanding resistance of dormant endospores is believed to be strongly related to its capability to preserve the core at low hydration levels under atmospheric conditions [23,147–149]. At low hydration levels, important core enzymes remain inactive [34,148,150] and do not denature irreversibly upon a temperature increase [150,151]. In addition, the core is believed to be in high viscous state (glass or gel, still under discussion), which further reduces the diffusive molecular motions and further contributes to preserve the molecular structure of the proteins and the genome [152–154]. This peculiar internal hydration distribution seems to be, also, at the basis of the large forces and stresses generated by volume changes in endospores upon exposure to

environmental relativity humidity modifications [155–157]. This latter property has been used very recently to develop surprising technological applications, including energy-harvesting devices able to generate electrical power from an evaporating body of water [157,158] and electromechanical tunnelling graphene quantum dot-spore devices [159].

Therefore, understanding the internal hydration properties of endospores under a large range of varying environmental humidity conditions (internal hygroscopicity) is a subject of major interest both to understand the fundamental mechanisms of endospore resistance, as well as, to design novel technological applications.

In recent years a significant effort has been made to develop micro/nanotechniques able to examine the internal hydration properties of endospores at the single endospore level. These techniques allow providing direct answers to this problem not subject to the averaging associated to traditional population endospore studies [7,160–163]. The single endospore techniques used for hygroscopic studies include high resolution secondary ion spectroscopy (NanoSIMMS) [11], confocal Raman Microspectroscopy [164], fluorescence redistribution after photobleaching microscopy (FRAP) [23,165], automated scanning optical microscopy [155] and microsystem techniques, such as single particle levitation [166] and suspended microchannel resonators [167]. In spite of the valuable results obtained by the above mentioned techniques, they still suffer from some inherent limitations, namely, to be able to work under different environmental humidity conditions on a given endospore in a non-destructive way, with high spatial resolution (nanoscale) and with sensitivity to the internal hydration distribution. We note that other nanotechniques, such as Atomic Force Microscopy (AFM) or tip-enhanced Raman scattering (TERS), have been applied to endospore research, but not to the specific problem of determining the endospore hydration properties [14,33,35,168].

Here, we overcome some of the limitations of the above mentioned techniques by addressing the problem of measuring the internal hydration properties of single bacterial endospores by using quantitative Electrostatic Force Microscopy (EFM) under environmental relative humidity control. As described in chapter 5, EFM is a scanning probe microscopy technique sensitive to the local dielectric properties of the samples. Examples showing this ability include numerous applications to samples of non-biological origin (thin and thick oxides [46],

polymer films [105,106,108], nanowires [124], nanotubes [107,123] or nanoparticles [49,119–121]), and of biological origin (single bacterial cells [21,169], single virus particles [49], solid supported biomembranes [126], protein complexes [125] or DNA molecules [122]). EFM has two important properties relevant for the present application, namely, (i) it is sensitive to the internal dielectric properties of the samples, since it is based in the measurement of long range electric forces (chapter 6) [142–144] and, (ii) it is also sensitive to the presence of moisture in the sample [21], due to the large water electric permittivity ($\varepsilon_{r,water}$~80). The above mentioned features of quantitative environmental EFM show that this technique is optimal to probe *in situ* and in a non-destructive way the internal hydration properties of small scale biological samples, and bacterial endospores in particular, under varying environmental humidity conditions.

In order to achieve this goal we built an environmental EFM system able to cover a broad range of RH levels (from 0% to 80%). In addition, we developed a new data analysis methodology to quantitatively compare the results under such different environmental humidity conditions. Finally, we implemented accurate 3D simulation methods to quantify the EFM measurements and to determine the internal electric permittivity properties of the endospore, and from there, assess the internal hydration properties of a single bacterial endospore.

8.2 Results and Discussion

Figure 8.1 shows AFM topographic and EFM capacitance gradient images of an individual endospore from *B. cereus* under three different environmental humidity conditions corresponding to relative humidity RH~0% (first column), 40% (second column) and 80% (third column) (see Materials and Methods and Appendix 8.5 for experimental details). The topographic AFM images (Figures 8.1a, 8.1b and 8.1c) reveal a bacil-like shape for the mature endospore with lateral dimensions (length, width) ~2020nm and ~980nm, respectively, obtained after tip deconvolution analysis (see Appendix). Concerning the height, we observe a systematic and small increase with RH levels, giving values of ~825 nm, ~842 nm and ~858 nm corresponding to RH values of ~0%, 40% and 80%,

respectively (see topographic cross-section profiles in Figure 8.1d). Similar size variations have been also reported by other authors by using different methods [155].

Figures 8.1e, 8.1f and 8.1g show lift mode capacitance gradient EFM images of the bacterial endospore obtained with the same tip at an approximately similar lift distances, z_{lift}=53 nm, 56 nm and 57 nm, respectively. The images show a decrease of the capacitance gradient as the tip moves from the substrate to the top of the endospore, being the decrease smaller the higher the relative humidity (see cross-section profiles in Figure 8.1h). This behaviour is systematically reproduced at different lift distances, as shown in Figure 1n where we plot the absolute values of the lift capacitance gradient on the centre of the endospore (circles) and on the substrate (squares), as a function of lift distance (see also Appendix 8.5). We note that the change of environmental RH produces basically a variation of the capacitance gradient on the endospore, and not on the substrate. To rule out that this variation on top of the endospore at the different environmental RH is due to a topographic crosstalk effect associated to the small increase in the endospore height, we determined the intrinsic capacitance gradient images [169], in which topographic crosstalk contributions are removed. To obtain these images we use the topographic images and an approach curve measured on a bare part of the substrate (Figure 8.1m, black line), as explained in chapter 5 [169]. The resulting intrinsic capacitance gradient images are shown in Figures 8.1i, 8.1j and 8.1k. It can be clearly seen that the intrinsic images also show a variation in its contrast on the endospore for varying environmental RH (see cross-section profiles in Figures 8.1l and the values for different lift distances on the center of the endospore and on the substrate in Figure 8.1o).

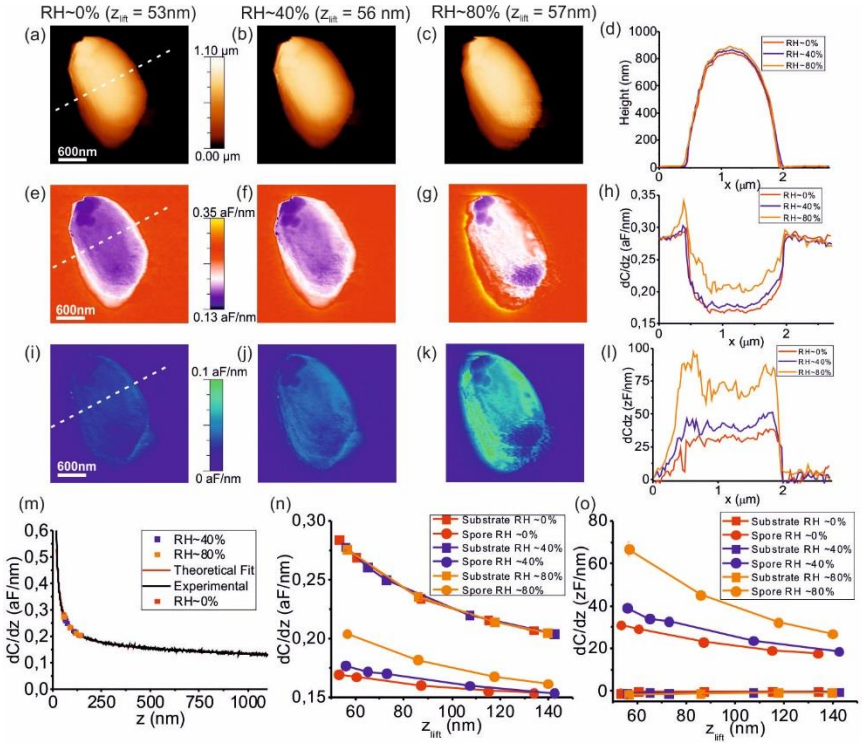

Figure 8.1. (a) Topographic, (e) lift capacitance gradient and (f) intrinsic capacitance gradient images of a *B. cereus* endospore obtained under dry conditions (RH~0%) at a lift distance z_{lift}=53 nm. (b), (f) and (j) idem at RH~40% and lift distance z_{lift}=56 nm. (c), (g) and (k) idem at RH~80% and lift distance z_{lift}=57 nm. (d), (h) and (j) show the corresponding cross-section profiles along the line drawn on the top figures. (m) Capacitance gradient approach curve on the bare substrate (black line). Symbols represent the values extracted from the EFM lift images on the substrate and used to determine the lift distances (red RH~0%, blue RH~40% and orange RH~80%). The red line (almost indistinguishable) is a theoretical fit to the experimental data used to calibrate the tip geometry, giving in this case R=133±2 nm θ=20±1º and k_{stray}=0.066±0.002 aF/nm. (n) Lift capacitance gradient values as a function of the lift distances obtained from the lift images on the bare substrate (squares) and on the centre of the endospore (circles). (o) Idem for the intrinsic capacitance gradient images. The error in the data represented by the symbols is of the order of 0.002 aF/nm, being smaller than the symbol size.

Altogether, these results imply that the variation in the lift EFM capacitance gradient images observed at increasing environmental humidity conditions is directly related to a variation in the electric permittivity properties of the endospore, and not to a change in the endospore dimensions. The variation in the electric permittivity, in turn, can be unambiguously correlated to an increase of the moisture content of the endospore, thus confirming the ability of EFM to assess the hygroscopic properties of small scale biological samples. Note that EFM measurements are more sensitive to the hygroscopic properties than the AFM images themselves, as it can be seen by comparing the relative variations produced by a RH change on the electric signals (Figure 8.1l) and on the topographic profiles (Figure 8.1d). The reason being that the electric permittivity of water ($\varepsilon_{r,water}$~80) is much larger than that of the dry biochemical components of the endospore ($\varepsilon_{r,proteins}$~3-5 for proteins [125,126], $\varepsilon_{r,lipids}$~2 for lipids [126] and $\varepsilon_{r,DNA}$~8 for DNA [49,125]), what makes its presence easily detectable in the EFM images even when small amounts of moisture are present.

As a control, a similar analysis has been performed using a *B. cereus* vegetative cell instead of the endospore. Results are shown in Figure 8.2. The lateral dimensions of the vegetative cell obtained from the topographic images (Figures 8.2a, 8.2b and 8.2c) are l~3450nm and w~960 nm, while the heights are h~622nm, 643nm and 670 nm for RH ~0%, 40% and 80%, respectively (see also topographic cross-section profiles in Figure 8.2d). The dielectric response of the vegetative bacterial cell to environmental RH changes is qualitatively very similar to the one found for the endospore. This fact is shown in the capacitance gradient lift EFM images in Figures 8.2e, 8.2f and 8.2g obtained at approximately the same lift distance, z_{lift}=85 nm – 90 nm (see also the capacitance gradient cross-section profiles in Figure 8.2h and the values on the centre of the endospore for different lift distances in Figure 8.2n and in the Appendix 8.5).

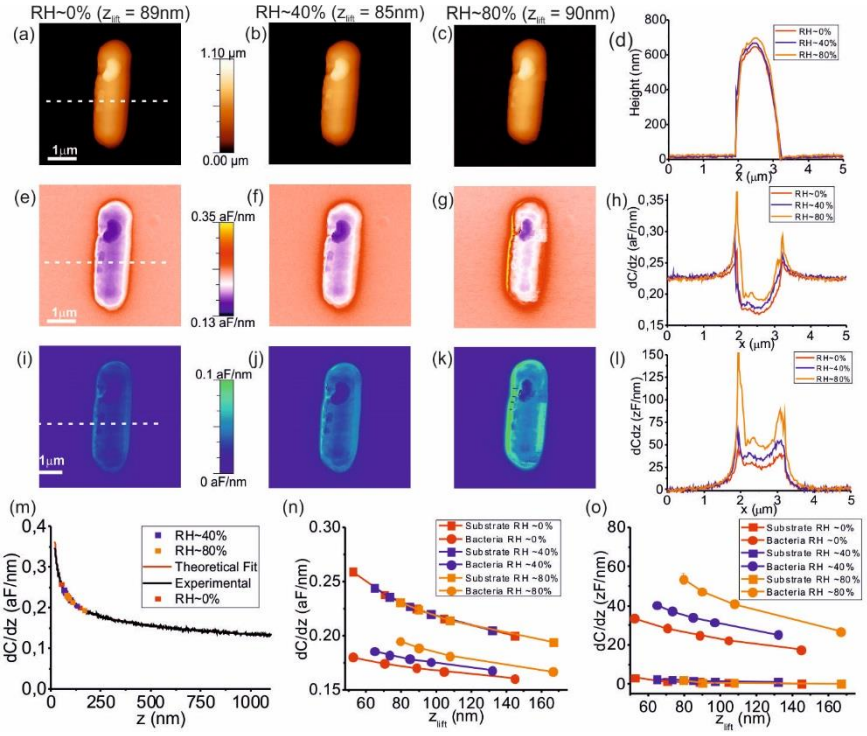

Figure 8.2 (a) Topographic, (e) lift capacitance gradient and (i) intrinsic capacitance gradient images of a *B. cereus* vegetative cell obtained under dry conditions (RH~0%) at a lift distance z_{lift}=89 nm. (b), (f) and (j) idem at RH~40% and lift distance z_{lift}=85 nm. (c), (g) and (k) idem at RH~80% and lift distance z_{lift}=90 nm. (d), (h) and (l) show the corresponding cross-section profiles along the line drawn on the top figures. (m) Capacitance gradient approach curve on the bare substrate (black lines). Symbols represent the values extracted from the images and used to determine the lift distances (red RH~0%, blue RH~40% and orange RH~80%). The red line (almost indistinguishable) is a theoretical fit to the experimental data used to calibrate the tip geometry, giving in this case R=63±2 nm θ=27±1º, and k_{stray}=0.040±0.002 aF/nm. (n) Lift capacitance gradient values as a function of the lift distance obtained from the lift images on the bare substrate (squares) and on the center of the vegetative cell (circles). (o) Idem from the intrinsic capacitance gradient images. The error in the data represented by the symbols is of the order of 0.002 aF/nm, being smaller than the symbol size.

The intrinsic capacitance gradient images in Figures 8.2i, 8.2j and 8.2k, together with the cross-section profiles in Figure 8.2l and the values on the centre of the vegetative *B. cereus* cell as a function of lift distance in Figure 8.2o, show again that the variation in the dielectric response for varying environmental RH levels cannot be attributed to a change in the dimensions of the bacterial cell, but to a change in its electric permittivity properties. Therefore, we conclude that, as observed for the endospores, *B. cereus* vegetative bacterial cells also absorb moisture from the environment, showing a direct correlation between the RH level and the dielectric response.

We addressed next the question whether the overall hydration properties, as well as the internal water distribution, of endospores and vegetative cells is the same or whether they offer distinct properties. To this end, we address the problematics of determining the equivalent homogeneous electric permittivity values of both bacterial entities, as well as their surface and internal electric permittivities.

To address this problem we consider the core-shell model shown schematically in Figure 8.3a. This model mimics in a simplified manner the internal structures of the endospore, as it can be inferred from the TEM image shown in Figure 8.3b. In the model the core represents the core of the endospore, while the shell represents the outer shells of the endospore, which includes the inner membrane, the cortex and the coat. For the vegetative cell we also use the same type of geometric model. However, in this case the core represents the cytoplasmatic region and the shell the cell wall, which includes the inner membrane and the thick peptidoglycan layer characteristic of Gram-positive bacterial cells (see Appendix 8.5.4). We assume in the model (i) different electric permittivities for the shell, $\varepsilon_{r,shell}$, and core, $\varepsilon_{r,core}$, regions, and (ii) an ellipsoidal shape for the endospore (3D simulations required). The model takes into account the actual sample and tip dimensions, which are obtained, respectively, from a tip deconvolution analysis of the topographic images (see Appendix 8.5) and from a tip calibration procedure based on a capacitance gradient approach curve measured on the bare substrate (see Figures 8.1m and 8.2m for the corresponding calibration curves for endospore and bacterial cell measurements, respectively, and the Materials and Methods section). An example of the electric potential distribution of the modeled system is shown in Figure 8.3c.

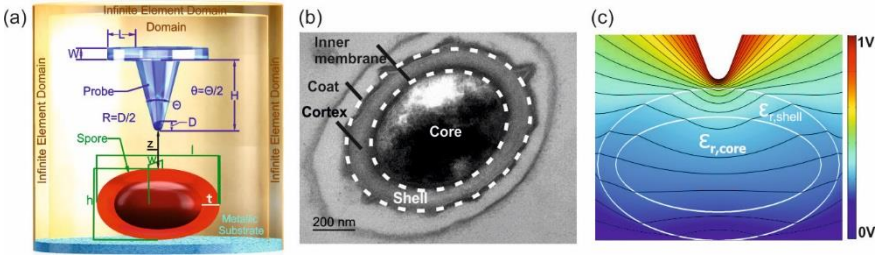

Figure 8.3 (a) Schematic representation of the tip-endospore model used in the finite element numerical calculations, with the model parameters indicated. (b) Transmission Electron Microscopy image of a cross-section cut of an endospore, with its main parts indicated. The dashed lines represent the division of the endospore in the core-shell model. (c) Example of the electric potential distribution for a tip-endospore system configuration. Parameters of the simulation: h=800 nm, l=2000 nm, w=1000 nm, $\varepsilon_{r,core}$=8 and $\varepsilon_{r,shell}$=4, R=100 nm, θ=30º, H=12.5 μm, W= 3 μm, L=0 μm and z=50 nm.

To determine the equivalent homogeneous electric permittivity of the endospore and of the bacterial cell, $\varepsilon_{r,eff}$, we consider the model with $\varepsilon_{r,core}$= $\varepsilon_{r,shell}$= $\varepsilon_{r,eff}$. Figure 8.4a (res. 8.4b) shows the results (lines) of the calculated capacitance gradient values on the centre of the endospore (res. vegetative cell), as a function of the lift distance, for the values of the equivalent homogeneous electric permittivity that best fit the experimental data (circles). The continuous lines represent the best fit curves, while the dashed lines represent curves at plus and minus one standard deviation of the fit. Red, blue and orange colours represents measurements at RH 0%, 40% and 80%, respectively. We also show on the plots the capacitance gradient values calculated for the tip on the bare metallic substrate (black line) and the experimental values measured there (squares). From this analysis, we obtain for the endospore equivalent homogeneous relative electric permittivities: $\varepsilon_{r,eff,endospore}$=4.3±0.3, 5.8±0.5 and 17±4, for RH=0%, 40% and 80%, respectively. For the vegetative cell, instead, we obtain: $\varepsilon_{r,eff,bact}$=5.0±0.5, 9.5±1 and 70±30, respectively (see Figure 8.4c).

The extracted equivalent homogeneous electric permittivities reveal that the global electric permittivity properties of the endospore and of the vegetative cell follow a relatively similar trend, namely, they show a relative small variation

from RH 0% to 40% followed by a large variation from RH 40% to 80%. We observe, in addition, that the vegetative cell shows a higher relative variation of its permittivity as compared to the endospore. These results indicate that both the endospore and the vegetative cell hydrate significantly starting at around 40% RH levels, and that the latter shows a more hygroscopic behaviour than the former. This latter observation supports previous statements made in the literature on this aspect based on population studies [7,162], here demonstrated at the single endospore and vegetative cell levels.

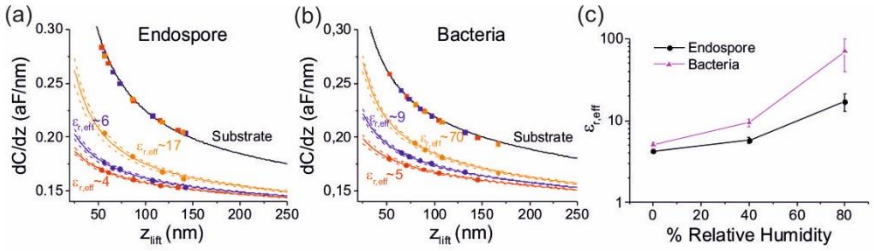

Figure 8.4 (a) (lines) Theoretical capacitance gradient as a function of lift distance for a probe located on the centre of the endospore for different values of the effective relative electric permittivity of the endospore (red 0% RH, blue 40% RH and orange 80% RH lines). The black line shows the corresponding curve on the metal substrate. The continuous line represents the theoretical curve that best fits the experimental data, while the dashed line represent plus minus a standard deviation. The symbols represent the experimental values obtained from the lift capacitance gradient images (same as in Figure 8.1n). The extracted equivalent homogeneous permittivities are $\varepsilon_{r,eff,endospore}$=4.3±0.3, 5.8±0.5 and 17±4, for RH=0%, 40% and 80%, respectively. Tip parameters: R=133 nm, θ=20º and k_{stray}=0.066 aF/nm, obtained from the calibration curve in Figure 1m. Endospore dimensions: l=2020 nm and w=980 nm (obtained from a tip deconvolution analysis) and h=825 nm, 842 nm and 858 nm for RH=0%, 40% and 80%, respectively (obtained from topographic profiles). (b) Idem for the bacterial cell measurements giving $\varepsilon_{r,eff,bact}$=5.0±0.5, 9.5±1 and 70±30, for RH=0%, 40% and 80%, respectively. Tip parameters: R=63 nm, θ=27º and k_{stray}=0.040 aF/nm (obtained from the calibration curve in Figure 8.2m). Bacterial cell dimensions: l=3450 nm and w=960 nm (obtained from a tip deconvolution analysis) and h=622 nm, 643 nm and 670 nm for RH=0%, 40% and 80%, respectively (obtained from topographic

profiles). (c) Plot of the extracted effective equivalent homogeneous relative electric permittivity as a function of the % Relative Humidity, for a bacterial endospore (black symbols) and a vegetative cell (pink). The line is a guide to the eyes.

Based on these results, we now analyse how the electric permittivity values of the internal parts of the endospore (and bacterial cell) evolve with the environmental humidity. To this end we consider the theoretical model with different electric permittivities for the core, $\varepsilon_{r,core}$, and the shell, $\varepsilon_{r,shell}$, and determine those values compatible with the measured equivalent homogeneous electric permittivity, $\varepsilon_{r,eff,exp}$, i.e. those values solving the relation $\varepsilon_{r,eff}(\varepsilon_{r,shell},\varepsilon_{r,core})= \varepsilon_{r,eff,exp}$ (see the Materials and Method section and Refs.[21,49] for further details). In the calculations, the thickness values of the shell are obtained from the TEM images in Figure 8.3b and in the Appendix 8.5.4, giving t~160±20 nm for the endospore and t~60±10 nm for the bacterial cell. Moreover, we use lateral dimensions characteristic of the values obtained from the AFM images: h_{sp}=800 nm, l_{sp}=2 μm and w_{sp}=950 nm for the endospore, and h_{bac}=600 nm, l_{bac}=3.5 μm and w_{bac}=950 nm for the bacterial cell. For the tip geometry we use R=100 nm and θ=30º, and a lift distance z_{lift}=50 nm, in both cases, since the results are almost insensitive to these parameters [21].

Figures 8.5a (res. 8.5b) shows the couples of values ($\varepsilon_{r,core}$, $\varepsilon_{r,shell}$) which are compatible with the measured equivalent homogeneous electric permittivity, $\varepsilon_{r,eff,exp}$, for the endospore (res. bacterial cell), for the different environmental humidity conditions considered (red RH~0%, blue 40%, and orange 80%). From the curves represented in Figures 8.5a and 8.5b we can investigate the evolution of the electric permittivities of the core and shell regions as a function of RH. We start by assuming that the electric permittivity of the shells of the endospore and of the bacterial cell at 0% RH is $\varepsilon_{r,shell,RH0}$~3–4, a range of values compatible with that of dry proteins and lipids, which are their main components [49,125,126]. By assuming these range of values, the plot predicts a core permittivity at 0% RH of $\varepsilon_{r,core,RH0}$~4–8 for the endospore, and of $\varepsilon_{r,core,RH0}$~6–7 for the bacterial cells. Both values are slightly larger than that of proteins and lipids, but are compatible with the presence of also DNA in the core and cytoplasmic region (note that DNA has a larger electric permittivity $\varepsilon_{r,DNA}$~8) [125].

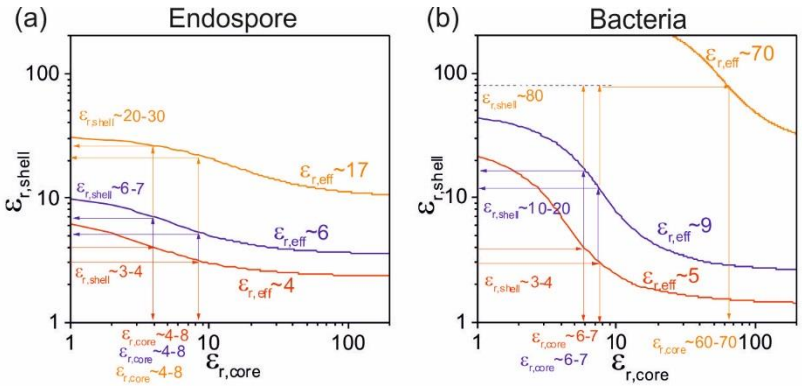

Figure 8.5 (a) and (b) Curves of values ($\varepsilon_{r,core}$, $\varepsilon_{r,shell}$) compatible with the measured equivalent homogeneous electric permittivity of the endospore and the vegetative cell, respectively, under different environmental humidity conditions (red RH~0%, blue 40% and orange 80%). Geometrical parameters used in the calculations: h_{sp}=800 nm, l_{sp}=2 μm and w_{sp}=950 nm for the endospore; and h_{bac}=600 nm, l_{bac}=3.5 μm and w_{bac}=950 nm for the bacterial cell. For the tip geometry we used R=100 nm and θ=30º, and a lift distance z_{lift}=50. The thin arrow lines help in determining the core and shell values in each case.

When the RH is increased to 40%, the results shown in Figures 8.5a and 8.5b are both compatible with keeping the core at the same hydration level than at 0% RH and increasing the shell permittivity to $\varepsilon_{r,shell,RH40}$~6–7 for the endospore and to $\varepsilon_{r,shell,RH40}$~10–20 for the bacterial cell. This would mean that the outer shells of both the endospore and the vegetative cell are able to accommodate the moisture adsorbed at low RH levels. In the case of the endospore, it produces only a slight hydration of the shell, while on the vegetative cell it is already relatively large at these RH levels. When considering a RH value of 80%, we obtain that the shell of the endospore is still able to accommodate the moisture and leave the core non-hydrated. In this case, the hydration level of the shell is already relatively large, giving an electric permittivity of $\varepsilon_{r,shell,RH80}$=20–30. Instead, for the vegetative cell, at RH ~80%, the moisture can no longer be accommodated by the shell region, as it would imply an unphysically large value of its permittivity, $\varepsilon_{r,shell,RH40,bac} > \varepsilon_{r,water}$~80. A solution in this case is that part of the moisture penetrates to the core region (the cytoplasmic region). If we assume for instance the limit case of $\varepsilon_{r,shell,RH80,bac}$~80 then one would have

$\varepsilon_{r,core,RH80,bac}$~60–70, also indicating a large hydration level of the cytoplasmic region.

The previous results support the statement that endospores have an innate mechanism to avoid hydration of the core even at large environmental relative humidity levels. This mechanism enables the core remaining almost dry, and hence, enables the endospore to extend dormancy under atmospheric conditions [23,34,147,148,150,151].

The mechanism by which the core is kept at low levels of hydration is still the subject of debate. The current view assumes that the main role is played by the inner membrane, which, in dormant endospores, is largely immobile and greatly reduces water permeation [150,165], thus preserving the core from being hydrated. On the other hand, the subsequent layer, the cortex, is believed to be hydratable [170] and can accommodate a large proportion of the water content of the endospore when the endospore is fully hydrated (note that the external layer, the coat, is permeable to water [155] and, when the endospore is hydrated, tends to show lower water content than the cortex [150,163]).

The present approach based on quantitative environmental EFM provides some fundamental advantages to study the internal hydration properties of single bacterial endospores with respect to other existing micro/nanotechniques used to date [7,160–163]. First, it is non-destructive and thus it allows varying in situ the environmental humidity conditions on a given endospore. Second, being the electric forces long ranged, it allows accessing the internal dielectric properties of the endospore, and hence, proposing models of internal hydration by making use of the known internal structure of the endospores. And finally, it provides also *in situ* access to eventual variations of the physical dimensions of the endospore with nanoscale spatial resolution, thus avoiding ambiguous interpretation of the results.

We note that the present methodology can be applied to other numerous problems where the internal hydration properties of small scale objects is of major interest. Examples could include the study of the hydration properties of biological entities, such as fungi endospores and single virus particles, and of humidity dependent biological process such as the production of mycotoxins, one of the largest food poisoning threats [171]. Similarly, it could be applied to the study of the nanoscale hygroscopic properties of novel water responsive

materials for energy harvesting [172,173] or of aerosol nanoparticles of interest in atmospheric sciences [174].

8.3 Conclusion

We have demonstrated that quantitative environmental Electrostatic Force Microscopy can be applied to the important problem of determining the internal hydration properties of single bacterial endospores. In particular, we have demonstrated that individual endospores of *Bacillus cereus* show a small variation of its equivalent homogeneous electric permittivity from 0% to 40%, followed by a large variation from 40% to 80%. These results suggested that bacterial endospores hardly hydrate at low RH's but, that they become significantly hydrated at larger RH. The analysis of these results by means of a core-shell model, which includes the internal structure of the bacterial endospores, has demonstrated that the external layers of the bacterial endospores (inner membrane, cortex and coat) can accommodate most of the moisture adsorbed by the endospore, even at the high relative humidity levels analyzed here (up to 80% RH), and leave the core of the endospore at low hydration levels. On the contrary, on bacterial cells, the cell wall is not able to accommodate all the moisture at high hydration levels and the cytoplasmic region becomes highly hydrated. This differential behavior is key to enable endospores to remain viable in its dormant state under atmospheric conditions, and could be at the basis of the large water responsive properties of bacterial endospores. Present results show the potential of quantitative environmental EFM to analyze the hygroscopic and internal hydration properties of small scale objects, with important implications in both Life and Material sciences.

8.4 Materials and Methods

Endospore and bacterial cell growth and sample preparation. *Bacillus cereus* (CECT495) was used in this study. Cells were grown as previously described [33]. Endospores were obtained by growing cells in G medium for 48h. This culture time guranteed that complete mature bacterial endospores are formed. Non sporulanting vegetative bacterial cells were cultured in Trypticase soy broth (Scharlau) for 24h at 30ºC and 250 rpm. For AFM and EFM imaging, the samples were deposited on a gold substrate (Arrandee), previously cleaned following sequential sonication washing with acetone, isopropanol and water. Samples were allowed to dry in a cabin flow before imaging.

Atomic and Electrostatic Force Microscopy imaging. Topographic and capacitance gradient images have been obtained with a commercial AFM system (Nanotec Electronica, S.L.) following the electrostatic force microscopy two pass mode detailed elsewhere [169]. Briefly, during the first pass the topographic line is obtained in conventional intermittent contact mode, followed by a second pass, in which the tip moves at a constant height from the measured sample topography, z_{lift} (lift-mode), while an electric potential of amplitude 3V rms and 2 kHz frequency is applied. In the second pass, the electrically induced oscillation amplitude at double of the excitation frequency ($A_{2\omega}$) is measured by an external lock-in amplifier (Anfatec Instruments AG). Conversion of the oscillation amplitude (rms value in volts) into the capacitance gradient is done by means of the relationship

$$\frac{dC}{dz} = \frac{2\sqrt{2}}{v_{rms}^{\ 2}} k \frac{\left(A_{2\omega} - A_{2\omega,offset}\right)}{mG} \tag{8.1}$$

where k is the equivalent spring constant of the cantilever, v_{rms} the rms voltage amplitude, $A_{2\omega,offset}$, the lock-in offset, m the optical lever sensitivity and G the lock-in gain. Typical values of these parameters are m~3 mV/nm, $A_{2\omega,offset}$~15 mV, G~500, v_{rms}~3V, k~0.5 N/m and $A_{2\omega}$~0–4 V. The absolute capacitance gradients values are then in the range ~0–0.4 aF/nm, with a sensitivity down to ~0.002 aF/nm. Capacitance gradient approach curves have also been measured on given points of the sample. These curves are used to determine the lift distances at which the EFM images are acquired by comparing the absolute value of the capacitance gradient in a bare part of the substrate of the EFM image with the values of the approach curve measured on this part of the sample. To help in the interpretation of the results, intrinsic capacitance gradient images (in which

topographic crosstalk contributions have been removed) have also been constructed following the methodology recently developed in chapter 5 [169]. A custom-made software written in Matlab (Mathworks Inc.) was developed to automatize these processes.

CDT-CONTR doped diamond probes (Nanosensors) of spring constant ~0.5 N/m and nominal tip radius ~100 nm have been used all through this chapter. Imaging has been performed under nitrogen ambient flow (~0% Relative Humidity), and under RH~40% and ~80% with the help of a homemade environmental EFM system. In this system, the ambient RH humidity of the AFM glass enclosure is regulated by a pump and monitored with a humidity sensor (Rotronic AG). Times >15 min where allowed after each change of humidity for system stabilization.

To monitor eventual changes on the photodiode sensitivity or tip geometry, after each set of EFM measurements at a given RH condition, a set of N=5 EFM approach curves were measured and analyzed following the specific methodology detailed in the Appendix 8.5.

3D finite element numerical calculations and internal electric permittivity quantification. The internal electric permittivity properties of the endospores and bacterial cells have been determined with the help of 3D finite element numerical calculations. To this end we used the model system schematically shown in Figure 8.3a. The endospore and the vegetative cell are assumed to have an ellipsoid shape (3D simulations required), and its internal structure is represented, in a simplified way, by a core and a shell, which are assumed to have different electric permittitvities, $\varepsilon_{r,core}$ and $\varepsilon_{r,shell}$, respectively. The width, w, height, h and length l of the endospore are obtained from the topographic AFM images after a tip deconvolution analysis similar to that of Ref. [45], but including also the cone contact region. In the present case, the cone contact region is relevant due to the large height of the bacterial endospores in relation to the tip radii of the probes (see Appendix 8.5.2). The thickness, t, of the shell is determined from the TEM images, as detailed below. The apex radius, R, and cone half angle, θ, are obtained from a least square fitting of the theoretical model to a capacitance gradient approach curve recorded on the substrate, as explained elsewhere [49] (other parameters are set to nominal values, cone height H =12.5 μm and cantilever thickness W =3 μm and cantilever "length" L=0 μm). The microscopic cantilever effects are included in a constant stray offset, k_{stray}.

The capacitance gradient between the probe and sample is calculated by solving Poisson's equation with the finite element software Comsol Multiphysics 5.2 (AC/DC electrostatic module). Poisson's equation solution results in the distribution of the static electric potential around the tip and in the sample (an example is shown in Figure 8.3c), from which we derive the Maxwell stress tensor on the probe surface, and, by integration of it on the surface of the probe, we obtain the electrostatic force [169]. Software routines written in Matlab (Mathworks Inc.) have been used to move the tip in the simulations with respect to the sample and to calculate the capacitance gradient at different lift distances, z_{lift}.

To determine the internal electric permittivities of the core and shell, we proceed in a two-step process. In the first step, we determined the equivalent homogeneous electric permittivity, $\varepsilon_{r,eff}$, of the endospore (and bacterial cell), by following a procedure similar to the one detailed elsewhere [21,49,169], but applied, here, to the case of lift EFM images. In a nutshell, we compare the experimental capacitance gradient values on the center of the endospore (and vegetative cell) obtained from the lift EFM images with the corresponding values obtained from the 3D numerical calculations, by setting $\varepsilon_{r,core}=\varepsilon_{r,shell}=\varepsilon_{r,eff}$, with $\varepsilon_{r,eff}$ being the single fitting parameter. In a second step, by means of 3D finite element numerical calculations, we determine the relationship between the equivalent homogeneous electric permittivity and the core and shell permittivities, $\varepsilon_{r,eff}=\varepsilon_{r,eff}(\varepsilon_{r,shell},\varepsilon_{r,core})$, and from this relationship, we determine the couples of values ($\varepsilon_{r,core}$, $\varepsilon_{r,shell}$) which are compatible with a given experimental value of $\varepsilon_{r,eff,exp}$, i.e., those values solving the relationship $\varepsilon_{r,eff}(\varepsilon_{r,shell},\varepsilon_{r,core})=\varepsilon_{r,eff,exp}$ [21,49].

Transmission Electron Microscopy imaging. Mature bacterial endospores and bacterial cells were directly fixed with 2.5% glutaraldehyde and post fixated with 2% osmium tetroxide. Samples were allowed to dehydrate in a graded acetone series. Samples were embedded into an epoxy resin and allow polymerization before performing thin sections (thickness~90 nm) with an ultramicrotome (ULTRACUT E). Observations of the sections were performed with a JEOL 1010 transmission electron microscope with a tungsten filament operating at 80kV. Digital images were captured with a GATAN ORIUS CCD camera.

8.5 Appendix

8.5.1 Monitoring photodiode sensitivity and tip geometry variations for measurements at different environmental relative humidity levels

In order to minimize errors in the quantitative comparison of EFM measurements taken under different environmental relative humidity conditions, we had to cope with two eventual sources of uncertainty, namely, changes in the photodiode sensitivity due to re-alignments of the laser spot position when changing the RH level, and changes in the tip geometry due to the large number of measurements performed with a given probe. We have monitored these changes by measuring EFM and deflection-distance D-z approach curves after each set of images taken at a given environmental RH condition.

The photodiode sensitivity, *m*, is usually obtained from the slope of the contact region of the D-z curves. However, in the present case, this method introduced an uncertainty of the order of 5-10% in this parameter, which was too high for the high precision of the EFM measurements. To cope with this problem, we monitored the eventual variation in photodiode sensitivity by comparing the long range values of the EFM curves. These values are basically depending on the interaction of the cantilever with the substrate, and should remain constant from measurement to measurement if the photodiode response is not varied. Instead, if the photodiode response is varied, one should observe that the curves scale among them by a multiplicative factor, *f*, corresponding to the ratio of change of the photodiode sensitivity. Therefore, to monitor eventual variations in photodiode sensitivity we proceeded as follows: (i) we aligned the raw 2ω oscillation amplitude EFM approach curves, $A_{2\omega}(Z)$, by using the jump to contact point observed in these same curves, and (ii) we analysed the long range part of the curves and determined whether any variation among them occurred. If this was the case, we attributed it to a change in the photodiode sensitivity, *m*, and determined the correction multiplicative factor, *f*. The new photodiode sensitivity would then be $m^*=m/f$. This latter photodiode sensitivity is the one used to calibrate the corresponding set of EFM images associated to the analysed EFM

approach curves. Concerning the monitoring of the variation of the tip geometry, we analysed the short range part of the raw EFM curves, once aligned and corrected for the photodiode sensitivity variation. If the curves overlapped in the short range also, this implied that the tip geometry had not changed during the measurement. We have only considered sets of measurements in which the tip geometry has not changed from the beginning to the end. We illustrate the procedure described above in Figure 8.6, for the approach curves related to the endospore measurements shown in Figure 8.1, and in Figures 8.7 for those related to the bacterial cell measurements shown in Figure 8.2.

To further test this procedure, in Figure 8.8 we show a similar analysis performed on a set of five consecutive EFM approach curves performed under the same environmental RH conditions (RH~0%). In this case, it can be seen that by just aligning the curves (Figure 8.8b), the curves nicely overlap in the long range region (Figures 8.8c), meaning no photodiode sensitivity change occurred (factor f=1), as it should be since no photodiode re-alignment took place. Moreover, they also align in the short range region (Figure 8.8d) meaning that no change in the tip geometry occurred. In this case, we also show the steps followed to convert one of the 2ω amplitude raw curve (in V) as a function of piezo displacement (Figure 8.8e) into the capacitance gradient curve (in aF/nm) as a function of tip sample distance (Figure 8.8f) by using Eq. (8.1) and the displacement approach curve (also shown in Figure 8.8e).

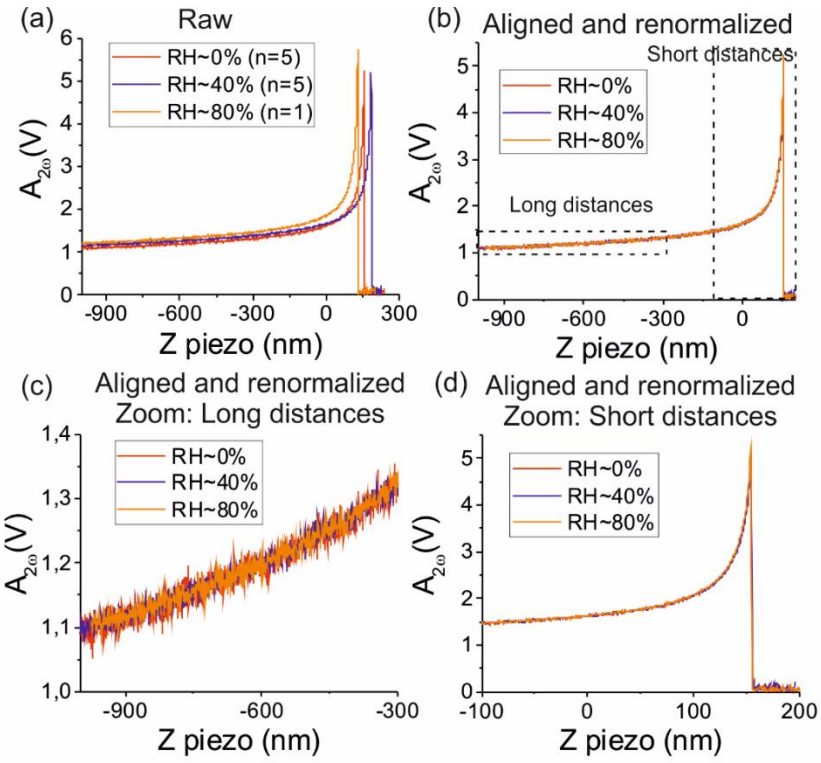

Figure 8.6 (a) Raw measured 2ω oscillation amplitude as a function of piezo displacement for three different environmental conditions (red RH~0%, blue RH~40% and orange RH~80%), corresponding to the measurements performed on the bacterial endospore shown in Figure 8.1. Each curve is a representative curve selected among the N=5 curves measured consecutively in each environmental condition. (b) Same as in (a) but with the curves at RH~40% and RH~80% aligned horizontally with the curve at RH~0% and renormalized by a multiplicative factor, *f*, that makes the long distance part of the curve to coincide (f_{RH40}=0.94 and f_{RH80}=0.91 in the present case). These factors are attributed to changes in the optical lever sensitivity caused by a readjustment of the laser spot when changing the environmental humidity conditions. Their values are consistent, within the experimental uncertainty, with the ratios between the optical lever sensitivities measured from the D-z curves ($f_{RH40,th}$= $m_{PDS,RH0}$/ $m_{PDS,RH40}$=0.94±0.09 and $f_{RH80,th}$= $m_{PDS,RH0}$/ $m_{PDS,RH80}$=0.99±0.13, where $m_{PDS,RH0}$=2.95±0.16 mV/nm, $m_{PDS,RH40}$=3.15±0.24 mV/nm and $m_{PDS,RH80}$=2.99±0.36 mV/nm). (c) and (d) zooms in of (b) for the long

and short distance ranges, respectively. The aligned and renormalized curves align, also, nicely in the short distance range meaning that the tip geometry has not changed during all the measurements.

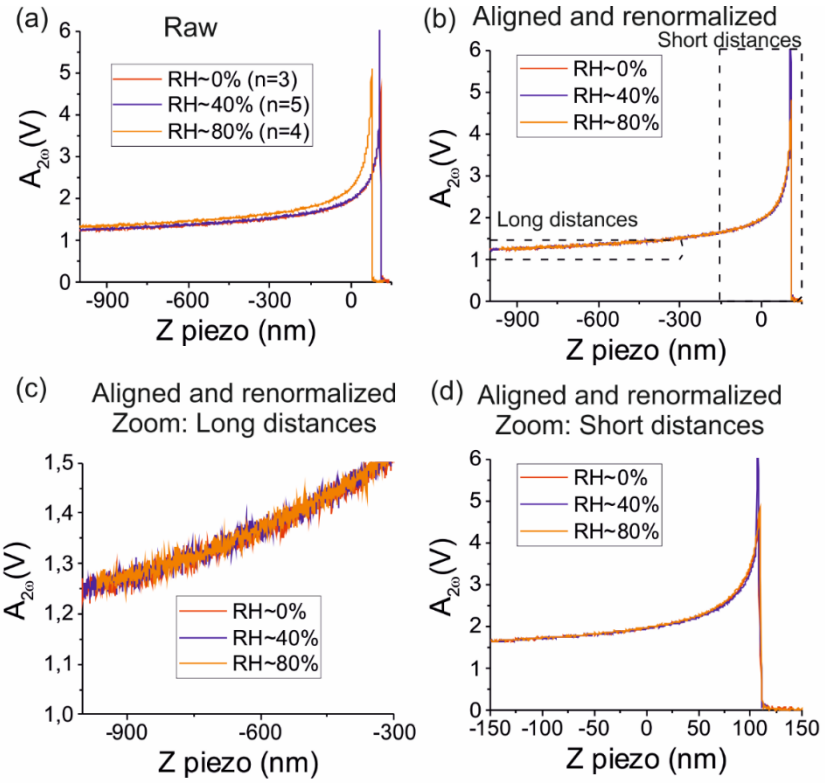

Figure 8.7 (a) Raw measured 2ω oscillation amplitude as a function of piezo displacement for three different environmental conditions (red RH~0%, blue RH~40% and orange RH~80%) for the measurements performed on the bacterial cell shown in Figure 8.2. Each curve is a representative curve selected among N=5 curves measured consecutively in each environmental humidity condition. (b) Same as in (a) but with curves at RH~40% and RH~80% aligned horizontally with the curve at RH~0% and multiplied by a factor, *f*, that makes the long distance part of the curve to coincide ($f_{RH40,exp}$=0.99 and $f_{RH80,exp}$=0.945). (c) and (d) zooms in of (b) for the long and short distance ranges, respectively. Again, the factors are consistent, within the experimental uncertainty, with the ratios between the measured optical lever sensitivities in each case, which in the present case were $f_{RH40,th}=m_{PDS,RH0}/m_{PDS,RH40}$=0.96±0.06 and

$f_{RH80,th}=m_{PDS,RH0}/m_{PDS,RH80}=0.99\pm0.09$, where $m_{PDS,RH0}=3.10\pm0.15$ mV/nm, $m_{PDS,RH40}=3.23\pm0.13$ mV/nm and $m_{PDS,RH80}=3.10\pm0.25$ mV/nm. The aligned and renormalized curves align, also, nicely in the short distance range meaning that the tip geometry has not changed during all the measurements.

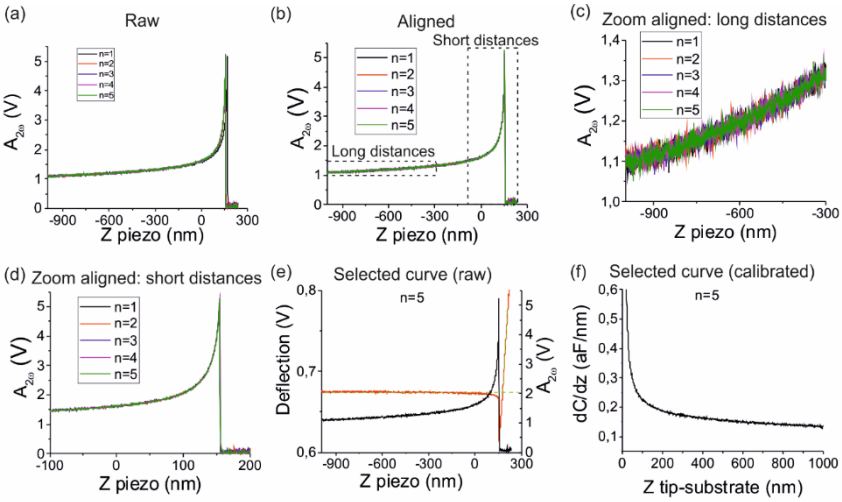

Figure 8.8 (a) Raw measured 2ω oscillation amplitude as a function of piezo displacement (N=5 curves). (b) Same as in (a) after aligning the different curves with respect to a reference curve, n=5 in this case (Z shifts -14.7 nm, -3 nm, -1.7 nm and -1.5 nm, respectively). (c) and (d) zooms in of (b) for the long and short distance regions, respectively. As it can be seen by just aligning the curves horizontally they look almost identical, meaning that neither the photodiode sensitivity has changed (factor f=1 for all curves with respect to the curve n=5) nor the tip geometry. (e) Simultaneously measured 2ω amplitude and deflection approach curves for n=5. The vertical line in the deflection curve corresponding to $D_0(V)$=0.675 V is used to set the Z=0 nm piezo distance ($Z_{0,piezo}$=176.2 nm), while the slope is used to convert the oscillation amplitude curve to aF/nm, giving m_{PD}=2.95 mV/nm. (f) Calibrated capacitance gradient curve as a function of tip-sample distance obtained by using Eq. (8.1) and by setting $Z_{tip\text{-}substrate}=Z_{piezo}-Z_{0,piezo}+(D-D_0)/m_{PD}$.

8.5.2 Topography tip de-convolution

The endospore and vegetative cell dimensions are obtained from the topographic image by following the procedure detailed in Ref. [45], with the difference that in the present case we included the convolution due to the cone contact region, since the apex radius is not larger than half the endospore or vegetative cell heights. In Figure 8.9 we show the results obtained for the endospore and vegetative cell corresponding to the data in Figure 8.1 and 8.2

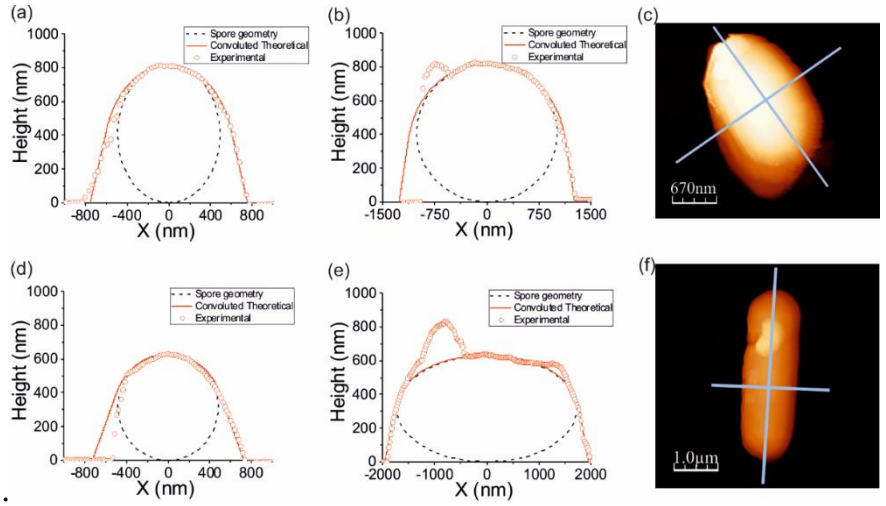

Figure 8.9 (a) (Symbols) Experimental transversal topographic cross-section of the endospore and (red line) corresponding theoretical convoluted profile for a superellipse with n_t=2.003 and a probe with R=133 nm and θ=20º, giving a geometrical width for the endospore w=980 nm. The dashed line represents the cross-section of the actual extracted ellipsoid. (b) Idem for the longitudinal direction. In this case n_l=2.067, giving l=2020 nm. (c) Topographic image of the endospore with the lines along the profiles which have been determined. (d) (Symbols) Experimental transversal topographic cross-section of the bacterial cell and (red line) corresponding theoretical convoluted profile for a superellipse with n_t=2.014 and a probe with R=63 nm and θ=27º, giving a geometrical width for the bacterial cell w=960 nm. The dashed line represents the cross-section of the actual extracted ellipsoid. (e) Idem for the longitudinal direction. In this case n_l=2.163, giving l=3450 nm. (f) Topographic image of the bacterial cell with the lines along which the profiles have been determined.

8.5.3 Experimental data for different lift distances

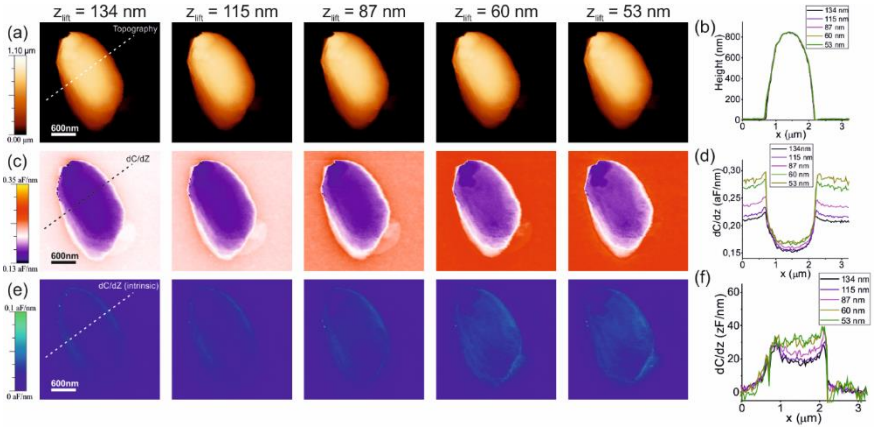

Figure 8.10 (a) Topographic images and (b) corresponding cross-section profiles along the line in (a) of the endospore at RH 0% for the different lift distance measurements shown in Figure 8.1n. (c) and (d) idem for the lift capacitance gradient measurements shown in Figure 8.1n. (e) and (f) idem for the intrinsic capacitance gradient measurements shown in Figure 8.1o.

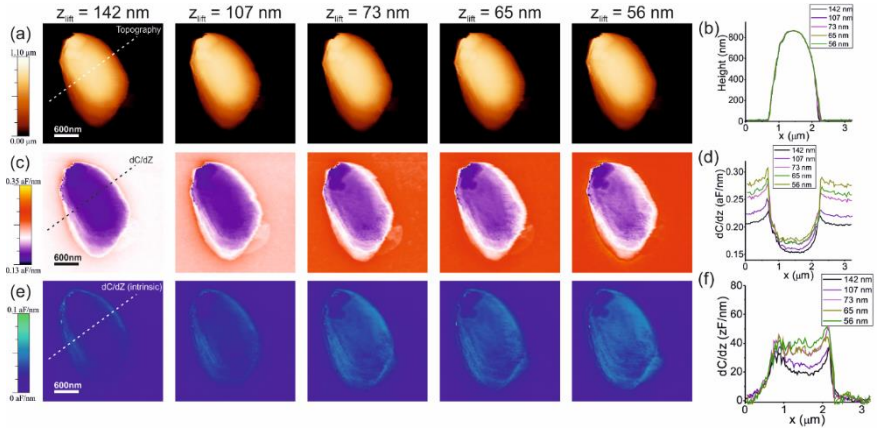

Figure 8.11 (a) Topographic images and (b) corresponding cross-section profiles along the line in (a) of the endospore at RH 40% for the different lift

distance measurements shown in Figure 8.1n. (c) and (d) idem for the lift capacitance gradient measurements shown in Figure 8.1n. (e) and (f) idem for the intrinsic capacitance gradient measurements shown in Figure 8.1o.

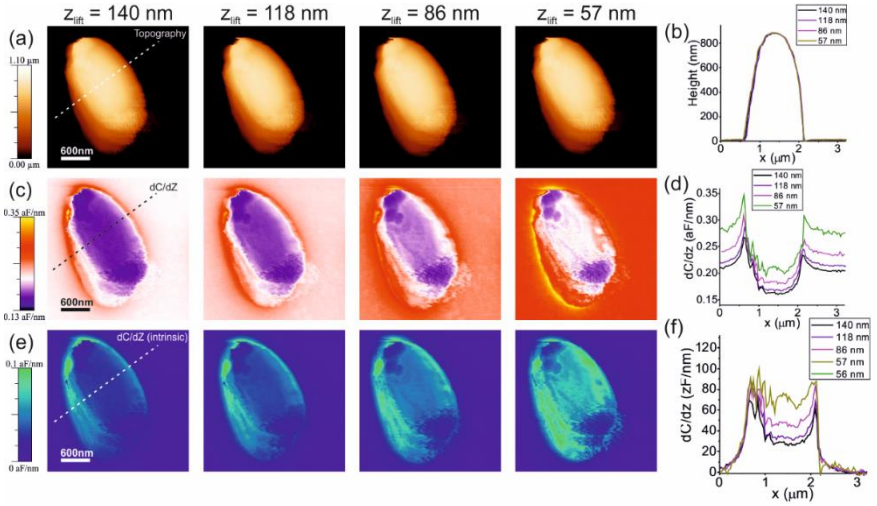

Figure 8.12 (a) Topographic images and (b) corresponding cross-section profiles along the line in (a) of the endospore at RH 80% for the different lift distance measurements shown in Figure 8.1n. (c) and (d) idem for the lift capacitance gradient measurements shown in Figure 8.1n. (e) and (f) idem for the intrinsic capacitance gradient measurements shown in Figure 8.1o.

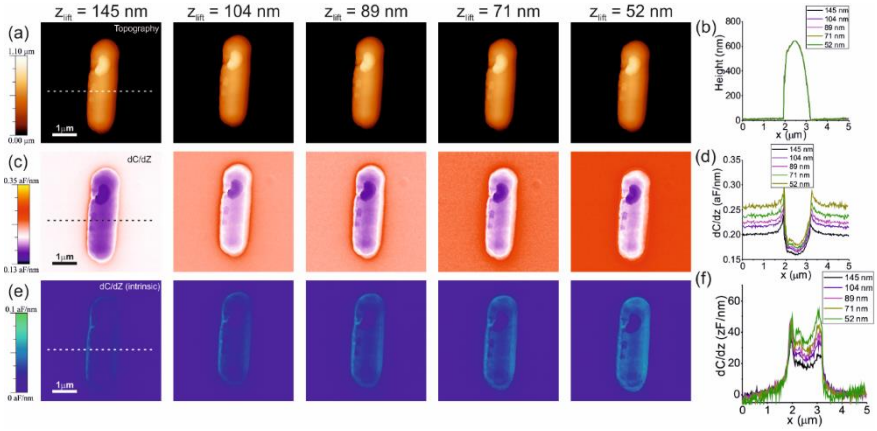

Figure 8.13 (a) Topographic images and (b) corresponding cross-section profiles along the line in (a) of the vegetative cell at RH 0% for the different lift distance measurements shown in Figure 8.2n. (c) and (d) idem for the lift capacitance gradient measurements shown in Figure 8.2n. (e) and (f) idem for the intrinsic capacitance gradient measurements shown in Figure 8.2o.

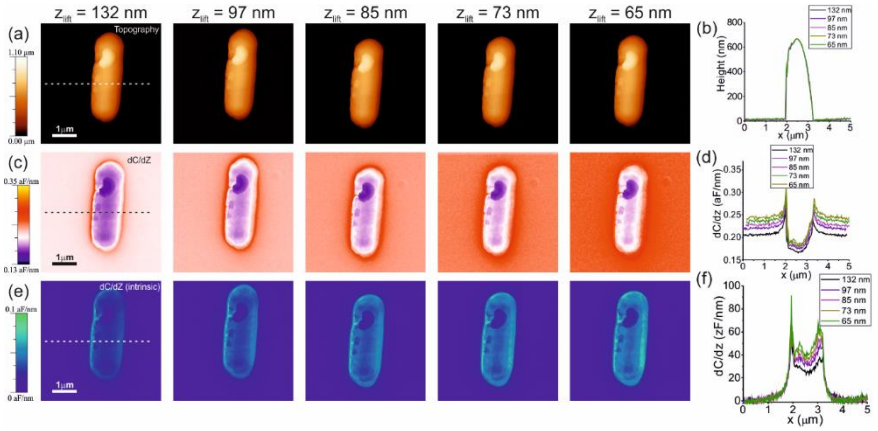

Figure 8.14 (a) Topographic images and (b) corresponding cross-section profiles along the line in (a) of the vegetative cell at RH 40% for the different lift distance measurements shown in Figure 8.2n. (c) and (d) idem for the lift capacitance gradient measurements shown in Figure 8.2n. (e) and (f) idem for the intrinsic capacitance gradient measurements shown in Figure 8.2o.

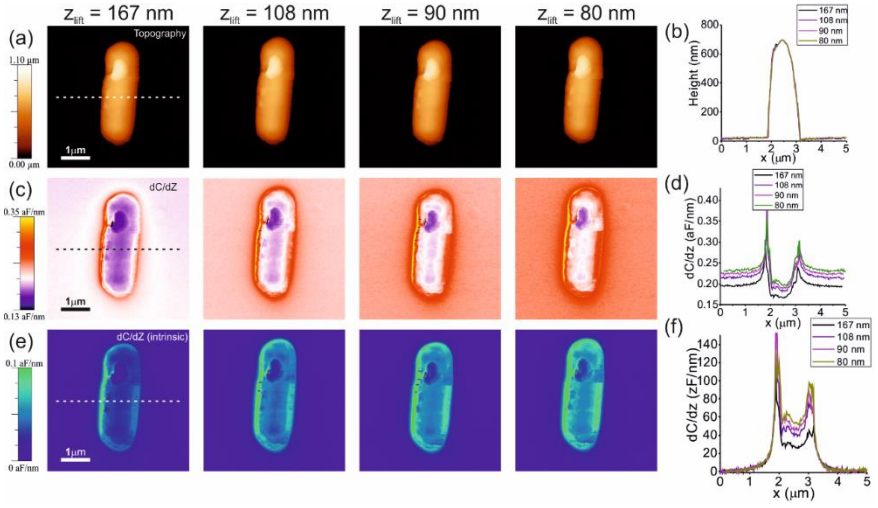

Figure 8.15 (a) Topographic images and (b) corresponding cross-section profiles along the line in (a) of the vegetative cell at RH 80% for the different lift distance measurements shown in Figure 8.n. (c) and (d) idem for the lift capacitance gradient measurements shown in Figure 8.2n. (e) and (f) idem for the intrinsic capacitance gradient measurements shown in Figure 8.2o.

8.5.4 Transmission electron microscopy image of the bacterial cell

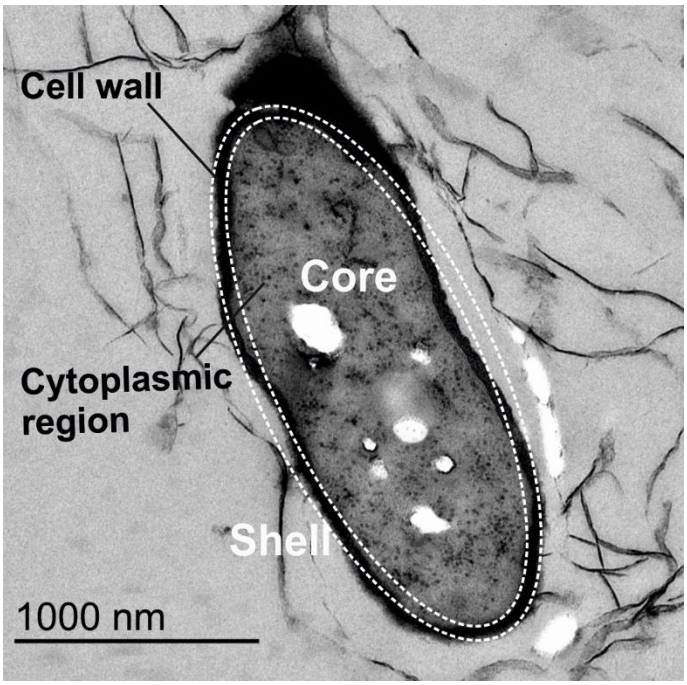

Figure 8.16 Transmission electron microscopy image of a vegetative cell, with its main parts indicated. The dashed line is a schematic representation of the core-shell model used in the theoretical calculations.

9 Electrical characterization of bacterial samples under liquid conditions

In chapter 8 we showed the hydration distribution of bacterial vegetative cells and endospores through a sequence of increasing relative humidity. The next step is to fully characterize the hydration capabilities of the bacterial samples under liquid conditions. With the capability of the Electrostatic Force Microscope to obtain electrical images of topographically tall samples as presented in chapter 7, we further asses it on bacterial samples under liquid conditions. We observed that while living bacterial samples of *E. coli* do not show electrical contrast under liquid conditions, re-hydrated *E. coli* bacterial vegetative cells and bacterial *B. cereus* endospores do. Results correlate with the complexity in structure and the lower hydration in comparison to living bacterial cells. These results show the capability of the Electrostatic Force Microscope to characterize structure and hydration levels under liquid conditions of living bacterial cells, which can be of relevance to study hydration states of living organism under liquid conditions.

9.1 Introduction

In chapter 4 we have demonstrated the drastic effect the drying process has on living bacterial samples, reducing strongly its height and killing them. This phenomena happens because water is an essential molecule for living organism, especially for those organism in which the water constitutes its natural niche, such as in the case of bacteria. For this reason, biological studies are constantly being pushed forward to be performed under liquid conditions, to mimic natural conditions.

On the other hand, the bacterial endospores are dormant and do not suffer from dehydration. Nevertheless, they need to be under liquid conditions in order to germinate and give rise to a vegetative cell. Therefore, it can be attributed that liquid conditions are not the native conditions for the bacterial endospores, but are essential for its germination.

For this reason, the last measurements of this work of thesis are focused in observing the hydration properties of bacterial samples under liquid conditions through the measurement of its electrical properties. To do so, the EFM system explained in chapter 7 is used to measure living bacterial cells, re-hydrated vegetative bacterial cells and bacterial endospores under milli-Q water.

9.2 Electrical images of living bacterial cells.

As used in chapter 7, electrical images under liquid conditions are performed by a two pass mode, where during the first pass the topography is acquired while during the second pass the capacitance gradient image is extracted. In this case, dynamic jumping mode was used as the topographical imaging mode since as observed in chapter 4, a weak imaging technique is essential to be able to image individual bacteria. Before starting the second pass, the mechanical oscillation is interrupted and an electrical potential is applied (with the help of a switch), with an amplitude and frequency of 2V rms and 44MHz, respectively, modulated by an electrical potential of amplitude and frequency 0.8V rms and 2 kHz, respectively. During the second pass, the electrically induced oscillation amplitude at the first excitation frequency ($A\omega$) is measured by an external lock-in amplifier (Anfatec instruments AG). In this chapter capacitance gradient images have been performed in lift mode and in constant height during the second pass.

In chapter 4 gold Biolevers (Olympus) were used due to their low spring constant and the presence of metallic coating, which were an important aspect to obtain images of living bacterial cells. The usage of such conductive probes was thought to allow future electrical measurements. Nevertheless, the Biolevers probes presented little local electrical contribution under liquid conditions (data not shown). It has been predicted from the shape of the capacitance gradient curve and previous results shown by members of the research group in air [131], that the probe's small cone hinders the electrical locality of the apex. The use of the CDT-CONTR probes, as used in the previous chapters for air measurements, present the limitation of a larger spring constant (an order of magnitude greater). The slight increase of the cone height will not outweighed the increase in

difficulty of imaging under liquid conditions living bacteria cells due to the increase of the spring constant.

The complexity of electrically imaging living bacterial cells under liquid conditions meant the use of nonconventional probes, such as those distributed by Rocky Mountain Nanotechnology (solid wire probes). The advantage presented by these platinum probes for electrical imaging is the large cone (~80μm), which is 20x greater than the Biolevers probe's cone. In this case, the large increase of the cone compensates for the increase in the spring constant (one order of magnitude). It is important to remark the difficulty in using stiffer and nonconventional probes (a solid wire) to image living bacterial cells.

Although dynamic jumping mode was used to image living bacterial cells, the use of the nonconventional probes could only allow the observation of bacterial cells when they were present on the image boundaries. This singularity was attributed to a reduction of the shear forces exerted on the bacteria. Figure 9.1a shows AFM topographic image of two living *E. coli* bacterial cells on a gelatinised gold substrate. The region of the imaged bacteria are not large enough to calculate the lateral dimensions, but from cross-sections the extracted topographic height is ~1020nm (Figure 9.1b), which is in close agreement with the results obtained for living bacterial *E. coli* cells in chapter 4.

Figure 9.1c shows capacitance gradient image obtained in lift mode, at a lift distance of ~200nm. This electrical imaging distance is great enough to prevent the overlapping of the EDL layers and achieve contrast of the bacterial cells under study. A large signal to noise level can be observed on the bacteria (Figure 9.1d), with special remark on the fact that electrical contrast is obtained for the entire sample. As presented in chapter 5, capacitance gradient images obtained in lift mode must be handled with precaution, since a large contribution comes from topographic crosstalk contributions.

A constant height electrical image performed on the same bacterial cells revealed no electrical contrast (image not shown). To rule out that the image at constant height was performed too far from the sample, capacitance gradient approach curves on the substrate and on the bacterial cell were measured and superimposed (Figure 9.1e). The curve on the bacterial cell was shifted on the Z axis by its height to be able to predict the electrical contrast obtained at constant height dependent upon the probe sample separation. Curve superposition

revealed no contrast of the living bacteria cell independently of the probe sample separation used.

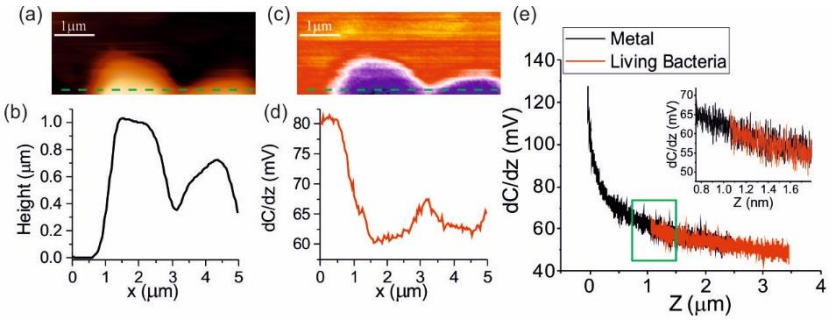

Figure 9.1 (a) Topographic image of a fragment of two living *E. coli* bacterial cells on top of a gelatinized gold substrate. (b) The corresponding cross-section profile along the green line in (a). (c) Capacitance gradient image for the matching topographical image at a lift distance of ~200nm. (d) Corresponding capacitance gradient cross-section profile along the green line in (c). (e) Capacitance gradient approach curve performed on the gelatinized gold substrate (black) and the gelatinised gold substrate (red), with the second shifted in the *Z* axis by the bacterial cell height. The inset shows a zoom of the most significant values,

9.3 Electrical images of dried re-hydrated bacterial cells

Figure 9.2a shows AFM topographic image of a re-hydrated EAEC bacterial cell on gelatinised gold substrate. As in the previous case with living bacterial cells, imaging of the sample is achieved when the samples are in the boundaries of the images. Cross-section analysis (Figure 9.2b) revealed a predicted height of ~980 nm for the re-hydrated bacteria, which is in close agreement with the previous results obtained in chapter 4.

Capacitance gradient image in constant height mode revealed an electrical contrast for the re-hydrated bacterial cell at a probe sample separation of ~145nm (Figure 9.2c), with a greater signal to noise level (Figure 9.2d) compared to the

previous results in chapter 7 of the gelatine. This results predict that the re-hydrated bacterial cells have a smaller effective dielectric value in comparison to the gelatine. Furthermore, the contrast presented by the re-hydrated, and the absence in contrast presented by the living bacterial cells confirms the statement that the gelatine coating would not hinder the electrical response of the samples deposited on top.

The comparison between the topographical cross-section (Figure 9.2b) and the capacitance gradient cross-section (Figure 9.2c) reveals the large lateral effect present in electrical measurements performed under liquid conditions in comparison to those performed in air (chapter 5). Bacterial topography decreases from its maximum height to the substrate in ~1 μm, while on the other hand the electrical signal needs double the distance to increase up to the EFM substrate levels. This shows the large sensitivity Electrostatic Force Microscopy has under liquid conditions, with special interest in having a greater penetration in comparison to measurements performed in air.

Difference between living bacterial cells and re-hydrated bacterial cells due to the difference in electrical signal must be stated with precaution. In the case of re-hydrated bacterial cells, the smaller in size could be an indication that dried bacterial cells do not hydrate as much as living bacterial cells under liquid conditions (~77% [175]), and hence showing a lower dielectric value due to a lower water content. Furthermore, during the drying process, the bacterial cells collapse onto the substrate. This could cause the compaction of the cytoplasm content to form a dense matrix of organic material which does not hydrate as much as the cytoplasm, and hence presenting an effective lower dielectric value. Yet, from chapter 8 we observe that the core of the bacterial cell at high relative humidity increases its effective dielectric value up to 60-70, which is smaller than that of water ($\varepsilon_{r,\ water}$~80).

From another point of view, it must be taken into consideration that the living bacterial cells have free ions in its cytoplasm which could give rise to conduction and affect EFM measurements. Nevertheless, these results further indicate, as previously argued in chapter 4, the alteration the drying process has on the living bacterial cells. Although re-hydrated bacterial cell present a size similar to that of the living bacterial cells, their composition changes, since a different electrical behaviour is observed.

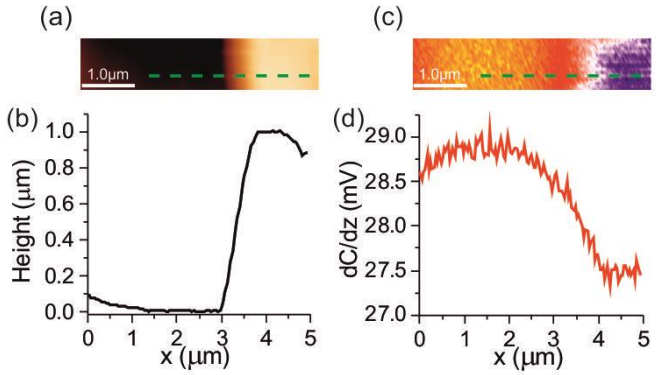

Figure 9.2 (a) Topographic image of a fragment of a re-hydrated EAEC bacterial cells on top of a gelatinized gold substrate. (b) The corresponding cross-section profile along the green line in (a). (c) Capacitance gradient image for the matching topographical image at a constant height of ~1125nm with respect to the substrate. (d) Corresponding capacitance gradient cross-section profile along the green line in (c).

9.4 Electrical images of bacterial endospores

Chapter 8 shows that bacterial endospores are more reluctant to hydration under low and high relative humidity compared to bacterial vegetative cells. Under liquid conditions, research has shown that bacterial endospores only hydrate up to 65%, being lower than bacterial vegetative cells [175]. Under liquid conditions, the core hydrates but remains the driest part of the endospores [23,147,148]. The observation of bacterial endospores under liquid conditions will fulfil the electrical characterization of bacterial samples (vegetative cells and bacterial endospores) under different environmental conditions. For the observation of *B. cereus* bacterial endospores under liquid conditions, sample preparation as chapter 8 is followed, and subsequently milli-Q water is added.

Bacterial endospores presented a stronger attachment to the gold substrate than its vegetative form, and could be directly imaged using dynamic jumping mode without the need of the gelatine coating (Figure 9.3a). The observed endospore height under liquid conditions, ~1015nm, does not differ largely from the values

extracted in air conditions or with the living vegetative form (Figure 9.3b). The peak observed in the cross-section profile is attributed to the presence of the exosporium, which does not collapse in liquid conditions as it does in dry conditions [33]. The prediction in the increase in spore size due to the complete hydration under liquid conditions is challenging, especially due to the large variability in endospore size [176].

Figure 9.3c shows capacitance gradient image obtained in lift mode, at a lift distance of ~650nm. Although a nice electrical image is observe with a high signal to noise level of the entire spore (Figure 9.3d), as previously shown a large contribution (if not all) could be due to topographic crosstalk. To make sure all electrical contrast is due to the sample intrinsic properties, capacitance gradient image in constant height mode at ~285nm probe spore distance was obtained (Figure 9.3e). The ellipsoidal contrast shape in the capacitance gradient image shows the local capabilities of the EFM under liquid conditions, since the endospore sample itself has such shape. As previously observed, from the cross-section profile it can be observed a large lateral and/or penetrability of the EFM signal, since the reduction in the EFM signal is not as steep as in air conditions [21].

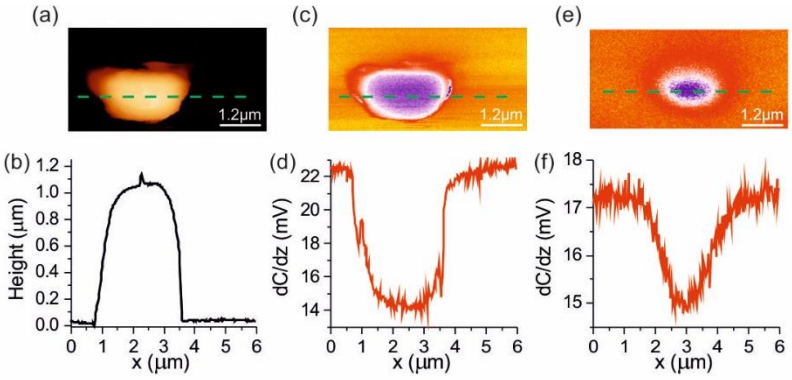

Figure 9.3 (a) Topographic image of a fragment of a re-hydrated EAEC bacterial cells on top of a gelatinized gold substrate. (b) The corresponding cross-section profile along the green line in (a). Capacitance gradient image for the matching topographical image at a lift distance of ~650nm. (d) Corresponding capacitance gradient cross-section profile along the green line in (c). (e) EFM capacitance gradient image for the matching topographical image at a constant height of ~1300nm with

respect to the substrate. (f) Corresponding capacitance gradient cross-section profile along the green line in (e).

The structure of the mature endospore consists of compacted layers, as explained in chapter 2. The compaction and the low hydration of the endospore, of only up to ~65% of its weight, causes a lower effective dielectric value than water, and hence creates an EFM contrast upon imaged. The signal to noise level is just under the re-hydrated bacterial cell results, indicating an effective greater hydration of the bacterial endospore compared to the re-hydrated bacterial cell, which could be due to the difference is structure.

The germination of bacterial endospores causes the breakdown and expansion of the cortex, causing the appearance of pores on its surface [14]. This expansion has been observed to be accompanied by an increase of the water content up to 73% [175], changing its structure towards a living bacterial vegetative cell. The lower hydration of the mature endospore could be the key factor in preserving bacterial endospore dormancy under liquid environments.

9.5 Conclusions

We have demonstrated that Electrostatic Force Microscopy can be applied to biological organism under liquid conditions. In particular we have demonstrated that living bacterial cells present no electrical contrast, in contraposition to re-hydrated bacterial cells or bacterial endospores. These results suggested that living bacterial cells hydrate to a greater extent than its dried homologous or a bacterial endospore, following the pattern previously observed in chapter 8. In addition, bacterial endospores show a greater hydration compared to re-hydrated bacterial cells. The large sensitivity of the EFM under liquid conditions shows the possibilities of the EFM for subsurface characterization at deep penetrations. Present results show the potential of EFM under liquid conditions to characterize internal hydration properties of large biological organism, with important implications in life sciences.

10 Conclusions and future perspective

10.1 Conclusions

The objective of the present work of thesis was to study the hygroscopic properties of single individual bacterial samples over the full range of environmental conditions, with special interest on dormant endospores. To achieve such goal, the Electrostatic Force Microscope was used to measure the electrical properties of bacterial vegetative cells and bacterial endospores at the single cell level under dry, humid and liquid environments.

The difficulty to observe living bacterial cells in its native living conditions (under liquids conditions with a weak adhesion onto the substrate) has always been a major issue for nanomicrobiological studies. To address this issue, we used biocompatible gelatinous coated planar substrates to weakly attach bacterial cells, and the use of dynamic jumping mode as a powerful technique due to its drastic reduction on the shear forces provoked on the sample as compared to conventional AFM imaging. This methodology allowed us to observe *in situ* bacterial cell division at the single cell and nanoscale resolution.

The large non-planar morphology of bacterial samples limited the use of constant height EFM, expertise of the research group. The problematic in the use lift-mode Electrostatic Force Microscopy is the topographical crosstalk contribution which hinders the intrinsic contribution from the sample under study. To this point, a quantitative analysis of lift mode EFM for nanoscale dielectric characterization was undertaken, revealing a greater capability of obtaining the local dielectric properties of the sample under study. The use of inorganic calibration samples and of single bacterial cells revealed the need of the proposed method for quantitative analysis of the dielectric properties of such highly non-planar samples, revealing electrical homogeneity of such samples.

The detection of gold pellets buried under a SiO_2 matrix revealed the capabilities of the Electrostatic Force Microscopy as a tool for subsurface characterization. The ability to detect a 200nm separation between two 200nm golden pellets at a large probe pellet separation showed the capability of EFM to

detect heterogeneities of deep subsurface samples. The resemblance between the SiO_2 matrix thickness with those of the bacterial samples under study revealed the potential of the EFM to detect water distribution within the bacterial cell samples under study in this work of thesis.

Following with the capabilities of the Electrostatic Force Microscopy, the ability to obtain electrical images under liquid conditions of topographical tall samples shows that the locality of the electrical signal is not lost at large distances from the substrate. Furthermore, the low contrast exhibited by the gelatine under liquid conditions indicates the gelatine would not hinder the electrical contrast of a deposited sample on top of it. These results are of special interest for the electrical measurements of bacterial cells under liquid conditions, their native conditions.

The electrical characterization of bacterial vegetative cells and bacterial endospores under a range of different relative humidity allowed us to study the difference in hygroscopic properties between the two samples. At low relative humidity, 40% RH, the bacterial endospores hardly hydrate in comparison to the bacterial vegetative cells. At high relative humidity, 80% RH, the bacterial vegetative cells drastically hydrate in comparison to the bacterial endospores. In the latter case, it has been demonstrated that the external layers accommodate most of the moisture absorbed, leaving the core at low hydration levels. In the case of the vegetative cells, the cell wall is not able to accommodate such high levels of moisture, forcing the cytoplasmic region to become highly hydrated. This discrepancy in the hydration behaviour seems key for the persistence of the core region as the driest region of the bacterial endospores in atmospheric conditions. This could be one of the basis of the large water responsive properties of the bacterial endospores to extend dormancy.

Finally, electrical measurements performed under liquid conditions fulfilled electrical measurements to characterize the hydration properties of bacterial samples. The absence of electrical contrast observed in living bacterial cells shows the high levels of hydration of such organism under liquid conditions. In contraposition, its re-hydrated homologous and the bacterial endospores do present electrical contrast, showing a difference in hydration pattern. This lower hydration could be attributable to difference in structure, such as the case of bacterial endospores which is consisted of concentric layers of proteins. This sensitivity under liquid conditions opens new possibilities of the EFM under

liquid conditions for subsurface characterization of large biological organism, with especial remark on the hydration properties.

All together these results obtained in this work of thesis have shown the lower hydration properties of single bacterial endospores in contraposition to its vegetative cell in all environmental conditions, from dry conditions up to liquid environments.

10.2 Future perspectives

Research is an ongoing career with no end. This thesis showed the difference in the hygroscopic properties between the wild type bacterial vegetative cell and its endospore with nanoscale resolution. The use of mutants that modify the composition or structure of the cortex, could give rise to the explanation of the bacterial endospore capability to not hydrate as much as its vegetative form, leaving the core in a drier state. This could open new technological approaches for water absorption materials.

The study of more complex internal structures in bacterial samples, such as bacteria that form nanoparticles, have magnetomes or express air vacuoles for buoyancy could be studied *in situ*. Their time of formation, speed, localization or excretion are just some of the traits that could be studied *in situ*, which has not been observed up to date. Not restricting to the microbiology field, Electrostatic Force Microscopy and its ability to measure hydration properties can be explored into other fields. The eukaryotic cell is well known for also its complexity in organelles, which could be a promising target to use with. The *in situ* inner characterization of liposomes could be assessed since they are a well know system due to their potential in drug delivery systems.

11 Appendix

11.1 Acknowledgments

This section should be the easiest part, but it is actually resulting to be the most difficult. Reaching this point means that the project is over, which opens the box of memories, and most importantly, that reaching this point has not only been accomplished by hard work, but also by scientific and social support.

Starting from the very beginning, I will like to thank to the people which introduced me into this field and to whom I'm grateful for the selection of the adequate group. Entering the group with basic foundations in nanotechnology, I wouldn't have advanced without the teachings from Esteban, Dols, Calò and Otero, from the most basic concepts up to the most advanced and *irresponsible* use of the AFM. Thank also to my generation in the Nanobioelec group, the "*A team*" (Rene and Maria Chiara), for the help with scripts and theoretical discussion, but greatest of all for the momentary disconnection from work for any random discussion. To the established new generation (Marti, Helena and Ruben), I'm indebted for entering with such vitality, making ending of doctorate more amenable, although I foresee a chaos in the lab, although you will find everything in the first draw.

To whom *struggles* to control the Nanobiolec group, Gabriel Gomila, I am grateful for its support with respect to the theoretical points of view, its essential criticism and especially for his thesis supervision. Treating me as an equal, he has shown me that a conversation between a biologist and a physicist is not easy, and furthermore that a biologist can reach to the point of explaining things to physicist.

For the assistance on the most microbiology aspects, I must appreciate the Antonio Juarez's group, with special emphasis to Sonia and Mari for their handy bench-work tricks and discussions.

Making the long journey amusing, I must thank specially members and formers members which whom I have relished and suffered the IBEC's PhD student committee. With them, dinners, hiking, parties, calçotades, bowling, dancing

classes, karaoke, discussions, after-parties, crazy races, expositions are just examples of the activities which they dealt with me. Furthermore, I must thank fellows and sports' companions for the need in special occasions to completely disconnect from IBEC. I do have to reserve some words of beholden to Luis, Xavi and Laura from the Electronic department for their shared knowledge and welcoming attitude whenever it was needed.

I must end with exclusive gratefulness to close relatives. To my family for their interest and backing to achieve up to where I stand now. To Clara for her constant encouragement day after day.

11.2 Publications

- *Nanoscale imaging of the growth and division of bacterial cells on planar substrates with the atomic force microscope*, **M. Van Der Hofstadt**, M. Hüttener, a. Juárez, G. Gomila, Ultramicroscopy. 154 (2015) 29–36. doi:10.1016/j.ultramic.2015.02.018.

- *Nanoscale Electric Permittivity of Single Bacterial Cells at Gigahertz Frequencies by Scanning Microwave Microscopy*, M.C. Biagi, R. Fabregas, G. Gramse, **M. Van Der Hofstadt**, A. Juárez, F. Kienberger, L. Fumagalli, G.Gomila, ACS Nano. 10 (2016) 280–288. doi:10.1021/acsnano.5b04279.

- *Nanoscale dielectric microscopy of non-planar samples by lift-mode electrostatic force microscopy*, **M. Van Der Hofstadt**, R. Fabregas, M.C. Biagi, L. Fumagalli, G. Gomila, Nanotechnology. 27 (2016) 405706. doi:10.1088/0957-4484/27/40/405706.

- *Internal hydration properties of single bacterial endospores probed by environmental electrostatic force microscopy*, **M. Van Der Hofstadt**, R.

Fabregas, R. Millan-Solsona, L. Fumagalli, A. Juarez, G. Gomila. Submitted.

- Revealing tomography structures with EFM. R. Fabregas, **M. Van Der Hofstadt**, L. Fumagalli, G. Gomila. In preparation.

11.3 Congress presentations:

- 9th IBEC Symposium on Bioengineering for Active Ageing (Barcelona, Spain) 2016. Local hydration properties of single bacterial cells and spores by lift-mode Electrostatic Force Microscopy, **Marc Van Der Hofstadt**, R. Fabregas, M. C. Biagi, L. Fumagalli, A. Juárez, G. Gomila. Poster & Oral Contribution

- AFM BioMed 2016 (Porto, Portugal) 2016. *Local hydration properties of single bacterial cells and spores by lift-mode Electrostatic Force Microscopy*, **Marc Van Der Hofstadt**, R. Fabregas, M. C. Biagi, L. Fumagalli, A. Juárez, G. Gomila. Oral Contribution

- 6th Multifrequency AFM (Madrid, Spain) 2016. *Nanoscale Electric Permittivity of Single Bacterial Cells at Gigahertz Frequencies by Scanning Microwave Microscopy*. Maria Chiara Biagi, Rene Fabregas, Georg Gramse, **Marc Van Der Hofstadt**, Antonio Juárez, Ferry Kienberger Laura Fumagalli, and Gabriel Gomila. Oral contribution.

- EMBO|EMBL Symposium: Seeing is believing - Imaging the Processes of Life (Heidelberg, Germany) 2015. *Nanoscale imaging of the growth and division of bacterial cells on planar substrates with the AFM*, **M.**

Van Der Hofstadt, A. Juarez, G. Gomila. Poster contribution with selected poster to present with an elevator pitch.

- Nanomeasure 2015 (Barcelona, Spain) 2015. *Nanoscale imaging of the growth and division of bacterial cells on planar substrates with the AFM,* **M. Van Der Hofstadt**, A. Juarez, G. Gomila. Oral contribution

- 8th IBEC Symposium Bioengineering for regenerative therapies (Barcelona, Spain) 2015. Quantitative lift mode electrostatic force microscopy applied to bacterial spores, **M. Van Der Hofstadt**, R. Fábregas, M.C. Biagi, L. Fumagalli, A. Juárez, G. Gomila. Poster & Oral contribution.

- 7th IBEC Symposium Bioengineering for future Medicine (Barcelona, Spain) 2014. *New approach to image single bacterial division on gelatine coated substrates with the Atomic Force Microscope,* **M. Van Der Hofstadt**, A. Juarez, G. Gomila. Oral & poster contribution

- International Conference on Scanning Probe Microscopy on Soft and Polymeric Materials (SPM-on-spm) (Toronto, Canada) 2014. *New approach to image single bacterial division on gelatine coated substrates with the Atomic Force Microscope,* **M. Van Der Hofstadt**, A. Juarez, G. Gomila. Poster contribution

- 2a Jornada d'Investigadors Predoctorals Interdisciplinària (JIPI) (Barcelona, Spain) 2014. *Imaging living individual bacteria at the nanoscale with the Atomic Force Microscope (AFM),* **M. Van Der Hofstadt**, A. Juarez, G. Gomila. Oral contribution

11.4 Acronyms

AFM	Atomic Force Microscope
Bio-MEMS	Biological Microelectromechanical Systems
C-AFM	Conductive Atomic Force Microscope
EAEC	Enteroaggregative *Escherichia coli*
EDL	Electrostatic Double Layer
EFM	Electrostatic Force Microscope
KPFM	Kelvin probe Force Microscope
nanoSIMS	Nanoscale secondary ion mass spectrometry
NIM	Nanoscale Impedance Microscope
PCR	Polymerase Chain Reaction
RH	Relative Humidity
SCM	Scanning Capacitance Microscope
SECM	Scanning Electrochemical Microscope
SICM	Scanning Ion-Conductance Microscopy
SMM	scanning microwave microscope
SPFM	Scanning polarization Force Microscopy
SPM	Scanning Probe Microscopy
STM	Scanning Tunnelling Microscope
TEM	Transmission Electron Microscope

11.5 Resum en català

Els bacteris són atribuïts com l'organisme viu que millor s'ha adaptat al nostre planeta. Aquesta afirmació es basa sota la concepció que com més senzill és l'organisme, més ràpid pot evolucionar. A més, els bacteris són reconeguts com un dels primers organismes vius, per tant, la seva evolució i adaptació ha anat lligada amb el desenvolupament de les condicions ambientals de la terra. La gran adaptació dels bacteris es pot observar en la seva presència que és gairebé omnipresent a la terra. Es poden trobar a l'interior com l'exterior d'organismes vius, com en sòls i entorns líquids on poden sobreviure a condicions extremes (com ara temperatura, radioactivitat o salinitat entre d'altres). La seva adaptació i la seva presència és tal, que la suma de les cèl·lules bacterianes que es preveuen a la terra ($\sim 5x10^{30}$) tindria una biomassa més gran que la suma de les plantes i els animals.

La gran abundància de nínxols bacterians ofereix una rica diversitat de característiques bacterianes. Dins d'aquesta diversitat, algunes són avantatjoses i tenen un paper crucial en la salut i el creixement humà. Molts bacteris tenen un ús ampli al sector de la biotecnologia, on les aplicacions van des d'estudis biològics fonamentals (facilitat per modificar genèticament els bacteris), fins a l'explotació al sector mèdic i industrial (tal com en la producció d'antibiòtics, enzims, processament d'aliments o la generació de biocombustibles). Antagònicament, hi ha bacteris patògens que són de gran preocupació. Moltes soques bacterianes virulentes són responsables de malalties greus, com *Bacillus anthrcis* (Àntrax), *Corynebacterium diphteriae* (Diftèria) o *Vibrio Cholerae* (còlera), entre altres. Tal és la problemàtica dels bacteris virulents, que només el bacteri *Mycobacterium tuberculosi* és responsable de 2 milions de morts a l'any. Aquests dos punts conflictius d'interès condueixen a la necessitat de desentranyar completament les propietats dels bacteris.

Per establir una arquitectura dins el domini dels bacteris, s'ha establert l'anàlisi de la seqüència del RNA ribosomal com el principal mètode per a la seva classificació en espècies. Fins a la data, s'han descrit més de 10^4 espècies bacterianes. A causa de la gran diversitat existent dins d'una mateixa espècie bacteriana, hi ha hagut la necessitat de sub-dividir en soques. Com a exemple, dins l'espècie *Escherichia coli* hi ha soques beneficioses que ajuden a l'hoste en

la producció de vitamina K2, mentre que altres soques causen greus intoxicacions d'aliments [1]. Com a conseqüència, la classificació per RNA ribosomal és encara limitada.

Per la caracterització i diferenciació de les soques bacterianes s'utilitzen eines d'investigació de microbiologia tradicional. La caracterització es pot realitzar per la distinció en propietats immunològiques o fenotípiques. Sota la caracterització de trets immunològics, l'ús d'anticossos per detectar antígens de les cèl·lules bacterianes ajuden a descobrir propietats de la composició. De l'altra banda, la caracterització fenotípica es divideix en estudis bioquímics (que descobreixen la funcionalitat dels bacteris, com ara la detecció d'enzims específics per a una classificació segons el metabolisme) i estudis morfològics (que descobreixen estructures, com ara la forma cel·lular, mida, estructures especials, i morfologies macroscòpiques com el creixement i l'agregació de colònies). Amb el descobriment de la reacció en cadena de la polimerasa (PCR) en 1986, els estudis realitzats per la presència d'una seqüència genètica són anomenats com a eines de microbiologia moderna. No obstant això, aquests estudis genètics són corroborats amb les eines de microbiologia tradicional per enllaçar una seqüència genètica bacteriana a un atribut específic.

Les eines de caracterització de la microbiologia tradicional són limitades i poden ser restrictives a les espècies bacterianes més comunes. Aquesta limitació va empènyer la necessitat de noves tècniques no estàndard per complementar la caracterització bacteriana, on alguns trets podien ser específics per a una espècie bacteriana. Aquestes tècniques aborden les propietats físiques com la pressió mecànica (com la pressió turgent), la conductivitat elèctrica [2], propietats de bioluminescència [3], o les capacitats d'orientació amb els camps magnètics [4]. També hi ha altres propietats fisicoquímiques que són d'interès, especialment en el sector de la medicina, com ara les capacitats d'adherència [5], la hidrofobicitat [6] o les propietats higroscòpiques [7]. Amb l'excepció dels estudis estructurals específics (on s'utilitza el microscopi electrònic), la majoria de la microbiologia tradicional i les tècniques no convencionals es duen a terme a escala de colònies. Encara que una colònia microbiana sorgeix d'un bacteri individual, no totes les cèl·lules presents a la colònia són genèticament idèntiques a causa de la possible variabilitat estocàstica. Com a conseqüència, els milions de cèl·lules presents a una colònia produeixen una mitjana del fenotip, cosa que amaga l'heterogeneïtat de les cèl·lules individuals.

L'heterogeneïtat a les colònies de bacteris és important, ja que poden tenir conseqüències pràctiques en el sector mèdic (resistència a antibiòtics o agents patògens potencials) i la indústria alimentària (producció i conservació) [8]. D'altra banda, els trets individuals poden ser emmascarats per l'estudi a escala de colònies, com ara la polimerització d'actina o les proteïnes d'unió de superfície, que només són presents en els pols de les cèl·lules de *Listeria monocytegenes* i *Bradyrhizobium japonicum*, respectivament [9]. Per aquesta raó, l'estudi a escala de cèl·lules individuals és crucial per aconseguir una millor caracterització bacteriana.

Dins els estudis de cèl·lules bacterianes individuals, moltes tècniques diferents han estat desenvolupades. L'ús de sistemes microelectromecànics biològics (Bio-MEMS) basats en dielectroforesi, captura òptica o fluorescència (incloent-hi la citometria de flux, confocal, súper resolució, etc.), han demostrat la seva capacitat per extreure propietats específiques a escala de cèl·lules individuals [8]. La principal debilitat d'aquestes tècniques és la resolució assolible, la modificació de la mostra per a la seva observació, i/o la possibilitat de només extreure una característica alhora. Aquestes restriccions limiten la capacitat per estudiar a escala individual les cèl·lules bacterianes. Per complir amb aquesta bretxa, recentment s'estan explotant eines de nanotecnologia (Nanomicrobiologia [10]). Els exemples inclouen l'ús d'espectrometria de masses de ions secundaris a la nanoescala (Nano-SIMS) o la microscòpia de raigs X, que han contribuït a descobrir la composició química i estructural de les cèl·lules bacterianes individuals a la nanoescala [11,12].

El microscopi de forces atòmiques (AFM) s'està convertint en una eina prometedora per a la Nanomicrobiologia. El AFM és capaç de caracteritzar l'estructura de la cèl·lula bacteriana i obtenir al mateix temps altres propietats físiques d'interès. També pot manipular mostres i funcionar en condicions fisiològiques, sent aquesta capacitat d'interès important pel camp de la microbiologia. El AFM ha demostrat la seva capacitat per obtenir imatges d'alta resolució topogràfica de mostres bacterianes tant en condicions seques com sota líquid, amb la possibilitat de visualitzar processo vius, com ara l'extrusió de virus [13] o la germinació de les espores bacterianes, entre altres coses [14]. Propietats físiques obtingudes simultàniament a la imatge topogràfica inclouen característiques mecàniques (pressió de turgència, elasticitat, forces d'adhesió) [15], els atributs químics (composició química, el reconeixement d'antígens, hidrofobicitat) [16], les respostes funcionals (efectes *in situ* d'antibiòtics,

modificacions en el medi de cultiu, efecte de la radiació de microones) [17–19], o qualitats elèctriques (càrrega superficial, de valor dielèctric) [20,21].

Aquesta vasta funcionalitat del AFM per caracteritzar cèl·lules bacterianes obre grans possibilitats per a ser utilitzat al camp de la microbiologia; possibilitats que no es poden contemplar amb les eines de microbiologia tradicional. D'aquí en endavant, el AFM pot ajudar a entendre més profundament i resoldre problemes oberts en microbiologia. En particular, pot contribuir a una millor comprensió de les propietats de les cèl·lules bacterianes, una de les formes vives més destacades.

Una característica destacada que presenten algunes espècies bacterianes és la capacitat de produir espores per suportar condicions extremes. En particular, les endòspores han atret l'atenció dels investigadors, ja que és una forma inactiva de la cèl·lula bacteriana que ha evolucionat per suportar condicions ambientals adverses, sent posteriorment capaç de germinar i tornar de nou al seu estat natural quan es compleixen les condicions adequades. Al sector de la medicina i la indústria alimentària això és de gran preocupació, ja que les tècniques d'esterilització quotidianes (alta temperatura, radiació UV, desinfectants comuns o processos de dessecació [22]) no es poden utilitzar a causa de la capacitat de les espores a romandre latents en condicions extremes.

Aquestes característiques extraordinàries per sobreviure a condicions extremes, que no s'ha observat fins a tal punt en altres organismes, s'ha atribuït principalment a com l'endòspora pot controlar el seu contingut d'aigua. Una distribució heterogènia del contingut d'aigua juga un paper clau en la resistència bacteriana [23]. La capacitat del nucli intern de l'endòspora de romandre sec (i per tant menys mòbil) és important per a la seva resistència, ja que el nucli conté les molècules crucials per a la germinació. La eficiència més gran d'inactivació d'un tractament humit comparat a un tractament sec mostra l'efecte que les propietats d'hidratació tenen sobre la resistència de les endòspores [24].

Tot i l'abundant bibliografia existent sobre les propietats d'hidratació de les endòspores bacterianes [25], les capacitats individuals d'hidratació de les endòspores encara presenten algunes preguntes obertes. Com les endòspores seques i latents responen a diferents condicions d'humitat ambiental, com d'higroscòpiques són comparades a les cèl·lules bacterianes vegetatives, i sobretot, quina és la distribució de la hidratació durant la hidratació són algunes de les preguntes que a escala de cèl·lula individual segueixen sense estar clar.

L'objectiu d'aquesta tesi és l'estudi de les propietats d'hidratació de les mostres bacterianes individuals, posant un interès especial en la seva realització en endòspores latents i fent especial èmfasi per cobrir tota la gamma de condicions ambientals. Per realitzar-ho, es van fer mesures des de condicions seques fins a condicions líquides, passant per diferents condicions d'humitat relativa. Per aconseguir aquests resultats, s'ha fet ús del microscopi de forces electrostàtiques (EFM), una adaptació del AFM on el grup de recerca té una experiència considerable. L'ús d'aquesta tècnica pot detectar canvis en les propietats dielèctriques de mostres bacterianes, canvis atribuïts a la presència o absència del contingut d'aigua a causa de la hidratació [21]. Per aconseguir aquest objectiu, diversos reptes de diferents dificultats s'han abordat i resolt.

Embarcant amb un coneixement bàsic del AFM, m'he centrat en el seu ús per realitzar imatges de mostres bacterianes. Amb la dificultat especial de fer imatges de cèl·lules bacterianes vives en condicions natives, em vaig concentrar en la immobilització de mostres bacterianes i l'ús de tècniques d'obtenció d'imatge complexes i avançades. Aquesta implementació s'ha utilitzat per poder observar la divisió bacteriana usant el mètode d'adhesió menys agressiu. La gran alçada de les endòspores i les cèl·lules bacterianes limita l'ús de la metodologia convencional basada en el EFM utilitzada pel grup de recerca. Es va implementar una nova metodologia, amb la seva respectiva comprensió i l'adaptació del AFM per realitzar aquestes mesures.

He dedicat una considerable quantitat d'energia en l'adquisició d'imatges elèctriques d'endòspores individuals en diferents graus d'humitat relativa. Els canvis abruptes en l'alçada de les espores, i la presència d'humitat en combinació amb fer imatges elèctriques, causen l'obtenció dels citats resultats una tasca àrdua. Per arrodonir la feina, les darreres mesures es varen realitzar sota condicions líquides, on la inestabilitat de fer mesures van intensificar la complexitat de l'obtenció de resultats.

La dificultat per observar les cèl·lules bacterianes en les seves condicions de vida natives (en condicions líquides i amb una feble adherència al substrat) sempre ha estat un tema important. Es va abordar la qüestió fent servir substrats plans recoberts de gelatina biocompatible per unir dèbilment les cèl·lules bacterianes, i l'ús del mode d'imatge dynamic jumping mode que causa una dràstica reducció en les forces de cisallament provocades a la mostra comparat als mètodes d'imatge de AFM convencional. Aquesta metodologia ens va

permetre observar la divisió cel·lular bacteriana *in situ* amb una resolució nanomètrica i per bacteris individuals.

La limitació en l'ús del EFM a alçada constant a causa de la gran morfologia no plana de les mostres bacterianes, ens va fer servir el lift mode. La problemàtica d'aquest mètode d'imatge en EFM és la contribució topogràfica, que emmascara la contribució intrínseca de la mostra en estudi. Un anàlisi quantitatiu del lift mode EFM va permetre una caracterització dielèctrica a la nanoescala, revelant una major capacitat d'obtenir les propietats dielèctriques de la zona de la mostra en estudi. L'ús de mostres de calibratge inorgànics i de cèl·lules bacterianes individuals va revelar la necessitat del mètode proposat per a l'anàlisi quantitatiu de les propietats dielèctriques d'aquestes mostres altament no planes, revelant homogeneïtat elèctrica d'aquestes mostres.

La detecció de grànuls d'or enterrats sota una matriu de SiO_2 va revelar les capacitats del EFM com una eina per a la caracterització subsuperficial. La capacitat de detectar una separació de 200nm entre dos grànuls d'or de 200nm a una gran distancia entre la sonda i els grànuls, va mostrar la capacitat del EFM per detectar possibles heterogeneïtats subsuperficial. La semblança entre el gruix de la matriu del SiO_2 amb els de les mostres bacterianes en aquest estudi ens va revelar el potencial del EFM per detectar la distribució d'aigua dins de la cèl·lula de les mostres bacterianes en estudi en aquest treball de tesi.

Continuant amb les capacitats del microscopi de forces electrostàtiques, la capacitat d'obtenir imatges elèctriques en condicions líquides de mostres de gran alçada demostra que la localització del senyal elèctric no es perd a grans distàncies del substrat. El baix contrast exhibit per la gelatina en condicions líquides indica la poca possibilitat que la gelatina emmascari el contrast elèctric d'una mostra dipositada a la part superior de la gelatina. Aquests resultats són d'especial interès per les mesures elèctriques sota líquid de mostres bacterianes vives.

La caracterització elèctrica de les cèl·lules bacterianes vegetatives i les endòspores sota un rang d'humitat relatiu ens va permetre estudiar la diferència en higroscopicitat entre les dues mostres. A baixa humitat relativa, 40%, les endòspores bacterianes no s'hidraten gaire en comparació amb les cèl·lules vegetatives. A alta humitat relativa, 80%, les cèl·lules vegetatives bacterianes s'hidraten dràsticament en comparació amb les endòspores bacterianes. En l'últim

cas, s'ha demostrat que les capes externes donen lloc a la major part de la humitat absorbida, deixant el nucli en nivells baixos d'hidratació. En el cas de les cèl·lules vegetatives, la paret cel·lular no és capaç d'acomodar els alts nivells d'humitat, forçant la hidratació de la regió citoplasmàtica. Aquesta discrepància en el comportament d'hidratació sembla clau per a la persistència de la regió del nucli com la regió més seca de les endòspores bacterianes en condicions atmosfèriques. Això podria ser una de les bases de les grans propietats de resposta d'aigua de les endòspores bacterianes per estendre la seva latència.

Finalment, les mesures elèctriques realitzades en condicions líquides compleixen les mesures elèctriques per caracteritzar les propietats d'hidratació de les mostres bacterianes. L'absència elèctrica observada en les cèl·lules bacterianes vives mostra els alts nivells d'hidratació de l'organisme en condicions natives. En contraposició, la seva homologa rehidratada i les endòspores bacterianes presenten contrast elèctric, mostrant una diferència en el patró d'hidratació. Aquesta menor hidratació podria ser atribuïble a la diferència en l'estructura, com és el cas de les endòspores bacterianes que estan constituïdes per capes concèntriques de proteïnes. Aquesta sensibilitat en condicions líquides obre noves possibilitats pel EFM en condicions líquides per a la caracterització subsuperficial de grans organismes biològics, amb especial interès en les propietats d'hidratació.

Tot junt, aquests resultats obtinguts en aquest treball de tesi han demostrat una menor propietat d'hidratació en les endòspores bacterianes en contraposició a la seva cèl·lula vegetativa en totes les condicions ambientals, des de condicions seques fins a líquides.

12 References

[1] Nataro J P, Kaper J B, Robins-Browne R, Prado V, Vial P and Levine M 1987 Patterns of adherence of diarrheagenic Escherichia coli to HEp-2 cells. *Pediatr. Infect. Dis. J.* **6** 829–831

[2] Marquis R E and Carstensen E L 1973 Electric conductivity and internal osmolality of intact bacterial cells. *J. Bacteriol.* **113** 1198–206

[3] Nealson K H, Platt T and Hastings J W 1970 Cellular control of the synthesis and activity of the bacterial luminescent system. *J. Bacteriol.* **104** 313–22

[4] Blakemore R 1975 Magnetotactic bacteria. *Science* **190** 377–9

[5] Guégan C, Garderes J, Le Pennec G, Gaillard F, Fay F, Linossier I, Herry J-M, Fontaine M-N B and Réhel K V 2014 Alteration of bacterial adhesion induced by the substrate stiffness. *Colloids Surf. B. Biointerfaces* **114** 193–200

[6] Wiencek K M, Klapes N A and Foegeding P M 1990 Hydrophobicity of Bacillus and Clostridium spores. *Appl. Environ. Microbiol.* **56** 2600–5

[7] Waldham D G and Halvorson H O 1954 Studies on the relationship between equilibrium vapor pressure and moisture content of bacterial endospores. *Appl. Microbiol.* **2** 333–8

[8] Brehm-Stecher B F and Johnson E A 2004 Single-Cell Microbiology: Tools, Technologies, and Applications *Microbiol. Mol. Biol. Rev.* **68** 538–59

[9] Maddock J R, Alley M R and Shapiro L 1993 Polarized cells, polar actions. *J. Bacteriol.* **175** 7125–9

[10] Dufrêne Y F 2008 Towards nanomicrobiology using atomic force microscopy *Nat. Rev. Microbiol.* **6** 674–80

[11] Ghosal S, Leighton T J, Wheeler K E, Hutcheon I D and Weber P K 2010 Spatially resolved characterization of water and ion incorporation in Bacillus spores *Appl. Environ. Microbiol.* **76** 3275–82

[12] Schmid G, Zeitvogel F, Hao L, Ingino P, Floetenmeyer M, Stierhof Y-D, Schroeppel B, Burkhardt C J, Kappler A and Obst M 2014 3-D analysis of bacterial cell-(iron)mineral aggregates formed during Fe(II) oxidation

by the nitrate-reducing Acidovorax sp . strain BoFeN1 using complementary microscopy tomography approaches *Geobiology* **12** 340–61

[13] Alsteens D, Trabelsi H, Soumillion P and Dufrêne Y F 2013 Multiparametric atomic force microscopy imaging of single bacteriophages extruding from living bacteria *Nat. Commun.* **4** 2926

[14] Plomp M, Leighton T J, Wheeler K E, Hill H D and Malkin A J 2007 In vitro high-resolution structural dynamics of single germinating bacterial spores. *Proc. Natl. Acad. Sci. U. S. A.* **104** 9644–9

[15] Webb H K, Truong V K, Hasan J, Crawford R J and Ivanova E P 2011 Physico-mechanical characterisation of cells using atomic force microscopy - Current research and methodologies. *J. Microbiol. Methods* **86** 131–9

[16] Dague E, Alsteens D, Latgé J-P, Verbelen C, Raze D, Baulard A R and Dufrêne Y F 2007 Chemical force microscopy of single live cells. *Nano Lett.* **7** 3026–30

[17] Wang C, Ehrhardt C J and Yadavalli V K 2016 Nanoscale imaging and hydrophobicity mapping of the antimicrobial effect of copper on bacterial surfaces *Micron* **88** 16–23

[18] OBST M and DITTRICH M 2005 Living under an atomic force microscope. An optimized approach for in vivo investigations on surface alterations towards biomineral nucleation on cyanobacterial cells *Geobiology* **3** 179–93

[19] Shamis Y, Taube A, Mitik-Dineva N, Croft R, Crawford R J and Ivanova E P 2011 Specific Electromagnetic Effects of Microwave Radiation on Escherichia coli *Appl. Environ. Microbiol.* **77** 3017–23

[20] Marlière C and Dhahri S 2015 An in vivo study of electrical charge distribution on the bacterial cell wall by atomic force microscopy in vibrating force mode *Nanoscale* **7** 8843–57

[21] Esteban-Ferrer D, Edwards M A, Fumagalli L, Juárez A and Gomila G 2014 Electric Polarization Properties of Single Bacteria Measured with Electrostatic Force Microscopy *ACS Nano* **8** 9843–9

[22] Setlow P 2006 Spores of Bacillus subtilis: their resistance to and killing by radiation, heat and chemicals. *J. Appl. Microbiol.* **101** 514–25

[23] Cowan A E, Koppel D E, Setlow B and Setlow P 2003 A soluble protein

is immobile in dormant spores of Bacillus subtilis but is mobile in germinated spores: implications for spore dormancy. *Proc. Natl. Acad. Sci. U. S. A.* **100** 4209–14

[24] FOX K and EDER B D 1969 Comparison of Survivor Curves of Bacillus subtilis Spores Subjected to Wet and Dry Heat *J. Food Sci.* **34** 518–21

[25] Abel-Santos E 2012 *Bacterial spores : current research and applications* (Norfolk UK: Caister Academic Press)

[26] Silhavy T J, Kahne D and Walker S 2010 The Bacterial Cell Envelope *Cold Spring Harb. Perspect. Biol.* **2** a000414

[27] Sheikh J, Hicks S, Dall'Agnol M, Phillips A D and Nataro J P 2008 Roles for Fis and YafK in biofilm formation by enteroaggregative Escherichia coli *Mol. Microbiol.* **41** 983–97

[28] Booth S C, Workentine M L, Wen J, Shaykhutdinov R, Vogel H J, Ceri H, Turner R J and Weljie A M 2011 Differences in Metabolism between the Biofilm and Planktonic Response to Metal Stress *J. Proteome Res.* **10** 3190–9

[29] Angert E R 2005 Alternatives to binary fission in bacteria *Nat. Rev. Microbiol.* **3** 214–24

[30] Furuya E Y and Lowy F D 2006 Antimicrobial-resistant bacteria in the community setting *Nat. Rev. Microbiol.* **4** 36–45

[31] Okhuysen P C and DuPont H L 2010 Enteroaggregative *Escherichia coli* (EAEC): A Cause of Acute and Persistent Diarrhea of Worldwide Importance *J. Infect. Dis.* **202** 503–5

[32] Rogers T E, Ataide S F, Dare K, Katz A, Seveau S, Roy H and Ibba M 2012 A pseudo-tRNA modulates antibiotic resistance in Bacillus cereus *PLoS One* **7**

[33] Wang C, Stanciu C, Ehrhardt C J and Yadavalli V K 2015 Morphological and mechanical imaging of Bacillus cereus spore formation at the nanoscale. *J. Microsc.* **0** 1–10

[34] Nicholson W L, Munakata N, Horneck G, Melosh H J and Setlow P 2000 Resistance of Bacillus endospores to extreme terrestrial and extraterrestrial environments *Microbiol. Mol. Biol. Rev.* **64** 548–72

[35] Plomp M, Leighton T J, Wheeler K E and Malkin A J 2005 The high-resolution architecture and structural dynamics of Bacillus spores.

Biophys. J. **88** 603–8

[36] Errington J 2003 Regulation of endospore formation in Bacillus subtilis *Nat. Rev. Microbiol.* **1** 117–26

[37] Mah J-H, Kang D-H and Tang J 2008 Morphological study of heat-sensitive and heat-resistant spores of Clostridium sporogenes, using transmission electron microscopy. *J. Food Prot.* **71** 953–8

[38] Binnig G, Quate C F and Gerber C 1986 Atomic Force Microscope *Phys. Rev. Lett.* **56** 930–3

[39] Müller D J and Dufrêne Y F 2008 Atomic force microscopy as a multifunctional molecular toolbox in nanobiotechnology *Nat. Nanotechnol.* **3** 261–9

[40] Dorobantu L S, Goss G G and Burrell R E 2012 Atomic force microscopy: A nanoscopic view of microbial cell surfaces *Micron* **43** 1312–22

[41] Gould S A C 1990 From atoms to integrated circuit chips, blood cells, and bacteria with the atomic force microscope *J. Vac. Sci. Technol. A Vacuum, Surfaces, Film.* **8** 369

[42] Chen P, Xu L, Liu J, Hol F J H, Keymer J E, Taddei F, Han D and Lindner A B 2014 Nanoscale Probing the Kinetics of Oriented Bacterial Cell Growth Using Atomic Force Microscopy *Small* 1–8

[43] Louise Meyer R, Zhou X, Tang L, Arpanaei A, Kingshott P and Besenbacher F 2010 Immobilisation of living bacteria for AFM imaging under physiological conditions *Ultramicroscopy* **110** 1349–57

[44] Gramse G, Kasper M, Fumagalli L, Gomila G, Hinterdorfer P and Kienberger F 2014 Calibrated complex impedance and permittivity measurements with scanning microwave microscopy. *Nanotechnology* **25** 145703

[45] Biagi M C, Fabregas R, Gramse G, Van Der Hofstadt M, Juárez A, Kienberger F, Fumagalli L and Gomila G 2016 Nanoscale Electric Permittivity of Single Bacterial Cells at Gigahertz Frequencies by Scanning Microwave Microscopy *ACS Nano* **10** 280–288

[46] Fumagalli L, Gramse G, Esteban-Ferrer D, Edwards M a. and Gomila G 2010 Quantifying the dielectric constant of thick insulators using electrostatic force microscopy *Appl. Phys. Lett.* **96** 183107

[47] Hudlet S, Saint Jean M, Guthmann C and Berger J 1998 Evaluation of the capacitive force between an atomic force microscopy tip and a metallic surface *Eur. Phys. J. B* **2** 5–10

[48] Gomila G, Gramse G and Fumagalli L 2014 Finite-size effects and analytical modeling of electrostatic force microscopy applied to dielectric films *Nanotechnology* **25** 255702

[49] Fumagalli L, Esteban-Ferrer D, Cuervo A, Carrascosa J L and Gomila G 2012 Label-free identification of single dielectric nanoparticles and viruses with ultraweak polarization forces *Nat Mater* **11** 808–16

[50] García R and Pérez R 2002 Dynamic atomic force microscopy methods *Surf. Sci. Rep.* **47** 197–301

[51] Lee Y, Ding Z and Bard A J 2002 Combined Scanning Electrochemical/Optical Microscopy with Shear Force and Current Feedback *Anal. Chem.* **74** 3634–43

[52] Macpherson J V and Unwin P R 2000 Combined Scanning Electrochemical−Atomic Force Microscopy *Anal. Chem.* **72** 276–85

[53] Umeda K I, Kobayashi K, Oyabu N, Hirata Y, Matsushige K and Yamada H 2014 Practical aspects of Kelvin-probe force microscopy at solid/liquid interfaces in various liquid media *J. Appl. Phys.* **116**

[54] Johnson A S, Nehl C L, Mason M G and Hafner J H 2003 Fluid Electric Force Microscopy for Charge Density Mapping in Biological Systems Fluid Electric Force Microscopy for Charge Density Mapping in Biological Systems 10007–10

[55] Marlière C and Dhahri S 2015 An in vivo study of electrical charge distribution on the bacterial cell wall by atomic force microscopy in vibrating force mode *Nanoscale*

[56] Sotres J and Baró a. M 2008 DNA molecules resolved by electrical double layer force spectroscopy imaging *Appl. Phys. Lett.* **93** 103903

[57] Raiteri R, Preuss M, Grattarola M and Butt H-J 1998 Preliminary results on the electrostatic double-layer force between two surfaces with high surface potentials *Colloids Surfaces A Physicochem. Eng. Asp.* **136** 191–7

[58] Hirata Y, Mizutani F and Yokoyama H 1999 In situ observation of electrode surfaces using scanning Maxwell- stress microscopy under water *Surf. Interface Anal.* **27** 317–23

[59] Raiteri R and Butt H J 1995 Measuring electrochemically induced surface stress with an atomic force microscope *J. Phys. Chem.* **99** 15728–32

[60] Umeda K I, Oyabu N, Kobayashi K, Hirata Y, Matsushige K and Yamada H 2010 High-resolution frequency-modulation atomic force microscopy in liquids using electrostatic excitation method *Appl. Phys. Express* **3** 11–4

[61] Umeda K I, Kobayashi K, Oyabu N, Hirata Y, Matsushige K and Yamada H 2013 Analysis of capacitive force acting on a cantilever tip at solid/liquid interfaces *J. Appl. Phys.* **113**

[62] Gramse G, Edwards M a, Fumagalli L and Gomila G 2013 Theory of amplitude modulated electrostatic force microscopy for dielectric measurements in liquids at MHz frequencies. *Nanotechnology* **24** 415709

[63] Gramse G, Edwards M a., Fumagalli L and Gomila G 2012 Dynamic electrostatic force microscopy in liquid media *Appl. Phys. Lett.* **101** 213108

[64] Gramse G, Dols-Perez A, Edwards M A, Fumagalli L and Gomila G 2013 Nanoscale Measurement of the Dielectric Constant of Supported Lipid Bilayers in Aqueous Solutions with Electrostatic Force Microscopy *Biophys. J.* **104** 1257–62

[65] Dufrêne Y F and Garcia-Parajo M F 2012 Recent progress in cell surface nanoscopy: light and force in the near-field *Nano Today* **7** 390–403

[66] Alsteens D, Dupres V, Andre G and Dufrêne Y F 2011 Frontiers in microbial nanoscopy. *Nanomedicine (Lond).* **6** 395–403

[67] Dufrêne Y F 2004 Using nanotechniques to explore microbial surfaces *Nat. Rev. Microbiol.* **2** 451–60

[68] Yamashita H, Taoka A, Uchihashi T, Asano T, Ando T and Fukumori Y 2012 Single-molecule imaging on living bacterial cell surface by high-speed AFM. *J. Mol. Biol.* **422** 300–9

[69] Andre G, Kulakauskas S, Chapot-Chartier M-P, Navet B, Deghorain M, Bernard E, Hols P and Dufrêne Y F 2010 Imaging the nanoscale organization of peptidoglycan in living Lactococcus lactis cells *Nat. Commun.* **1** 27

[70] Alsteens D, Dague E, Verbelen C, Andre G, Dupres V and Dufrêne Y F 2009 Nanoscale imaging of microbial pathogens using atomic force

microscopy *Wiley Interdiscip. Rev. Nanomedicine Nanobiotechnology* **1** 168–80

[71] Longo G, Rio L M, Trampuz A, Dietler G, Bizzini A and Kasas S 2013 Antibiotic-induced modifications of the stiffness of bacterial membranes *J. Microbiol. Methods* **93** 80–4

[72] Fantner G E, Barbero R J, Gray D S and Belcher A M 2010 Kinetics of antimicrobial peptide activity measured on individual bacterial cells using high-speed atomic force microscopy *Nat. Nanotechnol.* **5** 280–5

[73] Sokolov I Y 1996 In situ high-resolution atomic force microscope imaging of biological surfaces *J. Vac. Sci. Technol. A Vacuum, Surfaces, Film.* **14** 674

[74] Bolshakova A V, Kiselyova O I, Filonov A S, Frolova O Y, Lyubchenko Y L and Yaminsky I V 2001 Comparative studies of bacteria with an atomic force microscopy operating in different modes *Ultramicroscopy* **86** 121–8

[75] Turner R D, Thomson N H, Kirkham J and Devine D 2010 Improvement of the pore trapping method to immobilize vital coccoid bacteria for high-resolution AFM: a study of Staphylococcus aureus. *J. Microsc.* **238** 102–10

[76] Chopinet L, Formosa C, Rols M P, Duval R E and Dague E 2013 Imaging living cells surface and quantifying its properties at high resolution using AFM in QI™ mode *Micron* **48** 26–33

[77] Lonergan N E, Britt L D and Sullivan C J 2014 Immobilizing live Escherichia coli for AFM studies of surface dynamics *Ultramicroscopy* **137** 30–9

[78] Doktycz M J, Sullivan C J, Hoyt P R, Pelletier D A, Wu S and Allison D P 2003 AFM imaging of bacteria in liquid media immobilized on gelatin coated mica surfaces *Ultramicroscopy* **97** 209–16

[79] Shu A-C, Wu C-C, Chen Y-Y, Peng H-L, Chang H-Y and Yew T-R 2008 Evidence of DNA transfer through F-pilus channels during Escherichia coli conjugation *Langmuir* **24** 6796–802

[80] Sullivan C J, Venkataraman S, Retterer S T, Allison D P and Doktycz M J 2007 Comparison of the indentation and elasticity of E. coli and its spheroplasts by AFM *Ultramicroscopy* **107** 934–42

[81] Formosa C, Grare M, Duval R E and Dague E 2012 Nanoscale effects of

antibiotics on P. aeruginosa *Nanomedicine* **8** 12–6

[82] Wu Y and Zhou A 2009 In situ, real-time tracking of cell wall topography and nanomechanics of antimycobacterial drugs treated Mycobacterium JLS using atomic force microscopy *Chem. Commun. (Camb).* 7021–3

[83] Fletcher M 1994 Bacterial biofilms and biofouling *Curr. Opin. Biotechnol.* **5** 302–6

[84] Hall-Stoodley L, Costerton J W and Stoodley P 2004 Bacterial biofilms: from the natural environment to infectious diseases *Nat. Rev. Microbiol.* **2** 95–108

[85] Ortega-Esteban A, Horcas I, Hernando-Pérez M, Ares P, Pérez-Berná A J, San Martín C, Carrascosa J L, de Pablo P J and Gómez-Herrero J 2012 Minimizing tip-sample forces in jumping mode atomic force microscopy in liquid *Ultramicroscopy* **114** 56–61

[86] Pérez-Berná A J, Ortega-Esteban A, Menéndez-Conejero R, Winkler D C, Menéndez M, Steven A C, Flint S J, de Pablo P J and San Martín C 2012 The role of capsid maturation on adenovirus priming for sequential uncoating *J. Biol. Chem.* **287** 31582–95

[87] Ortega-Esteban A, Pérez-Berná A J, Menéndez-Conejero R, Flint S J, San Martín C and de Pablo P J 2013 Monitoring dynamics of human adenovirus disassembly induced by mechanical fatigue. *Sci. Rep.* **3** 1434

[88] Blattner F R 1997 The Complete Genome Sequence of Escherichia coli K-12 *Science (80-.).* **277** 1453–62

[89] Beckmann M a, Venkataraman S, Doktycz M J, Nataro J P, Sullivan C J, Morrell-Falvey J L, Allison D P, M.A. Beckmann M.J. Doktycz, J.P. Nataro, C.J. Sullivan, S V and J.L. Morrell-Falvey D P A 2006 Measuring cell surface elasticity on enteroaggregative Escherichia coli wild type and dispersin mutant by AFM *Ultramicroscopy* **106** 695–702

[90] Oh Y J, Cui Y, Kim H, Li Y, Hinterdorfer P and Park S 2012 Characterization of curli A production on living bacterial surfaces by scanning probe microscopy *Biophys. J.* **103** 1666–71

[91] Otero J, Baños R, González L, Torrents E, Juárez A and Puig-Vidal M 2013 Quartz tuning fork studies on the surface properties of Pseudomonas aeruginosa during early stages of biofilm formation *Colloids Surf. B. Biointerfaces* **102** 117–23

[92] Moreno-Herrero F, de Pablo P ., Álvarez M, Colchero J, Gómez-Herrero

J and Baró A . 2003 Jumping mode scanning force microscopy: a suitable technique for imaging DNA in liquids *Appl. Surf. Sci.* **210** 22–6

[93] Gil A, Colchero J, Gómez-Herrero J and Baró A M 2001 Different stages of water adsorption on Au studied by dynamic SFM and jumping mode *Appl. Phys. A* **72** S137–40

[94] Hernando-Pérez M, Lambert S, Nakatani-Webster E, Catalano C E and de Pablo P J 2014 Cementing proteins provide extra mechanical stabilization to viral cages. *Nat. Commun.* **5** 4520

[95] Horcas I, Fernández R, Gómez-Rodríguez J M, Colchero J, Gómez-Herrero J and Baro a M 2007 WSXM: a software for scanning probe microscopy and a tool for nanotechnology *Rev. Sci. Instrum.* **78** 13705

[96] Müller C and Ziegler C 2013 The scanning force microscope in bacterial cell investigations *Phys. Status Solidi* **210** 846–52

[97] Kubitschek H E 1990 Cell volume increase in Escherichia coli after shifts to richer media. *J. Bacteriol.* **172** 94–101

[98] Matias V R F, Al-Amoudi A, Dubochet J and Beveridge T J 2003 Cryo-Transmission Electron Microscopy of Frozen-Hydrated Sections of Escherichia coli and Pseudomonas aeruginosa *J. Bacteriol.* **185** 6112–8

[99] Guzman H V and Garcia R 2013 Peak forces and lateral resolution in amplitude modulation force microscopy in liquid. *Beilstein J. Nanotechnol.* **4** 852–9

[100] Morin N, Santiago A E, Ernst R K, Guillot S J and Nataro J P 2013 Characterization of the AggR regulon in enteroaggregative Escherichia coli. *Infect. Immun.* **81** 122–32

[101] Reshes G, Vanounou S, Fishov I and Feingold M 2008 Timing the start of division in E. coli: a single-cell study. *Phys. Biol.* **5** 46001

[102] Lee D T, Pelz J P and Bhushan B 2006 Scanning capacitance microscopy for thin film measurements *Nanotechnology* **17** 1484–91

[103] Fumagalli L, Ferrari G, Sampietro M and Gomila G 2007 Dielectric-constant measurement of thin insulating films at low frequency by nanoscale capacitance microscopy *Appl. Phys. Lett.* **91** 243110

[104] Fumagalli L, Ferrari G, Sampietro M and Gomila G 2009 Quantitative nanoscale dielectric microscopy of single-layer supported biomembranes *Nano Lett.* **9** 1604–8

[105] Krayev A V and Talroze R V 2004 Electric force microscopy of dielectric heterogeneous polymer blends *Polymer (Guildf).* **45** 8195–200

[106] Crider P S, Majewski M R, Zhang J, Oukris H and Israeloff N E 2007 Local dielectric spectroscopy of polymer films *Appl. Phys. Lett.* **91** 13102

[107] Lu W, Wang D and Chen L 2007 Near-static dielectric polarization of individual carbon nanotubes. *Nano Lett.* **7** 2729–33

[108] Riedel C, Arinero R, Tordjeman P, Lévêque G, Schwartz G a., Alegria A and Colmenero J 2010 Nanodielectric mapping of a model polystyrene-poly(vinyl acetate) blend by electrostatic force microscopy *Phys. Rev. E* **81** 10801

[109] Kumar B, Bonvallet J C and Crittenden S R 2012 Dielectric constants by multifrequency non-contact atomic force microscopy. *Nanotechnology* **23** 25707

[110] Shao R, Kalinin S V. and Bonnell D A 2003 Local impedance imaging and spectroscopy of polycrystalline ZnO using contact atomic force microscopy *Appl. Phys. Lett.* **82** 1869

[111] Pingree L S C and Hersam M C 2005 Bridge-enhanced nanoscale impedance microscopy *Appl. Phys. Lett.* **87** 233117

[112] Hu J, Xiao X-D and Salmeron M 1995 Scanning polarization force microscopy: A technique for imaging liquids and weakly adsorbed layers *Appl. Phys. Lett.* **67** 476

[113] Hu J, Xiao X D, Ogletree D F and Salmeron M 1995 Imaging the condensation and evaporation of molecularly thin films of water with nanometer resolution. *Science* **268** 267–9

[114] Verdaguer A, Cardellach M and Fraxedas J 2008 Thin water films grown at ambient conditions on BaF(2)(111) studied by scanning polarization force microscopy. *J. Chem. Phys.* **129** 174705

[115] Benitez J J, de la Fuente O R, Díez-Pérez I, Sanz F and Salmeron M 2005 Dielectric properties of self-assembled layers of octadecylamine on mica in dry and humid environments. *J. Chem. Phys.* **123** 104706

[116] Lai K, Ji M B, Leindecker N, Kelly M A and Shen Z X 2007 Atomic-force-microscope-compatible near-field scanning microwave microscope with separated excitation and sensing probes. *Rev. Sci. Instrum.* **78** 63702

[117] Lai K, Kundhikanjana W, Kelly M A and Shen Z-X 2011 Nanoscale

microwave microscopy using shielded cantilever probes *Appl. Nanosci.* **1** 13–8

[118] Cho Y 2011 Scanning nonlinear dielectric microscopy *J. Mater. Res.* **26** 2007–16

[119] Krauss T D and Brus L E 1999 Charge, Polarizability, and Photoionization of Single Semiconductor Nanocrystals *Phys. Rev. Lett.* **83** 4840–3

[120] Cherniavskaya O, Chen L, Weng V, Yuditsky L and Brus L E 2003 Quantitative Noncontact Electrostatic Force Imaging of Nanocrystal Polarizability *J. Phys. Chem. B* **107** 1525–31

[121] Ben-Porat C H, Cherniavskaya O, Brus L, Cho K-S and Murray C B 2004 Electric Fields on Oxidized Silicon Surfaces: Static Polarization of PbSe Nanocrystals † *J. Phys. Chem. A* **108** 7814–9

[122] Bockrath M, Markovic N, Shepard A, Tinkham M, Gurevich L, Kouwenhoven L P, Wu M W and Sohn L L 2002 Scanned Conductance Microscopy of Carbon Nanotubes and λ-DNA *Nano Lett.* **2** 187–90

[123] Lu W, Xiong Y, Hassanien A, Zhao W, Zheng M and Chen L 2009 A Scanning Probe Microscopy Based Assay for Single-Walled Carbon Nanotube Metallicity *Nano Lett.* **9** 1668–72

[124] Yang Y, Guo W, Wang X, Wang Z, Qi J and Zhang Y 2012 Size dependence of dielectric constant in a single pencil-like ZnO nanowire. *Nano Lett.* **12** 1919–22

[125] Cuervo A, Dans P D, Carrascosa J L, Orozco M, Gomila G and Fumagalli L 2014 Direct measurement of the dielectric polarization properties of DNA. *Proc. Natl. Acad. Sci. U. S. A.* **111** E3624-30

[126] Dols-Perez A, Gramse G, Calò A, Gomila G and Fumagalli L 2015 Nanoscale electric polarizability of ultrathin biolayers on insulating substrates by electrostatic force microscopy. *Nanoscale* **7** 18327–36

[127] Barbet S, Popoff M, Diesinger H, Deresmes D, Théron D and Mélin T 2014 Cross-talk artefacts in Kelvin probe force microscopy imaging: A comprehensive study *J. Appl. Phys.* **115** 144313

[128] Oliver R a 2008 Advances in AFM for the electrical characterization of semiconductors *Reports Prog. Phys.* **71** 76501

[129] Tevaarwerk E, Keppel D G, Rugheimer P, Lagally M G and Eriksson M

A 2005 Quantitative analysis of electric force microscopy: The role of sample geometry *Rev. Sci. Instrum.* **76** 53707

[130] Lee M, Lee W and Prinz F B 2006 Geometric artefact suppressed surface potential measurements *Nanotechnology* **17** 3728–33

[131] Gramse G, Gomila G and Fumagalli L 2012 Quantifying the dielectric constant of thick insulators by electrostatic force microscopy: effects of the microscopic parts of the probe. *Nanotechnology* **23** 205703

[132] Pommerville J C 2014 *Fundamentals Of Microbiology* (Jones & Bartlett Learning)

[133] Hornstra L M, de Vries Y P, de Vos W M and Abee T 2006 Influence of sporulation medium composition on transcription of ger operons and the germination response of spores of Bacillus cereus ATCC 14579. *Appl. Environ. Microbiol.* **72** 3746–9

[134] Liu B, Hemayet Uddin M, Wah Ng T, Paterson D L, Velkov T, Li J and Fu J 2014 In situ probing the interior of single bacterial cells at nanometer scale *Nanotechnology* **25** 415101

[135] Shekhawat G S and Dravid V P 2005 Nanoscale imaging of buried structures via scanning near-field ultrasound holography. *Science* **310** 89–92

[136] Tetard L, Passian A, Venmar K T, Lynch R M, Voy B H, Shekhawat G, Dravid V P and Thundat T 2008 Imaging nanoparticles in cells by nanomechanical holography. *Nat. Nanotechnol.* **3** 501–5

[137] Govyadinov A a., Mastel S, Golmar F, Chuvilin A, Carney P S and Hillenbrand R 2014 Recovery of permittivity and depth from near-field data as a step toward infrared nanotomography *ACS Nano* **8** 6911–21

[138] Tselev A, Velmurugan J, Ievlev A V., Kalinin S V. and Kolmakov A 2016 Seeing through Walls at the Nanoscale: Microwave Microscopy of Enclosed Objects and Processes in Liquids *ACS Nano* acsnano.5b07919

[139] Riedel C, Alegría A, Schwartz G a., Arinero R, Colmenero J and Sáenz J J 2011 On the use of electrostatic force microscopy as a quantitative subsurface characterization technique: A numerical study *Appl. Phys. Lett.* **99** 23101

[140] Arinero R, Riedel C and Guasch C 2012 Numerical simulations of electrostatic interactions between an atomic force microscopy tip and a dielectric sample in presence of buried nano-particles *J. Appl. Phys.* **112**

[141] Cadena M J, Sung S H, Boudouris B W, Reifenberger R and Raman A 2016 Nanoscale Mapping of Dielectric Properties of Nanomaterials from Kilohertz to Megahertz Using Ultrasmall Cantilevers *ACS Nano* **10** 4062–71

[142] Zhao M, Gu X, Lowther S E, Park C, Jean Y C and Nguyen T 2010 Subsurface characterization of carbon nanotubes in polymer composites via quantitative electric force microscopy. *Nanotechnology* **21** 225702

[143] Cadena M J, Misiego R, Smith K C, Avila A, Pipes B, Reifenberger R and Raman A 2013 Sub-surface imaging of carbon nanotube-polymer composites using dynamic AFM methods. *Nanotechnology* **24** 135706

[144] Jespersen T S and Nygard J 2007 Mapping of individual carbon nanotubes in polymer/nanotube composites using electrostatic force microscopy *Appl. Phys. Lett.* **90** 8–11

[145] Takano H, Wong S S, Harnisch J A and Porter M D 2000 Mapping the subsurface composition of organic films by electric force microscopy *Langmuir* **16** 5231–3

[146] Rothschild L J and Mancinelli R L 2001 Life in extreme environments *Nature* **409** 1092–101

[147] Beaman T C and Gerhardt P 1986 Heat resistance of bacterial spores correlated with protoplast dehydration, mineralization, and thermal adaptation *Appl. Environ. Microbiol.* **52** 1242–6

[148] Setlow P 1994 Mechanisms which contribute to the long-term survival of spores of Bacillus species *J. Appl. Bacteriol.* **76**49S–60S

[149] Driks A, Setlow P and Setlow P 2000 Morphogenesis and Properties of the Bacterial Spore *Prokaryotic Development* ed Y V. Brun and L J Shimkets (American Society of Microbiology) pp 191–218

[150] Sunde E P, Setlow P, Hederstedt L and Halle B 2009 The physical state of water in bacterial spores. *Proc. Natl. Acad. Sci. U. S. A.* **106** 19334–9

[151] Rupley J A and Careri G 1991 Protein hydration and function. *Adv. Protein Chem.* **41** 37–172

[152] Hughes T, Strongin B, Gao F P, Vijayvergiya V, Busath D D and Davis R C 2004 AFM visualization of mobile influenza A M2 molecules in planar bilayers. *Biophys. J.* **87** 311–22

[153] Kaieda S, Setlow B, Setlow P and Halle B 2013 Mobility of core water

in Bacillus subtilis spores by 2H NMR. *Biophys. J.* **105** 2016–23

[154] Ablett S, Darke A H, Lillford P J and Martin D R 1999 Glass formation and dormancy in bacterial spores *Int. J. Food Sci. Technol.* **34** 59–69

[155] Westphal A J, Price P B, Leighton T J and Wheeler K E 2003 Kinetics of size changes of individual Bacillus thuringiensis spores in response to changes in relative humidity. *Proc. Natl. Acad. Sci. U. S. A.* **100** 3461–6

[156] Driks A 2003 The dynamic spore. *Proc. Natl. Acad. Sci. U. S. A.* **100** 3007–9

[157] Chen X, Mahadevan L, Driks A and Sahin O 2014 Bacillus spores as building blocks for stimuli-responsive materials and nanogenerators *Nat. Nanotechnol.* **9** 137–41

[158] Chen X, Goodnight D, Gao Z, Cavusoglu A H, Sabharwal N, DeLay M, Driks A and Sahin O 2015 Scaling up nanoscale water-driven energy conversion into evaporation-driven engines and generators *Nat. Commun.* **6** 7346

[159] Sreeprasad T S, Nguyen P, Alshogeathri A, Hibbeler L, Martinez F, McNeil N and Berry V 2015 Graphene quantum dots interfaced with single bacterial spore for bio-electromechanical devices: a graphene cytobot. *Sci. Rep.* **5** 9138

[160] Leuschner R G K and Lillford P J 2000 Effects of hydration on molecular mobility in phase-bright Bacillus subtilis spores *Microbiology* **146** 49–55

[161] Carstensen E L, Marquis R E and Gerhardt P 1971 Dielectric Study of the Physical State of Electrolytes and Water Within Bacillus cereus *J. Bacteriol.* **107** 106

[162] Henry B S and Friedman C A 1937 The water content of bacterial spores *J. Bacteriol.* **33** 323–9

[163] Algie J E and Watt I C 1984 Calculation of mass and water content between the core, cortex, and coat of Bacillus stearothermophilus spores *Curr. Microbiol.* **10** 249–53

[164] Kong L, Setlow P and Li Y 2013 Direct analysis of water content and movement in single dormant bacterial spores using confocal Raman microspectroscopy and Raman imaging. *Anal. Chem.* **85** 7094–101

[165] Cowan A E, Olivastro E M, Koppel D E, Loshon C a, Setlow B and Setlow P 2004 Lipids in the inner membrane of dormant spores of

Bacillus species are largely immobile *Proc. Natl. Acad. Sci.* **101** 7733–8

[166] Rubel G O 1997 A non-intrusive method for the measurement of water vapour sorption by bacterial spores *J. Appl. Microbiol.* **83** 243–7

[167] Knudsen S M, Cermak N, Feijó Delgado F, Setlow B, Setlow P and Manalis S R 2016 Water and Small-Molecule Permeation of Dormant Bacillus subtilis Spores ed P de Boer *J. Bacteriol.* **198** 168–77

[168] Rusciano G, Zito G, Isticato R, Sirec T, Ricca E, Bailo E and Sasso A 2014 Nanoscale Chemical Imaging of Bacillus subtilis Spores by Combining Tip-Enhanced Raman Scattering and Advanced Statistical Tools *ACS Nano* **8** 12300–9

[169] Van Der Hofstadt M, Fabregas R, Biagi M C, Fumagalli L and Gomila G 2016 Nanoscale dielectric microscopy of non-planar samples by lift-mode electrostatic force microscopy *Nanotechnology* **27** 405706

[170] Gould G W and Dring G J 1975 Heat resistance of bacterial endospores and concept of an expanded osmoregulatory cortex *Nature* **258** 402–5

[171] Peraica M, Radić B, Lucić A and Pavlović M 1999 Toxic effects of mycotoxins in humans. *Bull. World Health Organ.* **77** 754–66

[172] Ma M, Guo L, Anderson D G and Langer R 2013 Bio-inspired polymer composite actuator and generator driven by water gradients. *Science* **339** 186–9

[173] Kim H and Kwon S 2013 Water-Responsive Polymer Composites on the Move *Science (80-.).* **339** 150–1

[174] Cheng Y, Su H, Koop T, Mikhailov E and Pöschl U 2015 Size dependence of phase transitions in aerosol nanoparticles *Nat. Commun.* **6** 5923

[175] Black S H and Gerhardt P 1962 Permeability of bacterial spores. IV. Water content, uptake, and distribution. *J. Bacteriol.* **83** 960–7

[176] Carrera M, Zandomeni R O, Fitzgibbon J and Sagripanti J-L 2007 Difference between the spore sizes of Bacillus anthracis and other Bacillus species. *J. Appl. Microbiol.* **102** 303–12